UNIVERSIDADE FEDERAL DE SANTA CATARINA
CAMPUS REITOR JOÃO DAVID FERREIRA LIMA
PROGRAMA DE PÓS-GRADUAÇÃO EM ENGENHARIA MECÂNICA

Rodrigo Cerqueira de Campos

Development of a UAV gripping device for fast coupling

Florianópolis
2021

Rodrigo Cerqueira de Campos

Development of a UAV gripping device for fast coupling

Dissertação submetida ao Programa de Pós-Graduação em Engenharia Mecânica da Universidade Federal de Santa Catarina para a obtenção do título de mestre em Engenharia Mecânica.
Orientador: Prof. Henrique Simas, Dr. Eng.
Coorientador: Prof. Estevan Hideki Murai, Dr. Eng.

Florianópolis
2021

Ficha de identificação da obra elaborada pelo autor,
através do Programa de Geração Automática da Biblioteca Universitária da UFSC.

Cerqueira de Campos, Rodrigo
Development of a UAV gripping device for fast coupling / Rodrigo Cerqueira de Campos ; orientador, Henrique Simas, coorientador, Estevan Hideki Murai, 2022.
110 p.

Dissertação (mestrado) - Universidade Federal de Santa Catarina, Centro Tecnológico, Programa de Pós-Graduação em Engenharia Mecânica, Florianópolis, 2022.

Inclui referências.

1. Engenharia Mecânica. 2. Mechanism synthesis. 3. Optimization. 4. Davies method. 5. Self-alignment. I. Simas, Henrique. II. Murai, Estevan Hideki. III. Universidade Federal de Santa Catarina. Programa de Pós Graduação em Engenharia Mecânica. IV. Título.

Rodrigo Cerqueira de Campos

Development of a UAV gripping device for fast coupling

O presente trabalho em nível de mestrado foi avaliado e aprovado por banca examinadora composta pelos seguintes membros:

Prof. Leonardo Mejia Rincon, Dr. Eng.
Universidade Federal de Santa Catarina

Prof. Edson Roberto de Pieri, Dr.
Universidade Federal de Santa Catarina

Certificamos que esta é a **versão original e final** do trabalho de conclusão que foi julgado adequado para obtenção do título de mestre em Engenharia Mecânica.

Documento assinado digitalmente
Paulo de Tarso Rocha de Mendonca
Data: 15/03/2022 14:26:43-0300
CPF: 149.822.691-49
Verifique as assinaturas em https://v.ufsc.br

Prof. Paulo de Tarso Rocha de Mendonça,
Dr. Eng.
Coordenador do Programa

Documento assinado digitalmente
Henrique Simas
Data: 14/03/2022 18:01:03-0300
CPF: 800.194.639-87
Verifique as assinaturas em https://v.ufsc.br

Prof. Henrique Simas, Dr. Eng.
Orientador

Florianópolis, 16 de dezembro de 2021.

AGRADECIMENTOS

À minha esposa, Hellen Campos, pela paciência e companhia nas incontáveis madrugadas de trabalho durante o mestrado, e pelo suporte e cooperação ao longo da minha vida acadêmica.

Aos meus pais, João e Maria, pelo apoio e incentivo, e por compreenderem a minha ausência. Ao meu irmão Rafael Campos, que apesar da distância, sempre me apoiou com ótimas contribuições e orientações.

Ao meu orientador, Henrique Simas, pelos conselhos e por todo o conhecimento compartilhado na minha pós-graduação. Ao meu coorientador, Estevan Hideki Murai, pela paciência e disponibilidade para as longas reuniões de orientação e direcionamento da pesquisa, e pelas contribuições valiosas que possibilitaram esta pesquisa.

À toda equipe do Laboratório de Robótica da Universidade Federal de Santa Catarina, em especial ao Gustavo Queiroz, à Marina Baldissera e ao Guilherme Bernardi, que sempre me auxiliaram nas mais diversas questões. À minha amiga Taynah Lima, pela amizade e companheirismo ao longo da minha vida acadêmica. Ao meu amigo Paulo Rossi, pelas longas conversas e discussões técnicas, teóricas e filosóficas, tanto presencial quanto à distância, que foram de grande importância para o meu desenvolvimento acadêmico, e pela ótima parceria na elaboração de nossos artigos.

Ao POSMEC pela oportunidade e ao CNPq pelo suporte financeiro.

“Someone’s sitting in the shade today
because someone planted a tree
a long time ago.”
(Warren Buffet)

RESUMO EXPANDIDO

Introdução

Veículos aéreos não tripulados são capazes de se locomover de forma autônoma, através de planos de vôo pré-programados, ou podem ser controlados remotamente por um usuário. Popularmente conhecidos como drones, estes veículos conquistaram sua fama nos últimos anos em uma vasta gama de aplicações, como fotografia, mapeamento de terrenos e inspeção de construções civis. A aplicação de veículos aéreos não-tripulados no transporte de carga é um dos setores com maior potencial de crescimento, por apresentarem diversas vantagens em relação à logística convencional, como menor custo e menor emissão de gases poluentes. Estas vantagens despertaram o interesse em pesquisas relacionadas ao transporte de carga através de drones, como o desenvolvimento de novos métodos de controle, o aperfeiçoamento da eficiência e autonomia de baterias e o desenvolvimento de mecanismos que facilitem a coleta e entrega de pacotes.

Objetivos

O objetivo principal desta dissertação é o desenvolvimento de um mecanismo para o acoplamento rápido de um veículo aéreo não tripulado a um corpo externo. Como forma de garantir que seja atingido o objetivo principal, os seguintes objetivos específicos foram definidos: avaliar o estado da arte de tecnologias utilizadas no transporte de cargas através de drones, e de plataformas de pouso para drones; estabelecer as características desejadas para estas aplicações, bem como as limitações e desvantagens desses sistemas; desenvolver um novo mecanismo capaz de acoplar um drone a um corpo externo de forma autônoma ou remota; realizar a otimização das dimensões da nova topologia com base nas restrições geométricas impostas pelo drone; realizar a análise estática do mecanismo para avaliar o seu comportamento e esforços envolvidos durante o uso.

Metodologia

O desenvolvimento do mecanismo foi dividido em seis etapas. A primeira etapa consiste na revisão bibliográfica de técnicas para realizar o transporte aéreo de carga. Em seguida, é realizado um levantamento do estado da arte de plataformas de pouso para drones, ressaltando as características desejáveis, bem como as limitações e desvantagens de cada sistema. É realizada ainda uma pesquisa de conceitos de funcionamento de grippers utilizados em conjunto aos drones, e mecanismos de trava frequentemente utilizados em robótica.

Através da revisão bibliográfica, é possível prosseguir para a segunda etapa, que consiste na listagem dos requisitos de projeto para o novo mecanismo, bem como as características desejáveis. Estes requisitos são utilizados na terceira etapa, composta pela síntese do número e do tipo, onde são enumerados todas as cadeias cinemáticas que atendem os requisitos estruturais de projeto, e definidos os pares cinemáticos com os quais a nova topologia será construída.

A quarta etapa consiste na otimização dimensional da topologia desenvolvida nas etapas anteriores. Inicialmente, é desenvolvido um modelo matemático que descreve o mecanismo através de coordenadas naturais. Em seguida, este modelo matemático é utilizado para realizar a otimização dimensional da topologia através de um algoritmo genético.
A quinta etapa utiliza os resultados obtidos da otimização da topologia para realizar a análise estática através do método de Davies. Dessa forma, é possível avaliar o comportamento e as forças de reação nos pares cinemáticos durante o uso. Nesta quinta etapa, são realizadas as análises no processo de acoplamento, em que a estática é calculada ao longo de todo o movimento do mecanismo, e durante o transporte aéreo de um corpo externo. Conhecendo as forças de reação nas juntas, é possível calcular os esforços internos de cada elo, e estimar a área da seção interna de cada elo, bem como o peso de cada elemento. Finalmente, as análises estáticas são realizadas novamente, considerando o peso dos componentes para avaliar os efeitos da força gravitacional no comportamento do mecanismo.
A sexta etapa consiste na avaliação de auto-alinhamento do mecanismo. Nesta etapa, as restrições redundantes são identificadas e eliminadas. Em seguida, é feita uma nova análise estática para verificar se há diferenças nas forças de reação dos pares cinemáticos.

Resultados e Discussão

Inicialmente, o mecanismo desenvolvido na terceira etapa foi modelado em um software CAD, e avaliado em relação ao movimento gerado, sendo constatado que a topologia funciona conforme esperado. O processo de otimização foi realizado considerando as restrições geométricas impostas por um drone específico, e resultou em dimensões satisfatórias, considerando que não ocorrem colisões com nenhum elemento do drone durante o processo de acoplamento. A avaliação do efeito gravitacional sobre as forças de reação nos pares cinemáticos foi realizada considerando três materiais diferentes. Foi constatado que mesmo materiais leves influenciam os resultados, e devem ser considerados do dimensionamento da seção transversal dos elos. Finalmente, o processo de auto-alinhamento foi implementado de forma a eliminar as restrições redundantes inicialmente presentes, e a nova análise estática não apresentou diferenças nos resultados em comparação com as análises anteriores.

Considerações finais

Considerando os resultados obtidos ao longo do desenvolvimento deste trabalho, pode-se concluir que o desenvolvimento de um novo mecanismo para acoplamento de um veículo aéreo não tripulado e um corpo externo foi bem sucedido. A metodologia utilizada, apesar da aplicação em um drone específico, é replicável para outros veículos, e o mecanismo em si pode ser adaptado para diferentes requisitos.

Palavras-chave: Método de Davies. Otimização Dimensional. Auto-Alinhamento. Drone. Transporte Aéreo.

ABSTRACT

Unmanned aerial vehicles (UAVs) are increasingly popular among different applications, mainly due to their mechanical simplicity and relatively low cost. The employment of UAVs in logistics and transportation of packages has experienced substantial growth over the last decade and is expected to experience significant growth in the next few years. However, a coupling method between the UAV and the grounded load is still a challenge to overcome. This master thesis aims to develop a passive gripper that allows fast coupling for such applications. The proposed development comprises a state-of-the-art UAV docking system survey to gather desirable features and requirements. A bibliographical review on aerial transport through UAVs is also conducted, along with a review on gripper's and locking mechanisms working principles and classifications. Afterwards, a new gripper topology is developed through number and type syntheses. A dimensional optimization is conducted on the new topology through an evolutionary algorithm, considering the geometrical constraints imposed by a UAV. Once the optimized topology is defined, the Davies method for static analysis is performed to compute the reaction forces acting on the kinematic pairs. Since the forces acting on the links are known, the internal stresses are calculated. An estimate of the cross-section area is defined, along with a mass estimate for a set of selected materials. Furthermore, a new static analysis evaluates the effect of gravitational forces on the mechanism. Finally, a self-alignment analysis is conducted in order to identify and eliminate redundant constraints, and a new static analysis is performed on the final, self-aligned mechanism, which results in reaction forces coherent to the previous studies. This works aims to provide researchers and professionals with a methodology for developing and dimensioning a gripper device for UAV coupling purposes.

Keywords: Davies method. Dimensional optimization. Self-alignment. UAV. Aerial transport.

LIST OF FIGURES

LIST OF TABLES

CONTENTS

1 INTRODUCTION

This chapter introduces the context, objectives, and structure of this master thesis. Section 1.1 introduces the current scenario of applications for Unmanned Aerial Vehicles, including market size and expected growth, as well as the sectors that extensively employ UAVs. Afterwards, Section 1.2 presents the objectives of this research and Section 1.3 describes the procedures to achieve the objectives. Finally, Section 1.4 presents the content of each chapter that composes this master thesis.

1.1 CONTEXTUALIZATION

As the name implies, an unmanned aerial vehicle (UAV) is an aerial vehicle capable of flying autonomously through a computer using pre-programmed flight plans or being controlled remotely by a pilot on the ground. Also known as drones, UAVs became famous over the last few years, starting with photography and recordings of landscapes, and they are already being implemented in a wide range of applications, such as agricultural mapping and surveys, buildings and bridges inspections, powerlines monitoring, parcel delivery, among many others.

In terms of market growth, according to Precedence Research (2021), the UAV market size was valued at USD 14.3 billion in 2020. The Globe Newswire (2021) estimates the global UAV market will reach USD 27.4 billion in 2021 and will reach USD 58.4 billion by 2026.

The UAV market has been categorized in military, commercial, and consumer applications. The military sector adopted UAVs for combat and humanitarian aid and it is currently the biggest UAV market. Nevertheless, the commercial business sector has the fastest growth record, with the infrastructure sector leading the charts (GUPTA et al., 2021). According to the Drone Industry Insights (2021), the Energy sector was the largest industry in the commercial drone market in 2020. Due to UAVs' growth potential and market interest, research on UAV-related applications is also increasing rapidly.

Advances in UAV-related topics has also triggered an increase in applications across various commercial sectors to gather a large amount of real-time information to make strategic decisions. Farmers are employing UAVs for crop data collection to help improve crops. The mining industry uses drones for mapping and surveying construction sites in less time and lower costs than the traditional inspection methods. Law enforcement agencies and rescue personnel have adopted UAVs for surveillance, search and rescue, and public safety (GUPTA et al., 2021).

The increasing number of cars and limited road capacity lead the existing ground transportation infrastructure to more overcrowded levels. Many logistics industries and big retailers started to explore aerial transport of goods through UAVs to avoid the inconveniences of terrestrial transport. The global UAV-assisted logistics market is

increasing rapidly, with around USD 11 billion projected market size until 2026, coming from USD 5.3 billion in 2019 (PR NEWSWIRE, 2021). The rapid growth of UAV usage is observed mainly because of the e-commerce market trying to meet the growing customer expectations of faster delivery. The global health crisis due to Covid-19 has also contributed to the faster growth of the UAV transport market.

UAV delivery is highly promising for the future of logistics. The Drone Industry Insights (2021) stated that even though the Energy sector is currently the most prominent UAV market, the Transportation and Warehousing industry leads the growth rate. UAV delivery has several advantages over conventional delivery methods, such as lower cost, faster delivery, and produces significantly lesser carbon footprints (YOO; YU; JUNG, 2018). In this context, many researchers have been working on efficient UAV transportation strategies in various aspects, such as control methods and techniques, battery efficiency, lightweight materials, and mechanisms for autonomous collecting of packages.

1.2 OBJECTIVES

The main objective of this work is to develop a passive gripping mechanism to be employed with unmanned aerial vehicles capable of attaching the UAV to the payload remotely. The resulting device could be used in the aerial transport of packages or in the terrestrial transport of the UAV itself. The following specific objectives were established to accomplish the main objective:

- To evaluate the current state-of-the-art technologies for remote load transport through UAVs and UAV docking systems, as well as its current drawbacks, limits, and challenges;
- To better understand the remote load grasping problem through the state-of-the-art research;
- To develop a new topology capable of solving the remote load grasping problem based on the last items' research;
- To perform the kinematic synthesis of a novel gripping device topology and optimize the dimensions of the obtained topology considering the geometrical constraints imposed by the intended applications of the device;
- To perform a static analysis of the developed mechanism to evaluate its effectiveness.

1.3 SCOPE OF THIS WORK

To develop the UAV gripping device following the objectives defined for this work, the following procedures were drawn:

- Initially, a bibliographical review is performed to evaluate the existing devices capable of fulfilling the same objective of the mechanism to be developed and other tools and technologies that may contribute to this work, such as docking systems and locking mechanisms.
- Once the state-of-the-art survey is finished, the features and restrictions of the existing devices are evaluated, which may serve as a guide to the synthesis process.
- Finally, the kinematic synthesis is performed considering the project requirements obtained from the bibliographical review and the desired features for the final device. Once the new topology has been defined, a dimensional optimization process is performed considering the geometrical constraints imposed by the UAV. At last, a static analysis is carried out to evaluate the behavior of the final mechanism.

1.4 OVERVIEW OF THIS WORK

This master thesis is composed of seven chapters. Chapter 1 presents the current scenario of UAV applications and growth expectations, which defines this work's motivation. The objectives are drawn, and an overview of steps taken to develop this work is presented.

Chapter 2 presents the bibliographical review that assisted the development. First, the existing techniques for UAV load transportation are exposed, followed by existing UAV docking systems and landing platforms. Since the new device's objective consists of grasping and holding a payload, a survey of grippers used in UAVs and locking mechanisms are also presented.

Chapter 3 brings the methodology used to develop the mechanism, so other researchers can replicate the methodology adopted to create different topologies. The tools used in the kinematic synthesis process are briefly presented.

Chapter 4 presents the development of the gripping device. The structural requirements are drawn considering the features observed in the state-of-the-art survey and intended use. The topology of the mechanism is achieved through the number and type synthesis, and dimensional optimization is performed. Finally, the static analysis is carried out considering the gripping process and aerial transport.

In Chapter 5, an estimate of the links' thickness and weight is carried out through the static analysis results. Next, another static analysis is performed to evaluate the gravitational effect of the members' weight on the mechanism's behavior.

Chapter 6 consists of the self-alignment analysis of the final mechanism.

Finally, Chapter 7 highlights the main conclusions from the development of the device, and some ideas for future work are drawn.

2 BIBLIOGRAPHICAL REVIEW

This chapter aims to present the adopted techniques for load transportation through UAVs and the state-of-the-art technologies that help develop the new mechanism. Section 2.1 presents the explored techniques for load transport and traces some advantages and drawbacks. Section 2.2 presents an overview of the concept of docking systems designed for UAVs, as well as a state-of-the-art survey of these devices. The major features and limitations of the UAV docking designs are highlighted so that this information can be helpful in this work's development. Section 2.3 presents a few concepts on grippers' classification and examples of other works incorporating grippers to UAVs. Section 2.4 presents a brief introduction to locking mechanism's concept and desirable features. Next, a survey of the most used locking mechanisms is presented, with examples of other works that successfully employed them. Finally, section 2.5 concludes the chapter with some final considerations.

2.1 UAV LOAD TRANSPORTATION

UAVs are beneficial in many applications, such as package delivery in urban areas, application of pesticides in agriculture, and providing supplies in conflict zones. However, these applications are still challenging because of their inherent instability and complex dynamics.

Load transportation using UAVs has been accomplished using two major carrying strategies: **cable-suspended load** and **grasped load** (VILLA; BRANDAO; SARCINELLI-FILHO, 2020). Each of these strategies may be implemented using individual or cooperative schemes, i. e. the given task is entirely performed by a single UAV or by a group of UAVs working together.

Figure 1 – Cable-suspended UAV transport.

Source: Cruz and Fierro (2017).

The **cable-suspended** approach comprises connecting the load to the UAV through a cable, as illustrated in Fig. 1, where a solid is taken from the ground through

a cable to the air. Commonly, this leads to the addition of passive degrees of freedom, which generates a swinging motion of the load and affects the UAV's dynamic characteristics. Moreover, the controller system should handle the weight fluctuations that occur when the cable tension changes while landing or taking off and their consequences.

From the mechanical point of view, minor enhancements are possible for the cable-suspended approach. Therefore, most research regarding this kind of system deals with the controlling aspect. Since the UAV's controlling method is not within the scope of this work, it will not be analyzed.

The **grasped** approach consists in attaching the load to the UAV's body through mechanical or electromagnetic grippers, robotic claws, or robotic hands. This option provides more straightforward ways to attach and detach a load, with easier design options to capture and deliver a package. On the other hand, this method reduces rotorcraft agility. Therefore, more thrust is required because of the grasped load, increasing energy consumption, and reducing battery life. Additionally, the center of mass commonly changes, affecting the controlling balance.

2.2 UAV DOCKING SYSTEMS

Despite the growth in the UAV market and the number of research efforts dedicated to UAVs, the short battery life restricts the applications of such devices. Several approaches to improve battery capacity have been proposed but still have significant drawbacks, such as high cost.

Landing platforms for UAVs are among the most promising approaches to extend their operation time. Besides the explored features, like battery charging or swapping, platforms could perform other functions as well, such as picking up cargo. Each of these tasks requires precise positioning and safe locking of the UAV to the platform. The positioning of the UAV at the desired point starts while the vehicle is still in the air when the UAV adjusts its position to land. The deviation between the desired landing position and the achieved position depends on several factors, such as the chosen landing technique, sensors installed in the UAV, the controlling system's performance, and other unpredictable external factors, such as meteorological conditions. A better positioning can be achieved by influencing the landing platform elements, such as geometry. This work does not concern the controlling aspect of landing but focuses on the landing platform elements that provide better accuracy.

The existing landing platforms can be divided into platforms without positioning and with positioning. Platforms with positioning are further divided into active, passive, and combined positioning. In platforms with no positioning, the UAV lands relying only on the accuracy provided by the controlling system. Usually, this type of platform aims to establish an electrical connection through extensive contacts on the platform. There were no examples of manipulation tasks performed using this type of platform found

in the literature. Platforms with active positioning involve mechanisms that move the UAV to the required position. These mechanisms are selected considering the agility requirements of positioning. Platforms with passive positioning achieve the UAV's positioning through the passive interaction of the platform with the UAV elements, which transforms the vertical motion of the landing process into horizontal motion. Passive positioning devices usually use funnels, slopes, inclined edges, among other examples. A platform with combined positioning adopts the benefits of both active and passive methods, capable of achieving better accuracy.

Each type of positioning technique can be further divided into sub-types, presented in Fig. 2. Since the scope of this work is passive mechanisms, each passive positioning platform is analyzed in more detail, except for the closed contours platforms, since all examples found in the literature require a unique design.

Figure 2 – Positioning approaches for UAV landing platforms.

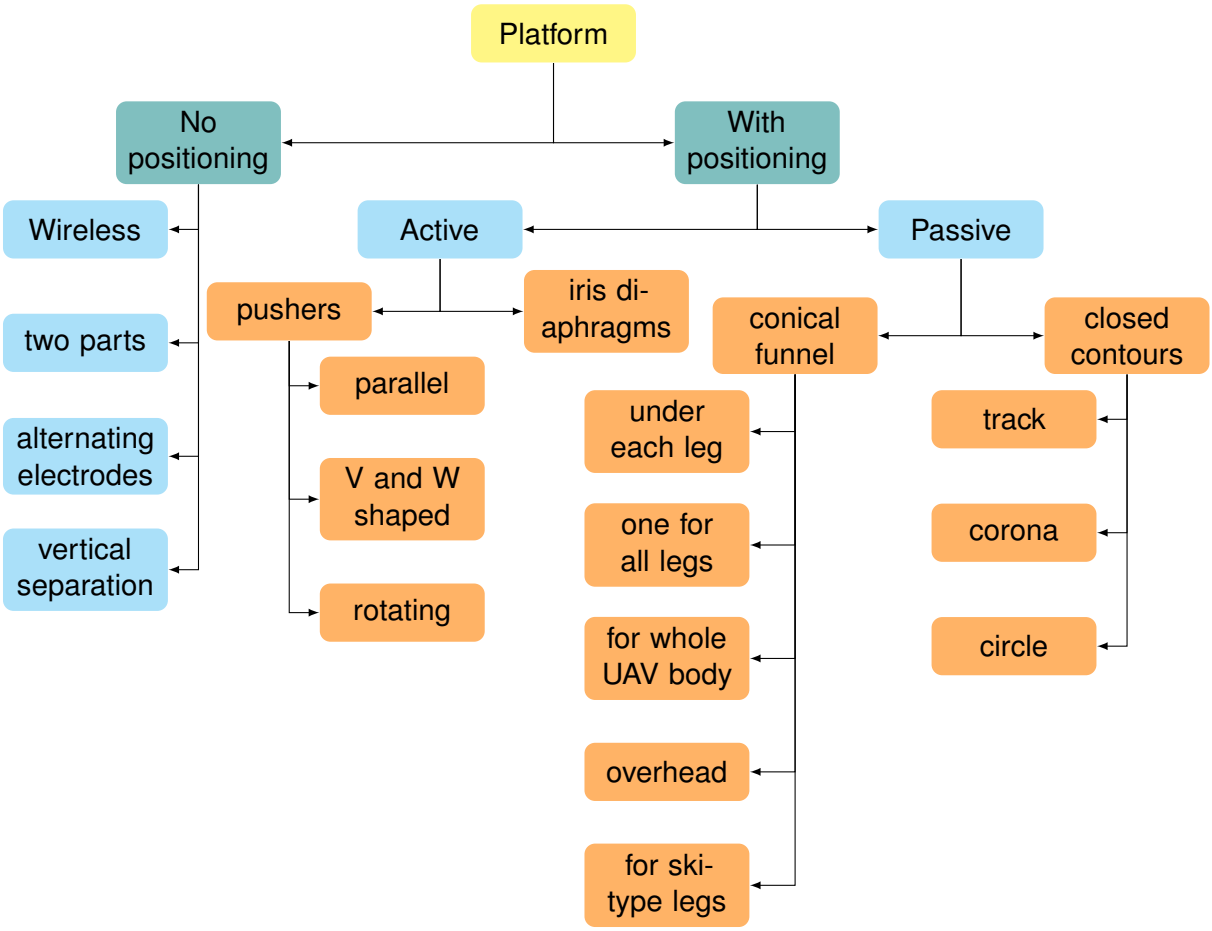

Source: Villa, Brandao, and Sarcinelli-Filho (2020).

Landing platforms with **conical funnels under each leg** are relatively well explored. The funnels may carry out simply the positioning function or contain additional features, such as electrical contacts, inductors, or fixing devices. Figure 3a presents a UAV landing platform developed by Antonini, Fici, and Gaspardone (2019), composed

of a flat surface and four centering funnels. The funnels are coaxial to the UAV legs, which slide to the UAV's desired position, where electrical contacts may be located.

Figure 3b presents a landing system designed for an AC power wirelessly-chargeable device for UAVs, designed by Science and Technology (2016). In this system, the UAV legs end with power receiving units. The landing platform is composed of three funnels to align the UAV and correctly start charging the battery.

Figure 3 – Examples of landing platforms with conical funnels for each leg.

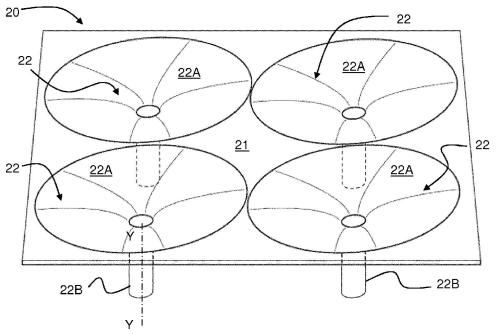

(a) Landing platform developed by Antonini, Fici, and Gaspardone (2019).

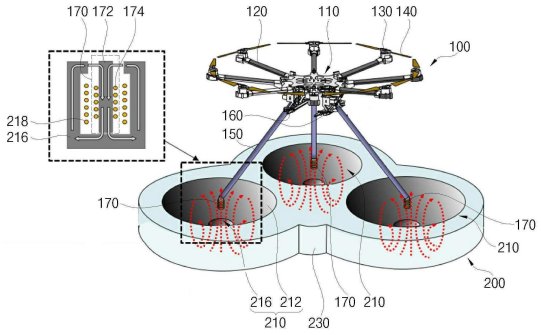

(b) Landing platform developed by Science and Technology (2016).

Landing platforms with a **conical funnel for all legs** simplify the design of the landing platform and are commercially available, such as the Sunflower hive, presented in Fig. 4a. Another example is shown in Fig. 4b, developed by Krauss and Kliner (2020), which is composed of a central funnel formed of trapezoidal segments.

Figure 4 – Examples of landing platforms with conical funnels for all legs.

(a) Sunflower hive developed by Sunflower Labs.

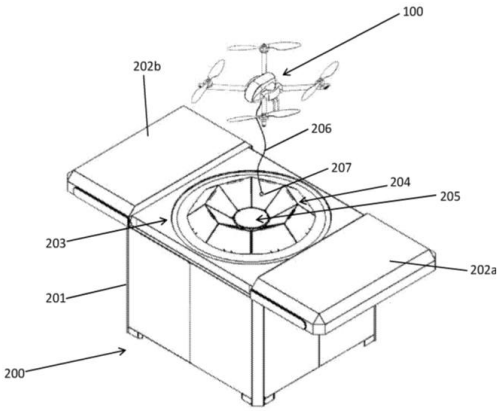

(b) Landing platform developed by Krauss and Kliner (2020).

Stefánsson (2014) developed a few concepts for a UAV docking system that adopts the concept of a single centered funnel. Figure 5 presents one of the concepts. Since all others are minimally changed, focused on details, they will not be presented

here. The project aimed for a fully autonomous pick-up and transport device that could be used for package delivering. The lower platform is fixed to the package, while the upper part, comprised of the mechanism, servo motor and sensors, is mounted to the UAV. When the connection is accomplished, the servo motor rotates the cam to lock the system.

Figure 5 – Stefánsson (2014) UAV docking system concept

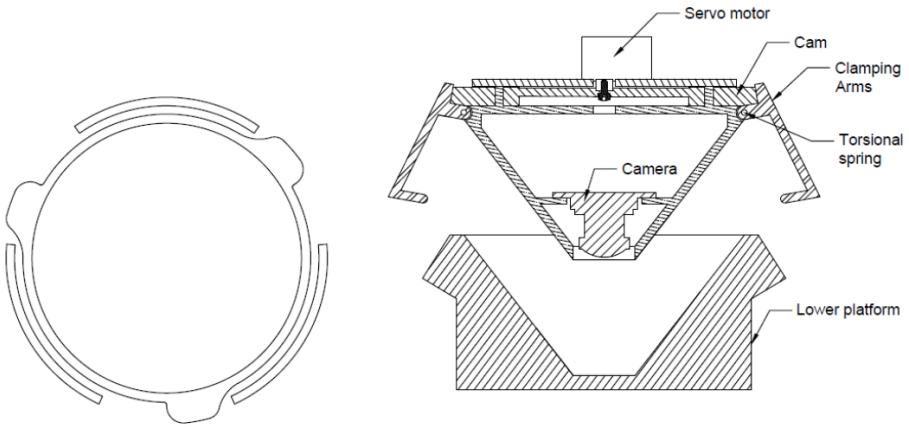

Source: Stefánsson (2014).

A significant disadvantage of this concept is that most components are attached to the drone, increasing the payload and reducing autonomy. In order to keep the device locked in place, the servomotor must be on at all times, which diminishes battery life.

Compagnin et al. (2017) described the Autoport project, developed by the Department of Industrial Engineering of the University of Padua. The project's main goal is to design, build and test a docking station for Mars exploration UAVs. Figure 6 presents each step of the docking process.

The system is composed by a probe, mounted directly on the lower part of the UAV, and a drogue mounted in the docking station. The probe is not equipped with any kind of mechanism, playing a completely passive role. The drogue, on the other hand, is equipped with electric sensors responsible for detecting the probe, and the necessary actuators for a secure fastening.

Landing platforms with a **funnel for the UAV's whole body** is another approach that involves the interaction of the UAV body with the landing platform to achieve the desired position. This is a better approach if the UAV and landing platform are designed together but can be applied in other scenarios. The funnel complements the shape of the UAV body, making a stable fit. Figure 7 presents the concept introduced by Sullivan, Williams, and Prokhorov (2019).

Landing platforms with **overhead cone funnels** are not common. Barbasov K.V.; Barbasov (2017) presented landing platforms in which the UAV is hung, as illustrated in Fig. 8. The conical positioning equipment is oriented upside down and presents a

Figure 6 – Docking steps of the Autoport project.

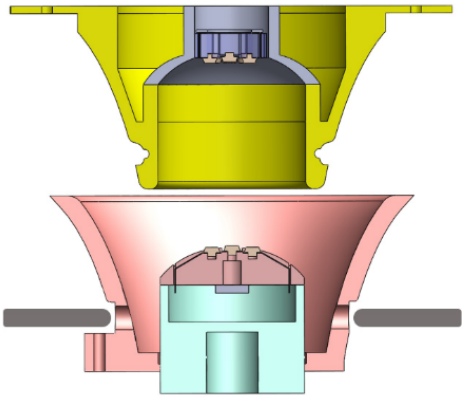

(a) UAV's probe entering the drogue.

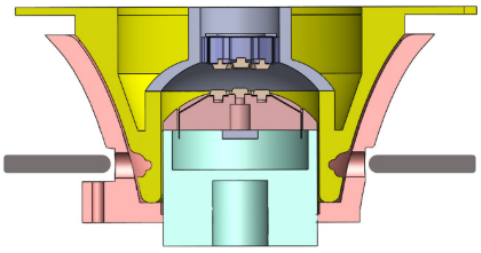

(b) Contact detection by electric sensors.

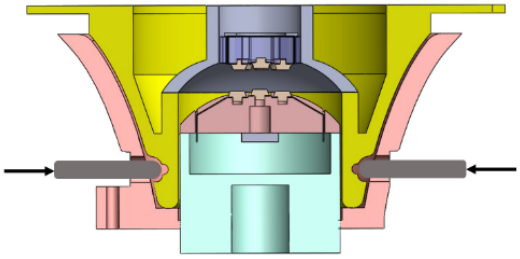

(c) Radial actuators lock the probe.

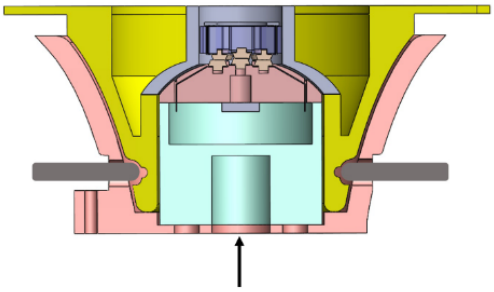

(d) Central pin creates a pre-load. docking is accomplished.

Source: Compagnin et al. (2017).

Figure 7 – Landing platform for the UAVs whole body.

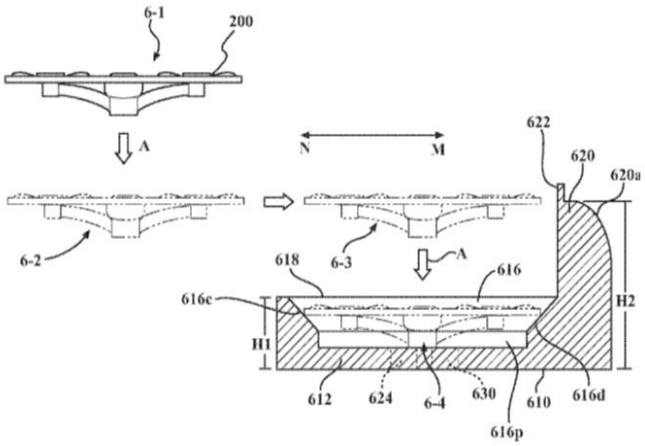

Source: Sullivan, Williams, and Prokhorov (2019)

fast gripping device. In order to land, the UAV has to fly underneath the cone, and a retractable hanger attached to the UAV gets pushed to the center of the funnel.

Landing platforms for **UAVs with ski-type legs** may be considered a way to

Figure 8 – Landing platform with overhead cone funnel.

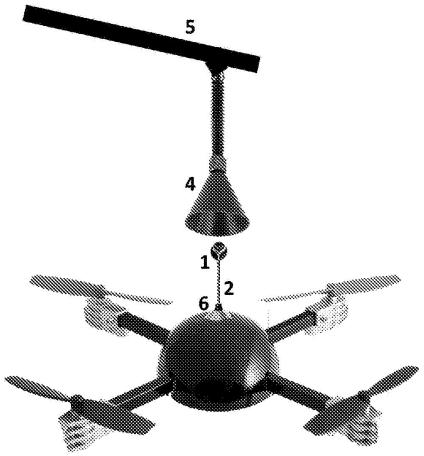

Source: Barbasov K.V.; Barbasov (2017)

create a stable landing gear for two-legged UAVs. This type of landing platform resembles a conical funnel for all legs, presenting lateral rails. Figure 9 presents the concept proposed by Mingxi Hanping and Yuan (2014), where the rails can change the tilt angle.

Figure 9 – Landing platform for UAVs with ski-type legs.

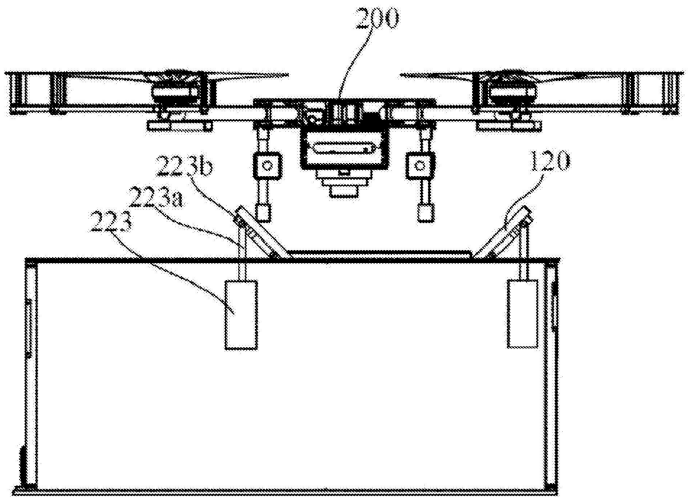

Source: Mingxi Hanping and Yuan (2014)

2.3 GRIPPERS

Monkman et al. (2007) define **grippers** as subsystems of handling mechanisms that provide temporary contact with the grasped object, ensuring the position and orientation of the workpiece. The name **gripper** is also used when grasping is not involved, but instead, it holds the workpiece in place with a retention force acting on a point, line,

or surface. Their application varies widely, from industrial robots handling heavy loads to hand-guided manipulators used in remote medical operations or clamping mechanisms used in manufacturing. Grippers can be categorized into four main groups: *impactive*, *ingressive*, *astrictive* and *contigutive*.

Figure 10 – Examples of grippers applications with UAVs.

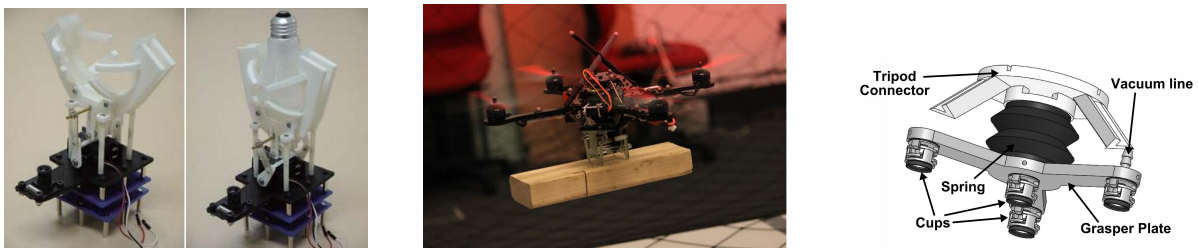

(a) Impactive gripper. (b) Ingressive gripper. (c) Vaccum gripper.

Source: Shimahara et al. (2016), Mellinger et al. (2013) and Kessens et al. (2016), respectively.

Impactive grippers are the most used grippers with a wide variety of technical applications. The grasping force provided by mechanical grippers is based on the effects of classical mechanics associated with mass points and forces. Grasping of the workpiece occurs by applying sufficient normal forces or using frictional forces, which requires that the payload geometry is compatible with the grippers (MOHIUDDIN et al., 2020). The fingers' motion is accomplished by converting some form of energy into mechanical energy (MONKMAN et al., 2007). Shimahara et al. (2016) attached an impactive gripper on top of a UAV, as presented in Fig. 10a to accomplish tasks like taking a light bulb off.

Ingressive grippers consist in penetrating to a given depth the surface of the object to be held or manipulated. There are applications in which the penetration does not occur, and the end-effector pinch the material. The ingressive technique differs from impactive grippers in maintaining the grasped object, i.e., impactive grippers must maintain the exerted force on the workpiece at all times, while ingressive grippers do not necessarily have to apply force after grasping the object. (MONKMAN et al., 2007). The main advantage of this gripping technique is that it can grasp objects without well-defined attachment points, and it does not require a full enclosure of the object for grasping (MOHIUDDIN et al., 2020). Mellinger et al. (2013) adopted ingressive grippers for cooperative transport of wood pieces using multiple UAVs, as presented by Fig. 10b.

Astrictive grippers provide a constant holding force without compressive stress, and the binding force is applied in a single direction. Different from many impactive grippers, almost all kinds of astrictive devices depend on some continuous energy supply (MONKMAN et al., 2007). The vacuum suction is an example of an astrictive gripper extensively adopted throughout the industry. Kessens et al. (2016) used a vacuum gripper, presented in Fig. 10c, attached to a UAV and successfully grasped a wide

variety of objects, such as eyeglasses, hairbrush, and wood blocks. Other examples are electroadhesion and magnetoadhesion.

Contigutive grippers rely on direct contact. The holding force can be chemical, thermal adhesion, or rely on the surface tension forces. Examples of this gripping technique being applied with UAVs have not been found in the literature.

2.4 LOCKING DEVICES

A locking device is a mechanism that switches the states of allowing or preventing relative motion between two parts. Such devices are widely used in robotics. Although there are multiple reasons for applying locking devices, the most recurrent ones are for energy management and reconfiguration (PLOOIJ et al., 2015). The fundamental principles of many locking mechanisms are quite old and have been extensively described in the literature (PLOOIJ et al., 2015). However, it is important to perform a comparative study in which the advantages and drawbacks of each device are easily evaluated. Therefore, it is possible to better determine which locking mechanism is the most suitable for a desired application. The information presented in this section, including the comparative study, was obtained from Plooij et al. (2015), which can be consulted for further details.

Naturally, the requirements of a locking mechanism may vary across different applications. However, it is necessary to evaluate each device based on a standardized set of requirements to perform a comparative study. The considered aspects were:

- *Adjustable locking directions:* the device is able to switch between locking its position in one or two directions;
- *Compactness:* the device should be small relative to its application;
- *High locking force:* the device has relatively high locking torque;
- *Inexpensive:* the device should be inexpensive relative to its application;
- *Lightweight:* the device should be lightweight relative to its application;
- *Lockable in any position:* the device has an infinite amount of locking positions, i.e., it can lock in any direction;
- *Low energy consumption:* The device should consume the minimal amount of energy possible, either when locking, unlocking or idle;
- *Short switching time:* the device switches instantaneously;
- *Unlocking while under load:* While there is a load on the locking device, it should still unlock.

Although many locking devices have been presented in the literature, they can be categorized based on their operating principle. The study conducted by Plooij et al. (2015) considered three main locking mechanisms: *mechanical locking*, *friction-based locking*, and *singularity locking*.

These three main locking mechanisms can be further divided based on the actuation form. Active devices use an actuator to define the locking timing, position, or locking torque. Passive devices rely on the position of a specific joint or link, the direction of a velocity, or external factors to perform the lock.

2.4.1 Mechanical locking

Mechanical locking devices use a blockage to keep the mechanism from moving. The position of a specific component determines the locking or unlocking. This section briefly describes existing mechanical locking devices.

Figure 11 – Examples of mechanical locks.

(a) Latch.

(b) Ratchet.

(c) Dog clutch.

(d) Cam-based lock.

Source: Own author.

Latches, presented in Fig. 11a, are composed of a pawl and a hook that can lock at a single position. They can be active, where an electronic actuator changes the position of the hook or the pawl to lock/unlock, or passive.

Active latches have been applied in several medical devices, such as the work of Karssen and Wisse (2012), who adopted a latch in the knee of a bipedal robot designed for running. Another example is the design of a genderless latching mechanism for modular robots, performed by Parrott, Dodd, and Groß (2014). Although latches generally lock in a single position, there are cases in which locking in multiple positions is possible. Mitsui, Ozawa, and Kou (2013) used a multi-locking latch in a robotic hand to lock joints in an underactuated finger. Passive latches are also present in the literature, such as in the work of Unal et al. (2010), who used them in an ankle-knee prosthesis.

Ratchets, presented in Fig. 11b, are composed of a round gear or linear rack with teeth and an actuated pawl that engages with the teeth and locks the system.

Active ratchets have an actuator that controls the pawl and determines engagement and disengagement. They are commonly used in prostheses, Geeroms et al. (2013), who applied an active ratchet in the weight acceptance mechanism in an active knee-ankle prosthesis. Passive ratchets may be actuated by a spring but have the drawback of allowing motion in only a single direction and preventing it in the opposite direction. They have been adopted by Li, Deng, and Liu (2009), who used it in an energy storage device for a spherical hopping robot.

Dog clutch, presented in Fig. 11c, consists of two parts of matching shapes. When both parts are engaged, the relative motion between them is blocked. When disconnected, however, the two parts can rotate independently.

Few applications of dog clutches in robotics were found, and all of them were actively actuated. Elliott et al. (2013) used an active dog clutch to attach and detach a parallel spring to a knee exoskeleton. Palpacelli, Carbonari, and Palmieri (2014) used dog clutches to lock degrees of freedom of spherical joints.

Cam-based locking devices, presented in Fig. 11d, are composed of two separate cam surfaces with complementary shapes. Even though it is possible to use active actuators, most examples found in the literature are passively actuated, where the position of the components locks the system. Mathijssen, Lefeber, and Vanderborght (2014) adopted a mutilated gear mechanism in a compliant actuator to lock parallel springs.

2.4.2 Friction-based locking

Friction-based locking devices use friction to prevent motion. This method is mainly known for its application in automotive brakes (disk brakes, drum brakes, and others). The connection of two friction surfaces determines if the joint is locked or unlocked. This connection may be determined by an actuator or may depend on the position of a joint or the direction of a velocity.

One advantage of friction-based mechanisms is the ability to lock at every position. However, since the normal force limits the friction intensity, most devices have some force amplifier. This section briefly presents the most common friction-based

locking devices, along with their advantages, disadvantages, and actuation type.

Figure 12 – Examples of mechanical locks.

(a) Electromagnetic brake. (b) Overrunning clutch. (c) Worm drive.

A well-known type of break used in robotics is the **electromagnetic brake**, presented by Fig. 12a. The principle of this device lies in an attractive force between a permanent magnet and an electromagnet, which engages two friction surfaces. Such brakes are relatively cheap and simple. However, since it relies on the activation of the electromagnet, this device is necessarily active and often consumes a significant amount of energy. Multiple robots use electromagnetic brakes to improve safety or reduce energy consumption. Hirzinger et al. (2001) added brakes on a robotic arm's joints to make sure the robot stands even when it is powered off, increasing its safety. On the other hand, Sugahara et al. (2002) added brakes on a bipedal robot to hold the joints in place while standing, lowering energy consumption.

An **overrunning clutch**, presented in Fig. 12b, is composed of an inner and outer raceway, with cylinders or rollers between both. The relative rotational speed of the two raceways determines if the clutch locks or not. They can be active, such as the bidirectional overrunning clutch designed by Hild, Siedel, and Geppert (2011). Or can be passive, as the miniature clutch designed by Controzzi, Cipriani, and Carrozza (2010) to apply in a robotic hand's fingers.

Nonbackdrivable gearings, presented in Fig. 12c, are gears that can only be driven from one side. This restriction occurs due to the shear friction, resulting in low efficiency. Since no actuator is required, they are naturally passive. These systems are adequate for avoiding energy losses and motor overheating by static load-cancellation. Gu, Ceccarelli, and Carbone (2009) used worm drives in the motors of a one-degree-of-freedom anthropomorphic arm.

2.4.3 Singularity locking

A position-dependent transfer ratio characterizes singularity locking devices. When the singular position is reached, such locking devices have an infinitely high transfer ratio, theoretically featuring an infinitely high locking torque, limited to the material's structural integrity and a small unlocking force.

The most popular approach to achieve singular positions is to use **four-bar linkages**. A classic example of a four-bar locking device are the locking pliers, presented in Fig. 13. Such devices typically have an input rotation and an output rotation or translation. As soon as a singular position is reached, it is impossible to open the lock by applying torque on the input rotation. Only an external force pushing the mechanism out of the singularity may open the system. The advantages of this locking device are the possibility to unlock even when the system is under heavy load and its low energy consumption. However, the locking position is only available in a single angular position. This locking mechanism was adopted by Van Oort et al. (2011) to lock the knee of a bipedal robot.

Figure 13 – Four-bar locking device (locking plier).

Source: Own author.

2.5 CHAPTER OVERVIEW

This chapter first presented the already explored load transport techniques. The first, defined as cable-suspended transport, consists of connecting the load to the UAV through a cable. Despite being an apparently simple solution, it generates passive degrees of freedom and control challenges. The second consists in grasping the load through grippers, claws, or robotic hands. This approach provides easier design options to grasp and deliver a package but compromises the UAV's agility. Section 2.2 presented a state-of-the-art survey of UAV docking devices. Section 2.3 presented some concepts and classification of grippers and how they have been employed with UAVs to carry objects. Finally, Section 2.4 presented the most used locking mechanisms and their use in robotics.

3 METHODOLOGY

Design is the creation of synthesized solutions in products or systems that meet previously determined requirements (TSAI, 2000). For a design problem, the objective is to make the best use of the professional's knowledge and available information to understand the problem better and generate as many feasible solutions as possible. These concepts are evaluated according to the desired characteristics, and the most promising concept is selected for analysis and optimization. This chapter describes the methodology adopted to design the UAV coupling mechanism. First, Section 3.1 describes the concepts of mechanical design requirements. Section 3.2 presents an overview of the number and type syntheses procedure. Section 3.3 presents the process for achieving a topology with optimized dimensions given the constraints imposed by the device's intended use. Section 3.4 briefly describes the static analysis through the Davies method. Section 3.5 presents the concept of a robust design and self-alignment. Finally, Section 3.6 draws the chapter's overview.

3.1 REQUIREMENTS

To facilitate the kinematic synthesis process, it is possible to take a systematic approach. Adopting a structured methodology for mechanism design reduces the development time and enhances the design quality. There are Several approaches to systemize mechanism design, such as Hartenberg and Denavit (1964), Yan (1998) and Murai (2019). This work closely follows the methodology proposed by Murai (2019), presented in Fig. 14.

A kinematic synthesis process consists in creating a new mechanism that satisfies specific desired characteristics, which are:

- Required features: mandatory features that the kinematic chain must accomplish. These features may be quantifiable specifications, such as mobility (M), the number of independent loops (v), and workspace order (λ), or well-established non-quantifiable specifications, such as joint types, symmetries, among other examples;
- Desired features: specify all desirable, quantifiable or non-quantifiable aspects, such as ergonomics and aesthetics. These features may be accomplished when possible but are not mandatory.

Murai (2019) divides the required features into four groups:

- *Functional requirements*: describe what the final device should do or how it should work. Examples of functional requirements are mechanical stiffness, simplicity,

Figure 14 – Mechanism design methodology proposed by Murai (2019)

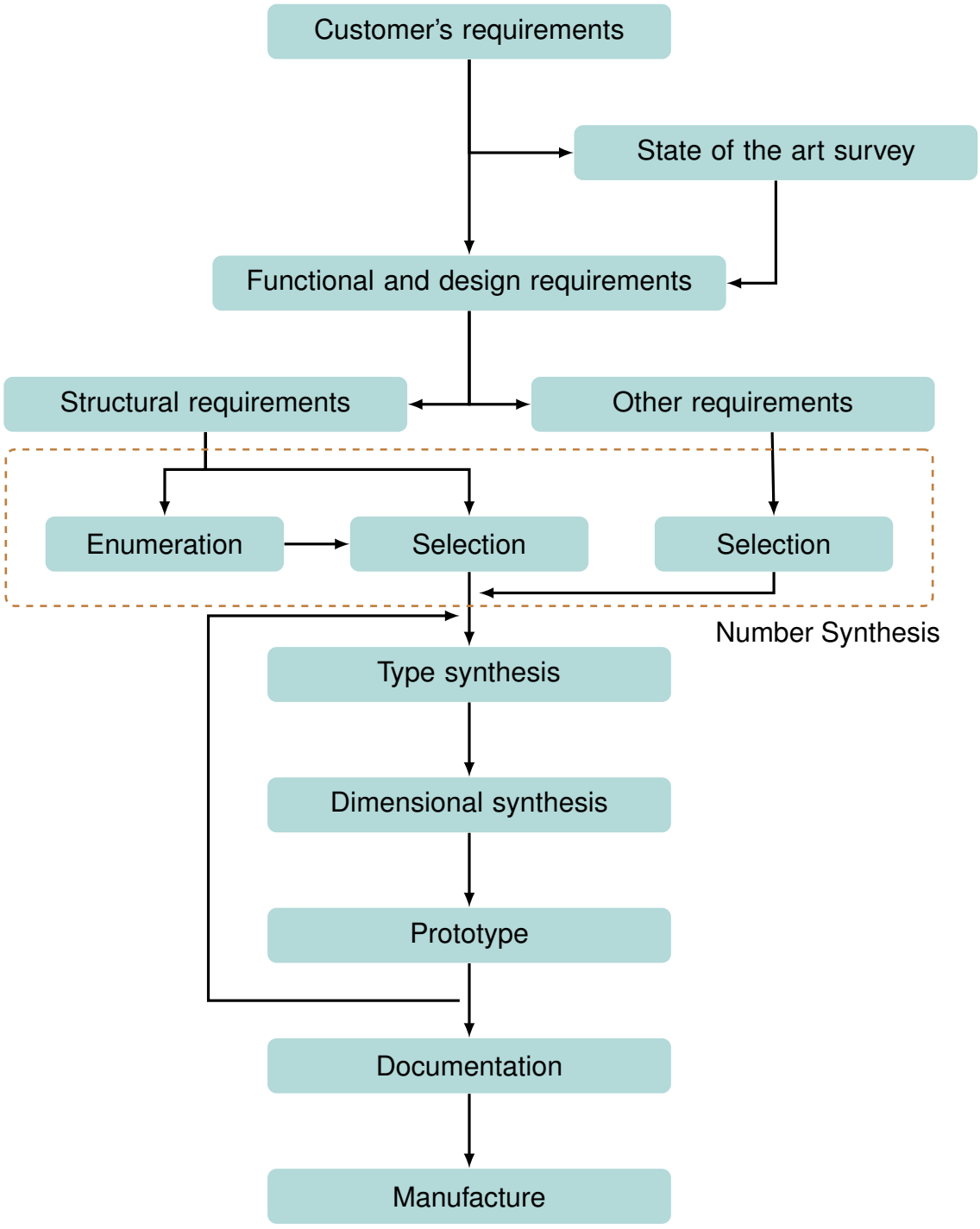

Source: Murai (2019).

size, and weight. These are aspects that can impact the design process regarding the number of independent loops, links, and actuators;

- *Design requirements*: are mandatory requirements for the design process but are not functions to be accomplished by the device itself. Examples of design requirements are manufacturing cost and designing time;

- *Structural requirements*: are mandatory characteristics on the kinematic chain structure, such as mobility, the number of independent loops, and workspace order;
- *Other requirements*: are functional or design requirements that could not be translated to structural requirements. These requirements are considered in the kinematic chain selection phase.

3.2 NUMBER AND TYPE SYNTHESES

The number synthesis starts with an initial set of structural requirements to define the number of links (n) and kinematic pairs (j). Then, it is determined how the links are connected, generating several kinematic chains that satisfy the structural requirements.

The first step in the number synthesis process is to verify the existing kinematic chains atlas available. Rosa (2018), Tsai (2000) and Yan (1998) present extensive atlas that should cover most of the planar synthesis problems.

However, if none of the available atlas include kinematic chains with the required structural characteristics, it is necessary to generate new kinematic chains. Simoni, Carboni, and Martins (2009) propose an enumeration method based on group theory tools and the analogy between graphs and kinematic chains, Murai (2019) proposes a method for the number synthesis development. Alternatively, it can be achieved through a chain enumeration capable software, such as Sagemath.

Type synthesis is a process to determine the type of each kinematic pair that composes the mechanism. At first glance, it is possible to employ any type of kinematic pair. However, several factors may narrow down the options. A few aspects that could be considered are:

- **Workspace order:** a planar kinematic chain ($\lambda = 3$), for instance, can only have revolute and prismatic pairs, and the orientation of these joints are also restricted;
- **Cost:** lowering the final cost is essential for any product, and it should be considered early in the design process;
- **Ease of maintenance:** the mechanism should be easy to repair. Higher kinematic pairs are often more complicated to manufacture and require frequent maintenance, which increases lifetime costs.

Once the available joints have been defined, the designer should evaluate every possible combination of these kinematic pairs in the kinematic chain. Since this is a combinatorial analysis problem, the number of possible results may be very high, and the analysis of each result would be a laborious task. Therefore, design requirements can be considered to reduce the number of results. The device application and form

of actuation are examples of requirements that might dictate which kinematic pair to adopt in certain positions.

After the type synthesis process is complete, it is possible to employ self-alignment concepts to the final mechanism. A self-aligning mechanism has the advantage of compensating for manufacturing imprecisions, reducing the final cost. The concept of self-alignment will be further discussed in Section 3.5.

3.3 DIMENSIONAL SYNTHESIS

The objective of the dimensional synthesis process is to determine the dimensions of the links to achieve a prescribed output motion. Prescribed output motion may include the path that a point of interest must travel, known displacements, or even higher order quantities, like velocities and accelerations (LEE; RUSSELL, 2018). The calculated dimensions may include the length and position of each link and joint coordinates.

This step can be divided into two subphases. First, a programmable mathematical model that describes the studied mechanism must be developed. This implies a series of equations that correctly represents the mechanism's elements. Second, an optimization process is applied to search for the best set of dimensions, so the mechanism behaves as intended.

3.3.1 Modeling methods

Figure 15 – Independent Coordinates.

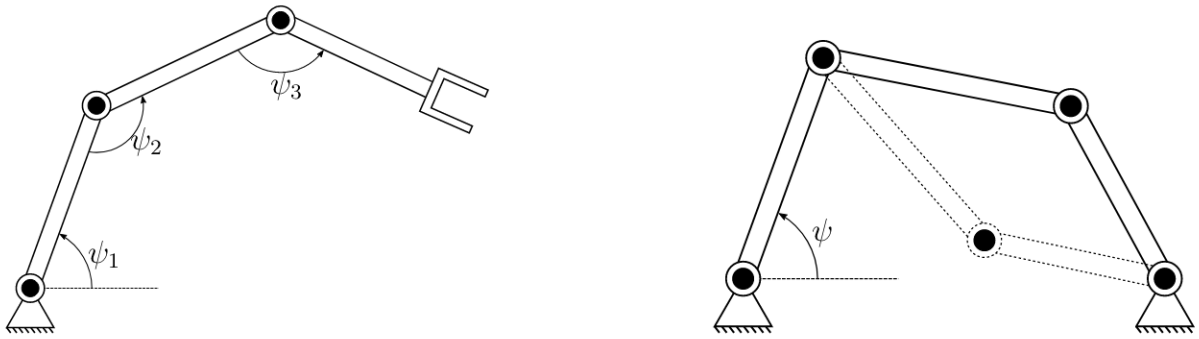

(a) Open-loop mechanism. (b) Closed-loop mechanism.

Source: Own author.

Independent coordinates could model a mechanism. In this case, the number of coordinates is equivalent to the mechanism's degrees of freedom. The advantage of this approach is the reduced number of equations required to define a mechanism position. However, the application of independent variables is most suitable to open-loop mechanisms. The example presented in Fig. 15a clearly shows that a 3-DOF open-loop

open-loop manipulator can be fully defined by the angles ψ_1, ψ_2 and ψ_3. On the other hand, a 1-DOF closed-loop chain, such as the four-bar mechanism presented in Fig. 15b, may achieve the same position by multiple paths, which a single variable cannot define. Therefore, independent variables for closed-loop mechanisms might result in an under-defined model.

To correctly represent a mechanism, it is necessary to know the position and motion of every rigid body. Therefore, an extended system of non-independent coordinates, capable of defining the mechanism unequivocally, is required. Different types of coordinates can be used to define a skeletal model, such as *relative coordinates*, *reference point coordinates* (also known as Cartesian coordinates), *natural coordinates* (also called fully Cartesian coordinates) or twist coordinates. Even though this text briefly describes each of them, further information is available in the works of Avello-Iturriagagoitia (2014) and De Jalon, Unda, and Avello (1986).

The *relative coordinates* method determines the position of every element concerning the previous one along the kinematic chain. The constraint equations are introduced as matrix products or vector equations that close independent kinematic loops. This method's drawbacks are the difficulty in manipulating the equations and the need to know the absolute values of position, velocity, acceleration, or inertia forces, which increases computational cost.

The *reference point coordinates* consist in fixing the position and angular orientation of each element in an absolute manner. Although there are some alternatives, the most direct and widely used is to define a reference system bonded to the element itself, using its origin to determine its translation, and Euler angles to determine its orientation. The restriction equations can be extracted by examining each pair of elements and describing its restrictions mathematically. The major drawback of this method is the singular positions, in which two of the angles become indeterminate.

The *natural coordinates* define each element's position absolutely. In this case, however, there is no need to define the angular orientation for each element, which reduces its complexity and avoids singularity issues. Because of its advantages and previous successful applications by Nuñez (2014), this work adopts the natural coordinates method. Therefore, it will be explored more thoroughly in this section.

The natural coordinates are composed of cartesian coordinates of a few points, which define a rigid body. For modeling a mechanism, these points are coincident with the joints. To model a mechanism correctly through natural coordinates, a few rules apply:

- Every joint must be considered a point;
- A rigid body must be composed of at least two points. Otherwise, it is not possible to determine the element's orientation.

Figure 16 presents two rigid bodies, where Fig. 16a represents a binary link, and Fig. 16b represents a ternary link. The modeling of a binary link can be achieved through a single equation, presented by Eq. 1. However, the ternary link requires one equation per side, totaling three equations to model it, as presented by Eq. 2.

Figure 16 – Example of natural coordinates modeling.

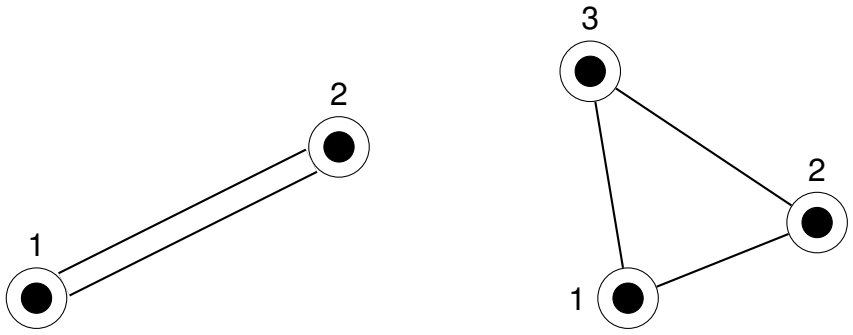

(a) Graph representation. (b) Kinematic chain.

Source: Own author.

$$(x_2 - x_1)^2 + (y_2 - y_1)^2 - L_{12}^2 = 0 \tag{1}$$

$$\begin{cases} (x_2 - x_1)^2 + (y_2 - y_1)^2 - L_{12}^2 = 0 \\ (x_3 - x_1)^2 + (y_3 - y_1)^2 - L_{13}^2 = 0 \\ (x_3 - x_2)^2 + (y_3 - y_2)^2 - L_{32}^2 = 0 \end{cases} \tag{2}$$

3.3.2 Optimization methods

To maximize gains and minimize losses has always been of great interest in many fields of science. The most common applications of optimization algorithms in engineering problems are energy conversion and distribution, logistics, and mechanical design (ALMEIDA; LEITE, 2019).

Engineering systems design may be a very complex process. Assumptions must be made to develop realistic models, which then must be verified by experiments. This process is highly iterative since it implies analyzing several trial designs until an acceptable design is accomplished.

There are several approaches capable of maximizing or minimizing a function. Despite the wide range of existing algorithms, no particular method is considered the best. Choosing which algorithm best suits the problem at hand depends on several characteristics, such as differentiability and concavity (ALMEIDA; LEITE, 2019). The designer must understand different approaches to identify which algorithm best fits the problem to select the most appropriate method.

It is possible to classify global optimization methods into two major categories: *deterministic*, which relies on an exhaustive search for the best solution, and *stochastic*, which involves random elements to determine the global optimum. Figure 17 summarizes the classification of these methods, and a brief description of each is presented.

Figure 17 – Optimization Methods.

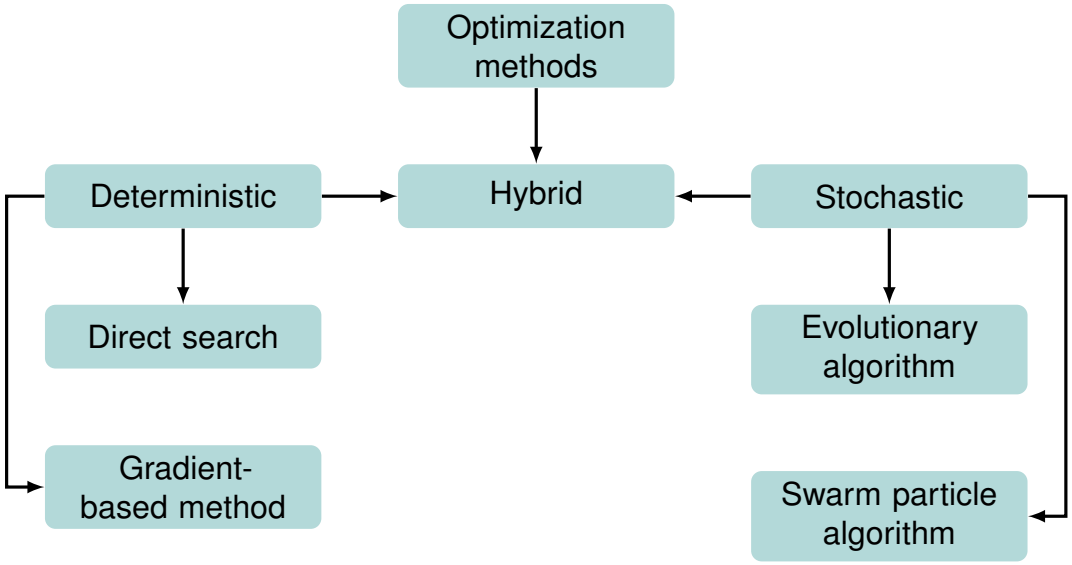

Source: Adapted from Nuñez (2014)

- **Direct search**: Although the functions are assumed to be continuous and differentiable, their derivatives are unavailable or even not trustworthy. Therefore, this method does not rely on the derivative of functions. Instead, only the functions' values are computed and used in the search (ARORA, 2004).
- **Gradient-based method**: The gradient is defined as a function, such as $\nabla f(x) = [\frac{\partial f}{\partial x_1} \frac{\partial f}{\partial x_2} \dots \frac{\partial f}{\partial x_n}]$. Since this method uses gradients of the problem functions to search for the best solution, it is assumed that all functions are smooth, and can be differentiated at least twice. Because only local information is used in the process, they converge only to a local optimum (ARORA, 2004).
- **Evolutionary algorithms**: Evolutionary methods are based on species evolution mechanisms, such as reproduction, mutation, recombination, and selection. Candidate solutions to the problem are considered individuals in a population, while the fitness function measures the quality of the solution.
- **Swarm particle algorithms**: The particle swarm optimization method is a metaheuristic algorithm based on the concept of swarm behavior, often seen in animal groups. It relies on shared information among the population to select the most suitable solution for the problem (ALMEIDA; LEITE, 2019).

The Genetic Algorithm method was selected for the development of this work based on many previously successful implementations in kinematic synthesis and optimization of mechanisms, including the ones by Nuñez (2014), Nariman-Zadeh et al. (2009) and Zhou (2009). Also, the following advantages, as described by Arora (2004), Haupt and Ellen Haupt (2004) and Weihmann (2013) were considered:

- compared to other techniques, GA is easy to apply and program;
- it applies to continuous, discrete, and non-differentiable problems;
- it is able to deal with large numbers of variables;
- simultaneously searches from a wide sampling of the cost surface.

3.3.3 Genetic algorithm

Genetic algorithms (GA) are categorized as *stochastic search optimization methods*, also known as *evolutionary methods* or *nature-inspired methods*. The genetic algorithm (GA) is an optimization algorithm based on genetics and natural selection (ARORA, 2004).

To better understand the Genetic Algorithm technique, let us consider an optimization problem with N_{VAR} variables, defined by a cost function and subject to a set of restriction functions. As stated previously, the goal is to search for the optimal solution in terms of the problem's variables.

The GA process begins with the definition of a *chromosome* as an array of variables to be optimized. Hence, if a N-dimensonal problem with p_1, p_2, $\ldots$, $p_{N_{VAR}}$ variables should be optimized, the chromosome would be written as in Eq. 3.

$$chromosome = \begin{bmatrix} p_1 & p_2 & p_3 & \ldots & p_{N_{VAR}} \end{bmatrix} \tag{3}$$

Since each chromosome represents a set of values for the problem's variables, a cost value is attached. This value can be computed by evaluating the cost function f for a given chromosome, as written in Eq. 4.

$$cost = f(chromosome) = f(p_1, p_2, \ldots, p_{N_{VAR}}) \tag{4}$$

The algorithm starts with a group of chromosomes, defined as the *population*. The population is organized in a matrix form, where each row represents a chromosome. Therefore, given an initial population of N_{pop} chromosomes, a $N_{pop} \times N_{var}$ matrix is obtained, as presented by Eq. 5.

$$pop = \begin{matrix} chromosome\ 1 \\ chromosome\ 2 \\ \vdots \\ chromosome\ N_{pop} \end{matrix} \begin{bmatrix} p_1 & p_2 & \dots & p_{N_{VAR}} \\ p_1 & p_2 & \dots & p_{N_{VAR}} \\ \vdots & \vdots & \ddots & \vdots \\ p_1 & p_2 & \dots & p_{N_{VAR}} \end{bmatrix} \tag{5}$$

To compute the values of $p_1, p_2, \ldots, p_{N_{VAR}}$, first the algorithm generates a random $N_{pop} \times N_{VAR}$ matrix. Then, each element of the pop matrix can be calculated through Eq. 6, where p_{high} and p_{low} are the higher and lower variable limits, and p_{random} is a random number that varies between 0 and 1.

$$p_i = (p_{high} - p_{low})p_{random} + p_{low} \tag{6}$$

Natural selection occurs through the survival of the fittest. Once the pop matrix is fully defined, the cost of each chromosome is evaluated and stored in a $1 \times N_{pop}$ vector. Then, these costs are ranked from lowest to highest, and only the best results are selected to continue, while the rest is discarded.

The selection rate (X_{rate}) is the fraction of the population that survives for the next steps. The number of chromosomes that will survive is computed by Eq. 7. Although the user defines the value of X_{rate}, which is somewhat arbitrary, it is important to note that keeping just a few chromosomes will limit the available genes in the offspring. On the other hand, keeping too many chromosomes allows higher-cost genes to pass through the next generations.

$$N_{keep} = X_{rate}N_{pop} \tag{7}$$

The *pairing* step occurs until there are enough offsprings to replace the discarded chromosomes. In this step, two chromosomes are selected by a uniform random number generator to produce two new offsprings. As an example, let us consider that the selected parents were $mom = [2\ \ 3]$ and $dad = [3\ \ 1]$. This means that the first element of the chromosome mom will mate with the first element of the chromosome dad, and the second element of the chromosome mom will mate with the second element of the chromosome dad.

The *mating* step begins by selecting a variable at random in the first pair of parents to be the crossover point (α). The parents' chromosomes are given by Eq. 8.

$$\begin{aligned} parent_{mom} &= [p_{m1}\ p_{m2}\ \dots\ p_{m\alpha}\ \dots\ P_{mN_{VAR}}] \\ parent_{dad} &= [p_{d1}\ p_{d2}\ \dots\ p_{d\alpha}\ \dots\ p_{dN_{VAR}}] \end{aligned} \tag{8}$$

Let β be a random number between 0 and 1. The selected variables are combined to generate new ones through Eq. 9, which will be part of the children chromosomes, presented by Eq. 10.

$$\begin{aligned} p_{new1} &= p_{m\alpha} - \beta[p_{m\alpha} - p_{m=d\alpha}] \\ p_{new2} &= p_{m\alpha} + \beta[p_{m\alpha} - p_{m=d\alpha}] \end{aligned} \tag{9}$$

$$\begin{aligned} offspring_1 &= [p_{m1}\ p_{m2}\ \ldots\ p_{new1}\ \ldots\ p_{mN_{VAR}}] \\ offspring_2 &= [p_{d1}\ p_{d2}\ \ldots\ p_{new2}\ \ldots\ p_{dN_{VAR}}] \end{aligned} \tag{10}$$

Most functions that require an minimization process have many local minimums. Occasionally, the GA may converge too quickly to a local minimum and cannot get the global minimum. Therefore, the algorithm is forced to explore other areas through *mutation*. This technique is a different way to evolve the population by introducing traits not present in the original chromosomes.

The number of chromosomes to be mutated is determined by Eq. 11, where μ is the percentage of mutated chromosomes. The new variables are calculated by Eq. 6.

$$N_{mut} = \mu N_{pop} \tag{11}$$

3.4 STATIC ANALYSIS

When a mechanism performs a given task, forces and torques are applied or supported. The static analysis allows the application of an action (or series of actions) over the mechanism's actuators and calculates the force applied to an external body. Alternatively, it is possible to compute the efforts to balance the system based on external input.

It is possible to solve the static analysis by various means, such as the vector method, Davies method, or Virtual Work Principle (TSAI, 2000). This work focuses on Davies method due to its advantages over the other options, like direct solution through matricial form and easiness to solve using computational techniques.

The Davies method adopts three fundamental concepts: the Kirchhoff laws, graph theory, and screw theory. Kirchhoff's laws, originally developed for solving electrical networks, were adapted by Davies (1981) to be applied in kinematic chains. Graphs are used to represent the kinematic chain's connectivity and establish the connection between the forces and velocities of the mechanism. Finally, the screws represent the position, forces, and velocities instead of the conventional vector representation.

3.4.1 Kirchhoff's laws

Kirchhoff's circuit laws are two equalities that quantify how current flows through a circuit and how voltage varies around a loop in a circuit. The first law, also known as Kirchhoff's current law, states that the current flowing into a node must be equal to the current flowing out of the same node. The second law, also known as Kirchhoff's voltage law, states that in any loop within a network, the sum of all voltages must be zero.

Davies (1981) establishes an analogy between a mechanism and an electrical circuit, considering account the similarities between a force and an electrical current and instantaneous velocity and voltage. This way, the adapted Kirchoff's laws are defined as:

Circuit law: The sum of the twists within a single closed loop equals zero.

Cutset law: The sum of the wrenches within a single cut equals zero.

This work is not concerned with instantaneous kinematics, and therefore will not be addressed. However, detailed information can be obtained from Davies (1981) and Cazangi (2008).

3.4.2 Graph theory

The application of graph representation eases the identification of independent loops, which define the static equilibrium equations (ERTHAL, 2010). A graph consists of a set of vertices connected through a set of edges. When representing a kinematic chain, the graph vertices represent the chain's links, while the edges may represent the chain's joints or embedded actions. Figure 18a presents a four-bar mechanism as an example, and Fig. 18b presents its respective graph representation, where the numbers identify the vertices, and the lower case letters identify the edges. A graph with edges that have a defined direction is called a directed graph, also known as a digraph. Figure 18c presents the digraph for the four-bar mechanism, in which the edges go from the lower to the higher number.

Figure 18 – Graph representation of a four-bar mechanism.

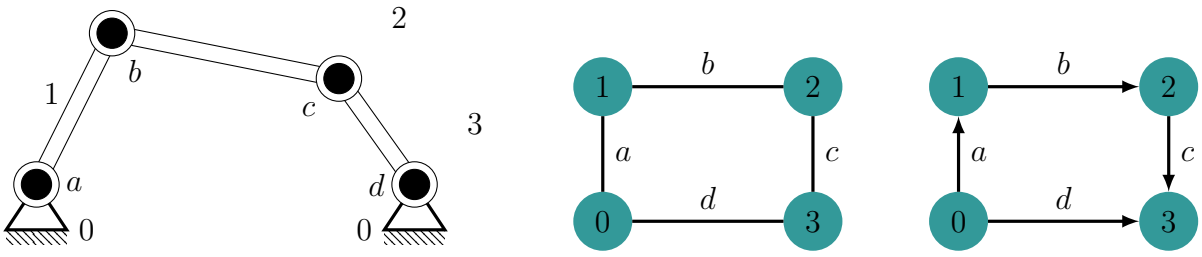

(a) Four-bar mechanism. (b) Four-bar graph. (c) Four-bar digraph.

Source: Own author.

A *path* is a sequence of vertices and edges, starting in a given vertice and finishing in another vertice. A *loop* is a path that starts and finishes in the same vertice. The graph presented in Fig. 18b and 18c starts at vertice 1 and finishes at vertice 1, creating a loop.

A *spanning tree* of a graph is a subgraph that contains all vertices of the original graph but does not create a loop. The edges that belong to the spanning tree are called *branches*, while the edges removed to create the spanning tree are called *chords*. For each chord, there is a corresponding loop.

A *cut*, denoted by the letter k, is a line that crosses a single branch and as many chords as necessary. For each branch, there is a corresponding cut. Therefore, the direction of a cut is defined as the direction of its respective branch. For the static analysis, the cuts are represented by the *cutset matrix*, $[\mathbf{Q}]_{k,e}$, where e is the number of edges, equivalent to the number of joints that compose the mechanism. Each element q_{ij} of the cutset matrix, where i represents the respective branch, and j represents the respective chord, may take on the values of 0, $+1$, or -1. The element q_{ij} of a branch is always equal to $+1$, while the element q_{ij} of a chord follows the pattern presented by Eq. 12.

$$q_{ij} = \begin{cases} 0, \text{if cut } i \text{ does not include edge } j; \\ +1, \text{if branch } i \text{ and chord } j \text{ shares the same direction;} \\ -1, \text{if branch } i \text{ and chord } j \text{ have opposite directions.} \end{cases} \tag{12}$$

Consider the four-bar mechanism from Fig. 18 as an example. Figure 19 presents the directed graph that represents the four-bar mechanism, where the black lines represent the branches, the red dashed line represents the chord, and each dashed brown box represents a cut.

Figure 19 – Graph representation of the four-bar mechanism with the respective cuts.

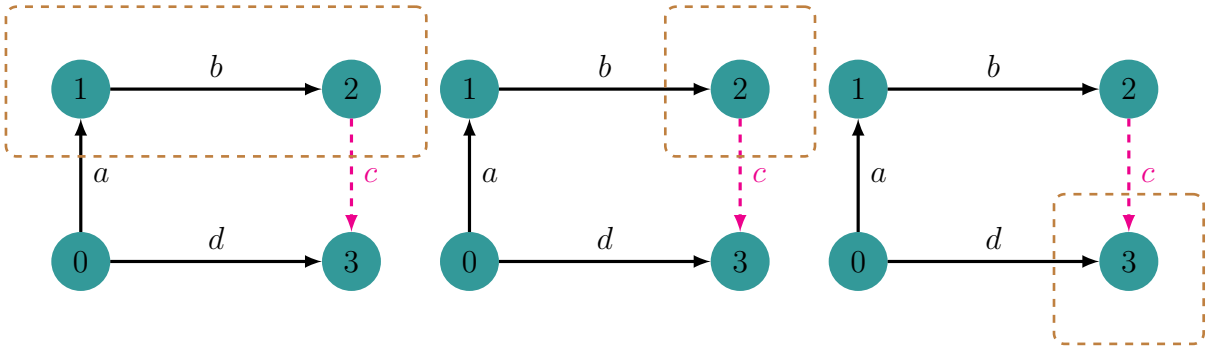

(a) cut a. (b) cut b. (c) cut d.

Source: Own author.

Figure 19a presents cut a. It can be seen that branch a is directed inward to the dashed brown box representing the cut, while chord c is directed outward. Therefore,

by following the rules presented by Eq. 12, it can be concluded that the element q corresponding to the chord c of cut a is -1. Similarly, Fig. 19c presents cut d, where the branch d is directed inward to the cut, and the chord c is also directed inward. Hence, the element q corresponding to the chord c of cut d is $+1$. Equation 13 presents the $\mathbf{Q}$ matrix of the four-bar mechanism built considering the graphs presented by Fig. 19.

$$\mathbf{Q} = \begin{array}{c} \\ \text{a} \\ \text{b} \\ \text{d} \end{array} \begin{array}{c} \begin{array}{cccc} \text{c} & \text{a} & \text{b} & \text{d} \end{array} \\ \begin{bmatrix} -1 & +1 & 0 & 0 \\ -1 & 0 & +1 & 0 \\ +1 & 0 & 0 & +1 \end{bmatrix} \end{array} \tag{13}$$

3.4.3 Screw theory

The concept of screw theory is a powerful mathematical tool, very convenient in kinematics and dynamics analysis of spatial mechanisms. A screw is composed of two three-dimensional vectors. It may denote the position and orientation of a spatial vector, the linear and angular velocities of a body, or a force and couple. When applied in mechanisms analysis, screw theory has the advantages of clear geometrical concepts, explicit physical meaning, and convenient algebraic calculation (HUANG; LI; DING, 2013).

Although the screw theory may perform both the kinematic and static analysis of a mechanism, this work only concerns the statics. Hence, the development of the motion analysis is not addressed. However, more information regarding both analyses may be obtained from Cazangi (2008) and Weihmann (2013).

An action screw $\$$, also known as a *wrench*, is defined by a unit direction vector ($\vec{S}$), a position vector ($\vec{S_0}$), an associated pitch h and a magnitude ψ. The unit direction vector describes the direction of a force or couple acting upon the mechanism. The position vector represents an arbitrary point of the screw axis relative to the origin of the coordinate system. The pitch is a scalar parameter that relates a force to a moment. Finally, the magnitude ψ quantifies the force or couple. This wrench definition is presented by Eq. 14.

$$\$ = \begin{bmatrix} \boldsymbol{S_0} \times \boldsymbol{S} + h\boldsymbol{S} \\ \boldsymbol{S} \end{bmatrix} \psi \tag{14}$$

When considering the application of pure forces, the pitch equals zero, $h = 0$. Then, Eq. 14 can be reduced to Eq. 15, where $\boldsymbol{F}$ and $\boldsymbol{M}$ are 3-dimensional vectors that indicate the force and moment, respectively. However, if the screw describes the action of pure moments, the pitch is considered equal to infinity, $h = \infty$, and results in Eq. 16.

$$\$ = \begin{bmatrix} \boldsymbol{S_0} \times \boldsymbol{S} \\ \boldsymbol{S} \end{bmatrix} \|\boldsymbol{F}\| = \begin{bmatrix} \boldsymbol{M} \\ \boldsymbol{F} \end{bmatrix} \tag{15}$$

$$\$ = \begin{bmatrix} \boldsymbol{S} \\ \mathbf{0} \end{bmatrix} \|\boldsymbol{M}\| = \begin{bmatrix} \boldsymbol{M} \\ \mathbf{0} \end{bmatrix} \tag{16}$$

The dimensional space in which the mechanism is represented is named *order of the screw system*, denoted by λ. A 3-dimensional mechanism, $\lambda = 6$, requires six independent wrenches to represent the actions. Expanding Equations 15 and 16 for each action in a spatial mechanism results in the vectors presented by Eq. 17.

$$\begin{aligned}
\$_{F_x} &= \begin{bmatrix} 0 & z & -y & 1 & 0 & 0 \end{bmatrix}^T F_x \\
\$_{F_y} &= \begin{bmatrix} -z & 0 & x & 0 & 1 & 0 \end{bmatrix}^T F_y \\
\$_{F_z} &= \begin{bmatrix} y & -x & 0 & 0 & 0 & 1 \end{bmatrix}^T F_z \\
\$_{M_x} &= \begin{bmatrix} 1 & 0 & 0 & 0 & 0 & 0 \end{bmatrix}^T M_x \\
\$_{M_y} &= \begin{bmatrix} 0 & 1 & 0 & 0 & 0 & 0 \end{bmatrix}^T M_y \\
\$_{M_z} &= \begin{bmatrix} 0 & 0 & 1 & 0 & 0 & 0 \end{bmatrix}^T M_z
\end{aligned} \tag{17}$$

It is possible to observe in Eq. 17 that the first three lines of a screw refer to the moments, and the last three refer to the forces. A planar mechanism with $\lambda = 3$, the only possible actions are the forces along the x and y axes and the moment around the z axis. Therefore, the first, second and last lines of the screws in Eq. 17 are always equal to zero. Hence, they can be simplified to Eq. 18.

$$\$_{F_x} = \begin{bmatrix} -y \\ 1 \\ 0 \end{bmatrix} F_x, \$_{F_y} = \begin{bmatrix} x \\ 0 \\ 1 \end{bmatrix} F_y, \$_{M_z} = \begin{bmatrix} 1 \\ 0 \\ 0 \end{bmatrix} M_z \tag{18}$$

Let C be the sum of constraints imposed by all joints that compose the mechanism. The wrenches vectors defined in Equations 17 and 18 can be bound together in a single unit action matrix $\boldsymbol{A_D}$, as shown by Eq. 19. The wrenches magnitudes are grouped in an *action magnitude vector*, Ψ, given by Eq. 20.

$$\mathbf{A_D} = \begin{bmatrix} \$_{\mathbf{F_x}} & \$_{\mathbf{F_y}} & \dots & \$_{\mathbf{C}} \end{bmatrix} \tag{19}$$

$$\boldsymbol{\Psi}_{C,1} = \begin{bmatrix} \psi_1 \\ \psi_2 \\ \vdots \\ \psi_C \end{bmatrix} \tag{20}$$

3.4.4 Davies method

Davies (1981) provided a method capable of systematically solving the kinematics and statics of mechanisms by adapting the Kirchhoff laws for electrical circuits, which results in a linear system of equations.

The static analysis through Davies method may be summarized in four steps:

- to construct the action graph and to assemble the $\boldsymbol{Q}$ matrix, as described in Section 3.4.2;
- to define the wrenches and assemble the $\boldsymbol{A_D}$ matrix, as described in Section 3.4.3;
- to compute the network action matrix $\boldsymbol{A_N}$ and define the linear system of equations;
- to identify the primary and secondary variables to solve the system of equations.

The *network action matrix*, $\boldsymbol{A_N}$ establishes the relationship between the C wrenches of the $\boldsymbol{A_D}$ matrix and the k cuts, defined by the cutset matrix $\boldsymbol{Q}$. Each line of $\boldsymbol{Q}$ informs which wrenches belong to the respective cut. The $\boldsymbol{A_N}$ matrix is assembled by distributing the wrenches belonging to each cut, multiplying the unit action matrix $\boldsymbol{A_D}$ to each line of the cutset matrix $\boldsymbol{Q}$. Cazangi (2008) presents a systematic approach to compute the $\boldsymbol{A_N}$ matrix, shown by Eq. 21, 22 and 23.

$$\boldsymbol{Q_1} = \begin{bmatrix} q_{1,1} & q_{1,2} & q_{1,3} & \dots & q_{1,C} \end{bmatrix} \tag{21}$$

$$diag\{\boldsymbol{Q_1}\} = \begin{bmatrix} q_{1,1} & 0 & 0 & \dots & 0 \\ 0 & q_{1,2} & 0 & \dots & 0 \\ 0 & 0 & q_{1,3} & \dots & 0 \\ \vdots & \vdots & \vdots & \ddots & \vdots \\ 0 & 0 & 0 & \dots & q_{1,C} \end{bmatrix} \tag{22}$$

$$\boldsymbol{A_N} = \begin{bmatrix} \boldsymbol{A_D} \cdot diag\{\boldsymbol{Q_1}\} \\ \boldsymbol{A_D} \cdot diag\{\boldsymbol{Q_2}\} \\ \vdots \\ \boldsymbol{A_D} \cdot diag\{\boldsymbol{Q_k}\} \end{bmatrix} \tag{23}$$

To satisfy the cutset law, the sum of all wrenches belonging to the same cut must be equal to zero. Therefore, the matrix $\boldsymbol{A_N}$ multiplied by the action magnitude vector $\boldsymbol{\Psi}$ is equal to zero, as presented by Eq. 24.

$$\boldsymbol{A_N \Psi} = \overrightarrow{\boldsymbol{0}} \tag{24}$$

Equation 24 is only solvable if matrix A_N is square. Hence, for an over-constrained mechanism, in which every external force is internalized, there is a required number of known variables C_n to fully define the system. The value of C_n may be calculated by Eq. 25.

$$C_n = C - \lambda k \tag{25}$$

To solve the statics, Eq. 24 must be manipulated, dividing the network action matrix in a primary $\boldsymbol{A_{N_p}}$ matrix, composed of the known variables wrenches, and secondary bmA_{N_s} network action matrix, composed of the unknown variables wrenches. Similarly, the magnitude vector $\boldsymbol{\Psi}$ is divided into primary $\boldsymbol{\Psi_p}$ and secondary $\boldsymbol{\Psi_s}$ magnitude vectors. As a result, Eq. 24 is transformed to Eq. 26.

$$\boldsymbol{A_{N_s}}\boldsymbol{\Psi_s} = -\boldsymbol{A_{N_p}}\boldsymbol{\Psi_p}. \tag{26}$$

3.5 SELF-ALIGNMENT

According to CARRETO (2010), constraining an element in more than six ways results in internal stress and deformation. An over-constrained mechanism is subject to more constraints than the workspace ($\lambda = 6$), so some degrees of freedom are constrained more than once (CARRETO, 2010). The assembly process of an over-constrained mechanism is more difficult by imprecisions of the manufacturing process, and the use of force is necessary to align the joints correctly. However, the use of force for joining elements causes elastic deformation, and the links are kept in constant internal stress.

Downey, Parkinson, and Chase (2003) define a robust design as a design that works correctly, despite its variations. These variations may result from manufacturing imprecisions, environmental effects, or even by the end-user. In mechanical assemblies, these variations propagate across the links' joints, which may result in the impossibility of achieving the final assembly or generating unnecessary stress to the material, as stated earlier. The self-alignment process eliminates redundant constraints of a mechanism and achieves a precisely constrained design, resulting in an assembly capable of canceling out possible variations.

This work adopts **Reshetov's table method** to eliminate a mechanism's over-constraints. This methodology consists of increasing the joint's degrees of freedom to improve the design and make it more reliable (RESHETOV, 1979). Reshetov's method is performed by filling Table 1 with all joints that offer a degree of freedom for the respective motion on the respective axis. If a linear freedom is missing on any axis, a rotation freedom around a different axis can replace it. The method considers that a loop can close with no problems if all six freedoms are present in that loop.

Table 1 – Reshetov's table.

Independent loop	
$\boldsymbol{R_x}$ =	$\boldsymbol{T_x}$ =
$\boldsymbol{R_y}$ =	$\boldsymbol{T_y}$ =
$\boldsymbol{R_z}$ =	$\boldsymbol{T_z}$ =

Source: Own author.

Reshetov's table method can be summarized in four steps. Filing Table 1 is the first. The second step is analyzing the filled table to spot if the mechanism has all six freedoms or not. If translation freedoms are missing, the third step is to replace them with rotational freedoms from the other axis. The fourth step is to determine the number of redundant constraints, given by the number of motions completely restricted. Similarly, the number of extra freedoms indicates the mobility of the mechanism.

Figure 20 – Reshetov's method example for an over-constrained mechanism.

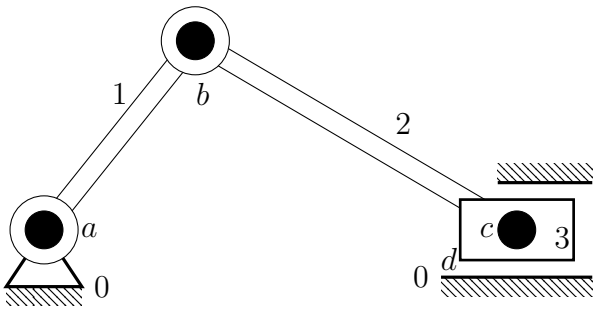

(a) over-constrained slider-crank mechanism.

Loop $abcd$			
$\boldsymbol{R_x}$ =	0	$\boldsymbol{T_x}$ =	d
$\boldsymbol{R_y}$ =	0	$\boldsymbol{T_y}$ =	0 (b)
$\boldsymbol{R_z}$ =	$a\ b\ c$	$\boldsymbol{T_z}$ =	0

(b) Reshetov's table.

Source: Own author.

Figures 20 and 21 presents the application of Reshetov's table method on an over-constrained slider-crank mechanism. Figure 20a illustrates a slider-crank mechanism composed of three revolute joints, denoted by the letters a, b and c, and a prismatic joint d. Filling Reshetov's table, as shown in Fig. 20b demonstrates that the mechanism has three rotational degrees-of-freedom around the z-axis provided by the revolute joints and a translational degree-of-freedom along the x-axis. Since there are extra rotational degrees-of-freedom around the z-axis, one of them can compensate for the missing translational freedom along the y-axis, as shown in Fig. 20b. Therefore, it can be concluded that the slider-crank mechanism has two rotational over-constraints (around the x and y axes) and a translational over-constraint along the z axis. Fur-

thermore, there is one extra rotational freedom around the z-axis, representing the mechanism's mobility.

Figure 21 – Reshetov's table method example for a self-aligning mechanism.

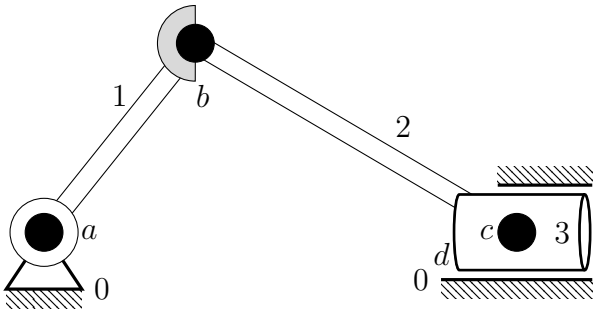

(a) Self-aligning slider-crank mechanism.

Loop $abcd$			
$\boldsymbol{R_x}$ =	$b\ d$	$\boldsymbol{T_x}$ =	d
$\boldsymbol{R_y}$ =	b	$\boldsymbol{T_y}$ =	$0\ (b)$
$\boldsymbol{R_z}$ =	$a\ b\ c$	$\boldsymbol{T_z}$ =	$0\ (d)$

(b) Reshetov's table.

Source: Own author.

In order to remove the mechanism's over-constraints, it is possible to replace one or more joints with ones that provide more degrees of freedom. A viable solution to the slider-crank would be to replace the revolute joint b with a spherical joint and the prismatic joint d with a cylindric joint, as illustrated in Fig. 21a. Filling Reshetov's table, presented in Fig. 21b, demonstrates that the new slider-crank has two rotational freedoms around the x-axis, one rotational freedom around the y-axis, three rotational freedoms around the z-axis, and one translational freedom along the x-axis. The extra rotational freedoms may compensate for the two lacking translational freedoms, as indicated in Fig. 21b, which results in a self-aligned mechanism.

3.6 CHAPTER OVERVIEW

This chapter presented the required tools to develop a novel topology for a UAV coupling mechanism. First, Section 3.1 established that the development of this work would follow the methodology proposed by Murai (2019). In addition, it was presented the concept of design requirements which serves as a basis for decision-making scenarios. Section 3.2 introduced the concept of number and type syntheses and drew the steps in this stage. Section 3.3 described a few methods for mathematically modeling a mechanism's topology and a few optimization methods. Section 3.4 briefly described the static analysis through Davies Method process, and the mathematical tools to apply it, such as graph theory and screw theory. Finally, Section 3.5 presented an overview of the self-alignment concept and described Reshetov's table method for evaluating and identifying a mechanism's redundant constraints.

4 DEVELOPMENT OF A UAV GRIPPING DEVICE

This chapter consists of developing the coupling device, following the steps described in Chapter 3. Section 4.1 lists the final mechanism's required and desirable characteristics based on the evaluation of the problem addressed and the information collected in chapter 2. Next, Section 4.2 presents the steps taken in the number synthesis and the logic used in the type synthesis to achieve the new topology. Section 4.3 presents the mathematical modeling of the new topology and the optimization process to achieve the optimal dimensions. Section 4.4 describes the static analysis of the optimized topology through Davies method. Finally, Section 4.5 draws some final considerations.

4.1 REQUIREMENTS

An initial analysis of the intended application was carried out and resulted in the following desired characteristics:

- **Mobility**: a single actuator should be able to fully open or close the mechanism. Therefore, the mobility should be equal to one ($M = 1$);
- **Weight**: since aerial transport is one of the objectives, the final mechanism should be as light as possible. Therefore, the number of links and loops should be minimized;
- **Actuation**: a fully passive mechanism is preferred. It would avoid the extra weight of active actuators and a battery, and the lack of an electronic circuit simplifies the final product;
- a vertical, downwards force should actuate the mechanism. This way, the UAV's weight could be used as the actuator;
- the final mechanism should fit between the UAV's landing gear.

Sections 2.1 and 2.2 presented an overview of existing devices that address the current studied issue, at least on some level. Although most of the already existing mechanisms previously discussed do not share the desired characteristics mentioned above, they meet some crucial requirements, which are:

- the workspace of the mechanism is inevitably spatial ($\lambda = 6$), mainly because of fluctuation forces generated during motion, which may have any direction;
- a locking mechanism should be embedded to hold the closed state during force fluctuation;

- a secondary actuation form should be included to open the gripper as the UAV detaches itself;
- the contact surface of the UAV to the gripper should have a geometry that assists the correct alignment;
- the final mechanism should be symmetric.

Since the mechanism's workspace is spatial and symmetric, it is possible to explore this symmetry to simplify the synthesis process. For the synthesis of robot hands, Tischler, Samuel, and Hunt (1995) argue that synthesizing separate fingers may save some effort, as the static equilibrium of the grasped object is still achieved by selecting a sufficient number of fingers. This way, the gripper's claws will be synthesized separately, considering a planar workspace ($\lambda = 3$).

As exposed by Murai (2019), in the synthesis early stages, defining the number of independent loops is a complicated task. At first, kinematic chains with the lowest number of loops are tested if they meet the design requirements. If not, a higher number of loops must be analyzed. Thus, kinematic chains with a single loop will be examined first to develop the gripper's claw.

Section 2.4 presented an overview of the existing types of locking mechanisms, along with their respective advantages and disadvantages. Hence, each claw will be developed with a singularity locking device, mainly due to the easiness of application in passive mechanisms. To preserve the freedom to apply as many locks as the designer judges necessary without compromising the number of claws, the locking device will be an independent loop. Therefore, the minimum number of independent loops is two ($\nu = 2$), one for the claw and one for the locking mechanism.

4.2 NUMBER AND TYPE SYNTHESES

As discussed in Section 3.2, the first step of the number synthesis process is to verify any kinematic chains atlas that satisfies the structural requirements. Tsai (2000) provides an atlas of planar linkages with the respective graph and kinematic chain representations. Figures 22 and 23 present the two options for a one-degree-of-freedom planar mechanism with two independent loops, the Watt kinematic chain and Stephenson kinematic chain, respectively.

As stated before, the actuation of the mechanism should be a downwards force, so the weight of the UAV itself could generate the closing motion. Therefore, a single prismatic joint must activate both the finger and locking device, which indicates that the actuator link is ternary.

Section 2.4.3 presented that the most common type of singularity locking devices is four-bar mechanisms. In this case, considering the actuator is a prismatic joint, the

Figure 22 – First option of a one-degree-of-freedom 2-loop mechanism (Watt kinematic chain).

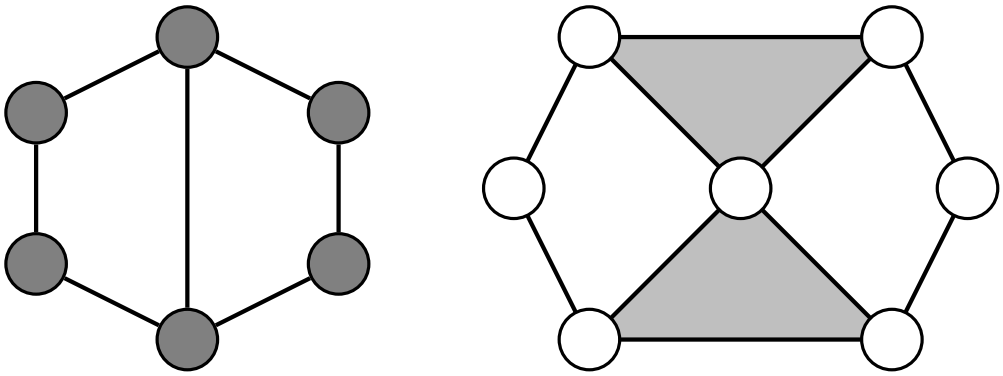

(a) Graph representation. (b) Kinematic chain.

Source: Own author.

Figure 23 – Second option of a one-degree-of-freedom 2-loop mechanism (Stephenson kinematic chain).

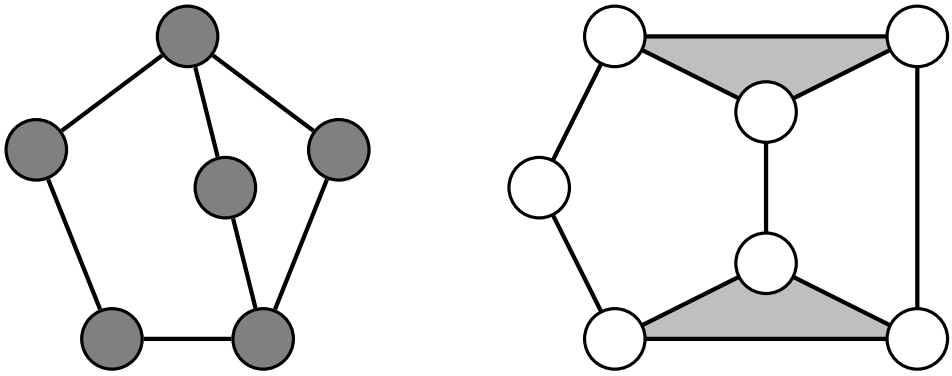

(a) Graph representation. (b) Kinematic chain.

Source: Own author.

locking device may be built as a slider-crank mechanism, as presented by Fig. 24a. Hence, the respective loop must have a revolute joint connected to the fixed frame.

The gripper's finger will support the entire cargo's weight during aerial transport. This way, it is essential that the link in contact with the UAV's gripping structure is also connected to the fixed frame, so the carried weight is better distributed.

So far, it has been established that the fixed frame must be a ternary link, connecting the locking device, the gripper's finger, and the actuated prismatic joint. The link that receives the external action (the UAV's weight) must also be ternary, responsible for transmitting the force to the locking device and the finger and connected to the fixed frame through the prismatic joint. From the atlas of planar linkages provided by Tsai (2000), the only kinematic chain that presents two ternary links connected by a single joint is presented by Fig. 22a.

The positioning of the UAV at the desired point on the coupling device begins

Figure 24 – First concept of each loop's topology.

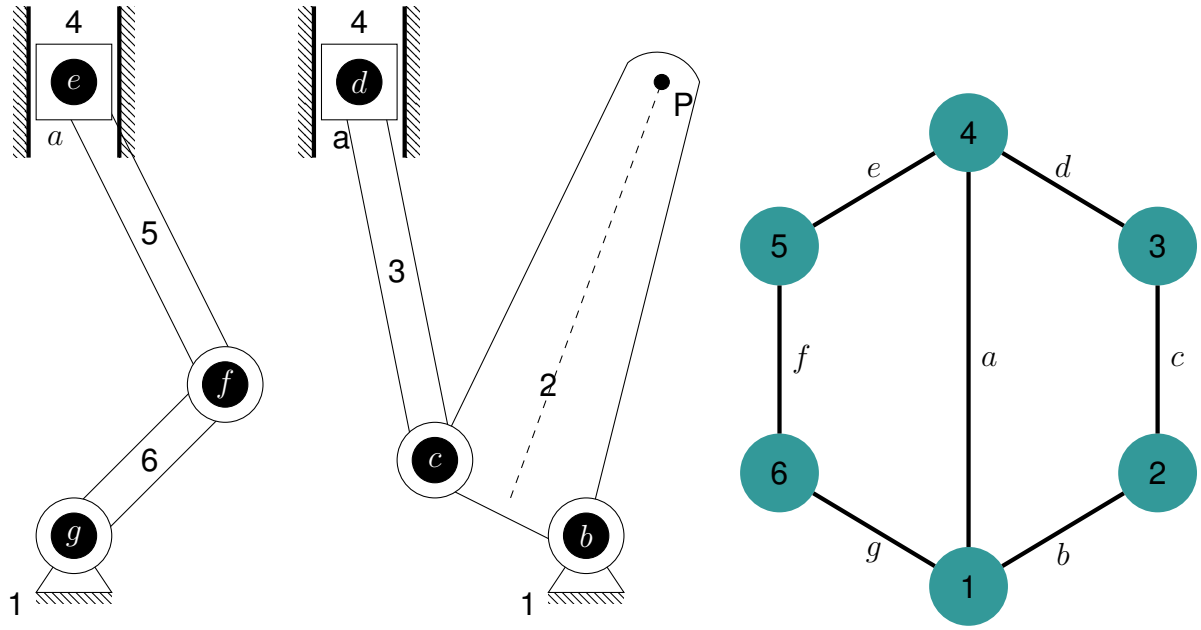

(a) Locker topology. (b) Finger topology. (c) Graph representation

Source: Own author.

during its flight, where it usually adjusts its position to land at a given point. The deviation between the desired landing position and the achieved position depends on the sensors installed in the vehicle, the chosen landing technique, the controlling system's performance, and other unpredictable external factors, such as meteorological conditions. As such, the occurrence of fluctuation of the UAV's position before landing. Therefore, the gripper's finger should be as far as possible from the UAV's gripping structure while landing and close only after achieving the correct alignment. A motion with the described characteristics can be achieved through a mechanism that resembles an eccentric slider-crank. Figure 24b presents an initial concept of the finger mechanism, where the letter P denotes a point of interest belonging to link 2, which may be interpreted as the end-effector.

Solenoids will be used to block joint f from any undesired motion to provide a safer lock. Figure 25 presents the system's working principle. As the gripper closes, joint f presses the solenoid's pin downwards, as illustrated in Fig. 25a and Fig. 25b. Once joint f passes the solenoid's pin position, the solenoid's spring returns the pin to its original position, which in turn acts as a blockage to keep joint f from moving, as illustrated in Fig. 25c.

4.3 DIMENSIONAL SYNTHESIS

This section presents the dimensional synthesis developed for the topology achieved in Section 4.2. The procedure follows the description presented in Section 3.3.

Figure 25 – Solenoid's locking system.

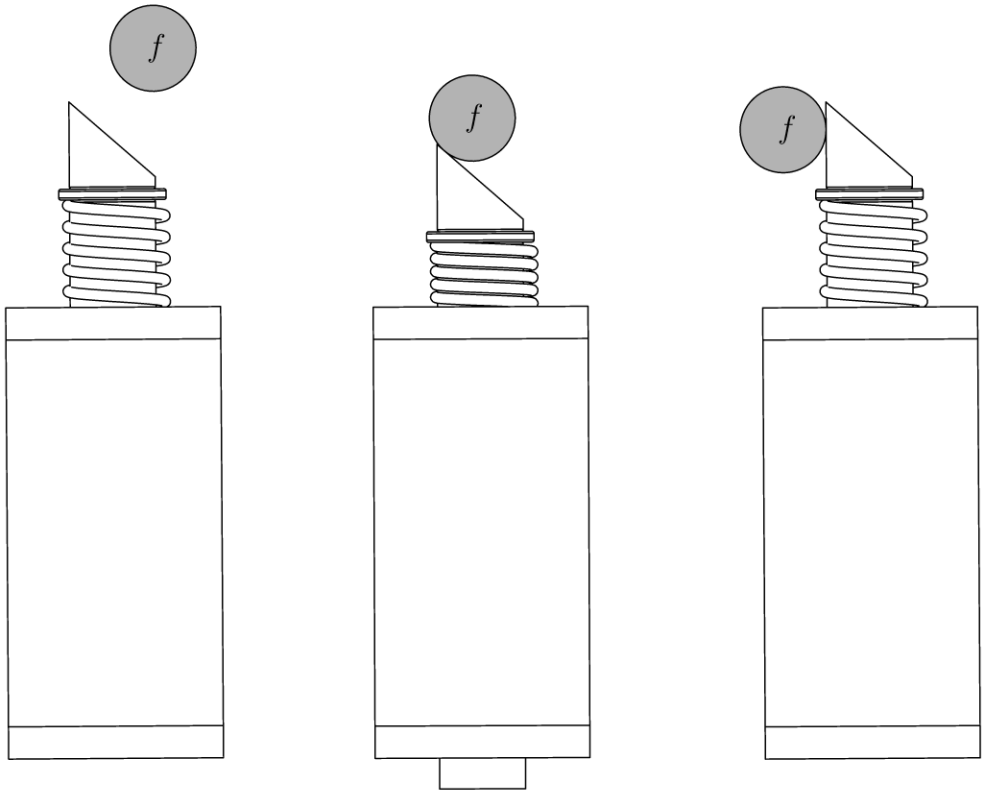

(a) Open mechanism. (b) Closing motion. (c) Closed mechanism.

Source: Own author.

However, a few tasks specific to the current design had to be added.

Using a torsion spring on joint g has two major objectives: to soften the closing motion and serve as an actuator for the opening motion. Therefore, the torsion spring dimensioning is directly linked to the forces supported by the links and the torque generated on joint b. The spring stiffness should be defined in such a way that, as the gripper closes, the resulting torque in joint b gets softer. Additionally, the spring constant should be high enough to generate the opening motion. Hence, it is necessary to estimate the weight of the links and evaluate if the final mechanism can perform both closing and opening motions smoothly. Figure 26 presents the flowchart of the adapted dimensional synthesis process.

Figure 27 presents a preliminary CAD model of the topology achieved in Section 4.2. Although this model does not consider the results of the dimensional optimization, it was possible to validate the motion and functionality of the topology.

The gripping device is expected to fit in the internal region of the landing gear. Therefore, it is necessary to adopt a UAV model to serve as a basis for the geometrical constraints. This work considered the information of a DJI Spreading Wings S900, presented in Fig. 28, but the optimization method is replicable to any other UAV.

Figure 26 – Adapted dimensional synthesis flowchart.

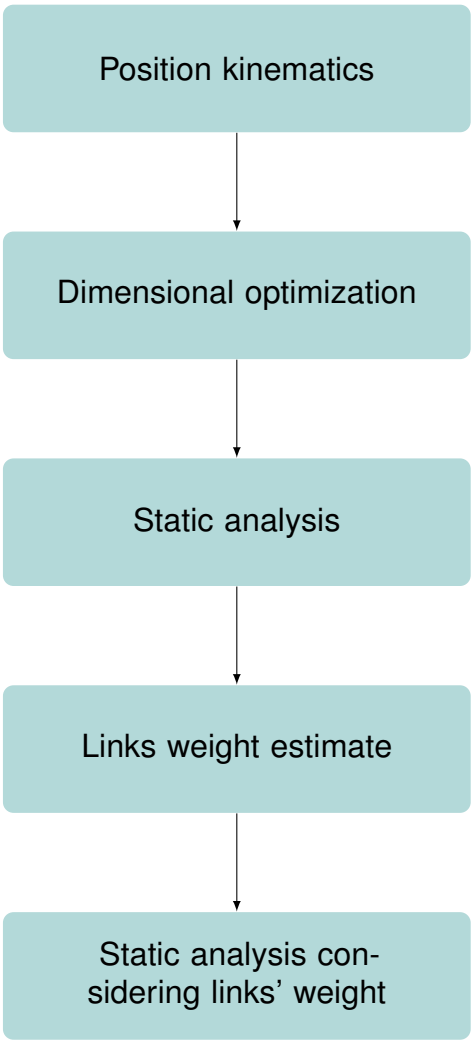

Source: Own author.

4.3.1 Position kinematics

Figure 27 presents the topology of the mechanism in its open state. Applying the Natural Coordinates procedure described in Section 3.3 would result in system of ten equations. However, the dimensions of the links $a - d$, $a - e$, $a - g$ and $d - e$ may be directly defined by the designer. Therefore, the system of equations is reduced to six equations, as shown by Eq. 27.

Even though the links' dimensions are unknown, the analysis of Fig. 27 provides some information regarding the mechanism's behavior. The coordinates of joints b and g are fixed and may be determined through the optimization process. The coordinates of joints d and e follow the displacement of the prismatic joint a and, therefore, can be determined directly. The dimensions of links L_2, L_3, L_5, L_6, L_{b-P} and L_{c-P} will be determined through the optimization process. Hence, the unknown variables of Eq. 27 are the coordinates of joints c, f and point P, represented by vector $\boldsymbol{q}$.

Figure 27 – Gripper mechanism dimensions.

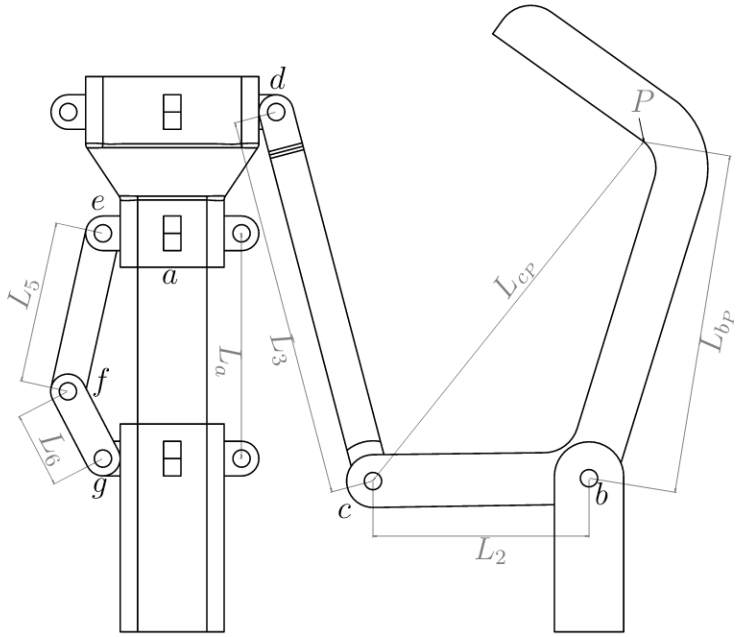

Source: Own author.

Figure 28 – DJI Spreading Wings S900

Source: DJI official website.

$$\mathbf{\Phi} = \begin{bmatrix} (x_b - x_c)^2 + (y_b - y_c)^2 - L_2^2 \\ (x_c - x_d)^2 + (y_c - y_d)^2 - L_3^2 \\ (x_b - x_P)^2 + (y_b - y_P)^2 - L_{b-P}^2 \\ (x_c - x_P)^2 + (y_c - y_P)^2 - L_{c-P}^2 \\ (x_e - x_f)^2 + (y_e - y_f)^2 - L_5^2 \\ (x_f - x_g)^2 + (y_f - y_g)^2 - L_6^2 \end{bmatrix} = \mathbf{0} \tag{27}$$

$$\mathbf{q} = \begin{bmatrix} x_c & y_c & x_f & y_f & x_P & y_P \end{bmatrix}^T \tag{28}$$

Finally, it is possible to calculate the jacobian of vector $\mathbf{\Phi}$, presented by Eq. 29. As a result, the Newton-Raphson can be applied to determine the joints' position in the entire range of motion.

$$\mathbf{\nabla \Phi} = \begin{bmatrix} 2x_c - 2x_b & 2y_c - 2y_b & 0 & 0 & 0 & 0 \\ 2x_c - 2x_d & 2y_c - 2y_d & 0 & 0 & 0 & 0 \\ 0 & 0 & 2x_f - 2x_e & 2y_f - 2y_e & 0 & 0 \\ 0 & 0 & 2x_f - 2x_g & 2y_f - 2y_g & 0 & 0 \\ 0 & 0 & 0 & 0 & 2x_P - 2x_b & 2y_P - 2y_b \\ 2x_c - 2x_P & 2y_c - 2y_M & 0 & 0 & 2x_P - 2x_c & 2y_P - 2y_c \end{bmatrix} \tag{29}$$

4.3.2 Topology optimization

Although the idea of a dimensional optimization process is to find a solution that best fits the desired outcome, some design parameters have to be determined before the optimization to define the mechanism's topology better and reduce computational costs. The height of the closed gripper is set to 130 mm, without considering the link's thickness. Although this definition is somewhat arbitrary, keeping the mechanism in the lower portion of the landing gear provides a wider range of motion and avoids the possibility of collision to the UAV's battery. The coordinates for joint d are also set to $x_d = 30$ mm and $y_d = 110$ mm, considering that the coupler attached to the UAV is 20 mm thick. Hence, the desired position for the end-effector in a closed state is $x_{P_{desired}} = 40$ mm and $x_{P_{desired}} = 130$ mm. Finally, the range of motion of the prismatic joint was set to be 40 mm.

Considering the definitions above and analyzing Fig. 27, it can be observed that loop $aefg$ has only two unknown variables, L_5 and L_6. Since the range of motion of the prismatic joint a is defined, it is possible to calculate the dimension of these links directly. The detailed procedure adopted for dimensioning the links of the locking mechanism will be presented in Section 4.3.3. Therefore, the optimization process is only applied to loop $abcd$, and Eq. 27 is reduced to 30.

$$\mathbf{\Phi} = \begin{bmatrix} (x_b - x_c)^2 + (y_b - y_c)^2 - L_2^2 \\ (x_c - x_d)^2 + (y_c - y_d)^2 - L_3^2 \\ (x_b - x_P)^2 + (y_b - y_P)^2 - L_{b-P}^2 \\ (x_c - x_P)^2 + (y_c - y_P)^2 - L_{c-P}^2 \end{bmatrix} = \mathbf{0} \tag{30}$$

The optimization variables are L_2, L_3, L_{c-P} and the coordinates for joint b. The value of L_{b-P} can be calculated by Eq. 31. As described in Section 3.3.3, vector $\mathbf{z}$ is composed of all variables that must be optimized, as exposed by Eq. 32.

$$L_{b-P} = \sqrt{(x_{P_{desired}} - x_b)^2 + (y_{P_{desired}} - y_b)^2}. \tag{31}$$

$$\boldsymbol{z} = \begin{bmatrix} L_2 & L_3 & L_{c-P} & x_b & y_b \end{bmatrix}^T \tag{32}$$

Generally, the cost function is composed of the error between the achieved path of the end-effector and the desired path. The path is known to be circular, where the center of the circle is the coordinates of joint b and the radius is the distance of joint b to the end-effector, which are not known. Therefore, it is not possible to fully define the desired path. Although the desired path is not known beforehand, it is possible to define that, in the closed position, the end-effector is positioned right above joint d. This way, it is possible to define that the quadratic error between the desired position and the achieved position when the gripper is closed should be minimal. Then, the cost function $f(\mathbf{q})$ is defined by Eq. 33.

$$f(\mathbf{q}) = (x_P - x_{P_{desired}})^2 + (y_P - y_{P_{desired}})^2, \tag{33}$$

As described in Section 4.1, when the gripper is closed, it lies inside the UAV's landing gear, which is also supported by the lower surface. Hence, the length of the links must be a suitable size. Also, collisions of the coupling device's finger with the landing gear during the closing motion should be avoided. Figure 29 presents the UAV's landing gear dimensions. This way, it is possible to determine the maximum x_P coordinate to avoid collision based on the y_P coordinate through Eq. 34.

Figure 29 – DJI Spreading Wings S900 landing gear dimensions.

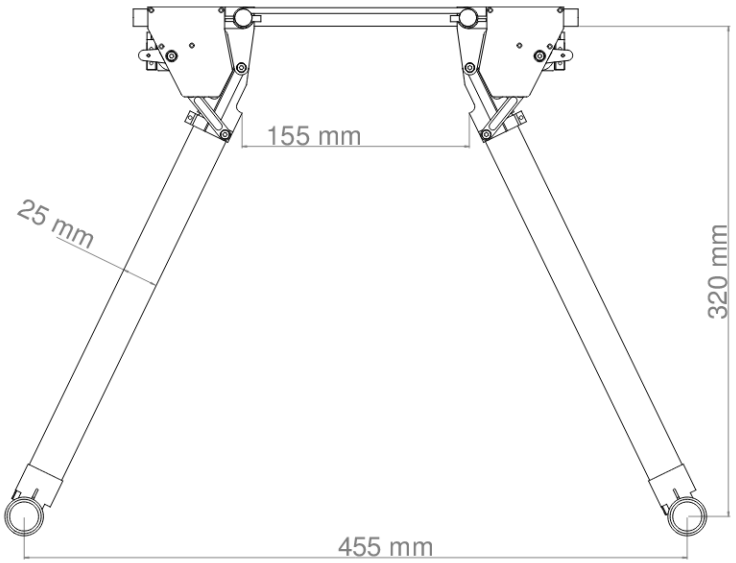

Source: Adapted from the DJI official website.

$$x_{P_{limit}} < \frac{485.32 - y_P}{2.13}. \tag{34}$$

The transmission quality μ is an indicator of the mechanism's effectiveness. It may be determined by measuring the angle between links L_5 and L_6. Martins and Murai (2019) recommend that the angle μ stays between 40° to 140°. Hence, the transmission quality can be calculated through the cosine law, presented by Eq. 35.

$$\mu = cos^{-1}\frac{L_{bd}^2 - L_3^2 - L_2^2}{2L_2L_3}, \tag{35}$$

where L_{bd} is the distance between joints b and d.

There is nothing to be optimized on the path traveled by the end-effector as the gripper opens. There are, however, some limits imposed by the UAV's landing gear. These limits are added to the cost function as $P(\mathbf{q})$ penalty functions. Then, if the results obtained in a given iteration break these limits, the cost function suffers a penalty, so the GA tries to avoid these problems in the next iterations. This way, the optimization problem can be rewritten as Eq. 36.

$$\text{minimize } f(\mathbf{q}) + \sum_{1}^{n} P(\mathbf{q}) \tag{36}$$

where n is the number of penalty functions. The gripping device has two boundaries. The first one is regarding the landing gear dimensions, which has to respect the limits imposed by Eq. (34) to avoid a collision between the gripper's finger and the landing gear. The second one is regarding the transmission quality μ, given by Eq. (35). Even though it is not mandatory, μ should be close to the recommended range. The penalty functions were the quadratic error between the achieved and limit values, multiplied by a factor k, as presented by Eq. 37 and Eq. 38. This work considered $k_1 = 1000$ and $k_2 = 100$.

$$P_1 = k_1(x_p - x_{p_{limit}})^2 \tag{37}$$

$$\begin{cases} P_2 &= k_2(\mu - 40°)^2, \text{ or} \\ P_2 &= k_2(\mu - 140°)^2 \end{cases} \tag{38}$$

4.3.3 Locking mechanism

The locking device does not require a specific path, and although it is subject to geometrical restrictions, there is not a need for an optimization process. The coordinates for joint e for the opened position were set to $x_e = 20$ mm and $y_e = 115$ mm, and the coordinates for joint g were set to $x_g = 20$ mm and $y_g = 50$ mm.

In order to reduce the mechanism's total weight, the length of the components should be minimum. For a fully open state, it is desirable to have high effectiveness of the force transmission from L_5 to L_6. Therefore, the transmission angle μ_{op} was set to be in the upper limit suggested by Martins and Murai (2019).

The concept of a singularity lock would require a perfect alignment of links L_5 and L_6. However, since the mechanism does not have active actuators, the opening process to detach the UAV could be complicated. In addition, locking can be achieved by getting close to the singularity. Therefore, the angle between L_6 and the central base is set to $10°$.

Figure 30 – Locking device variables.

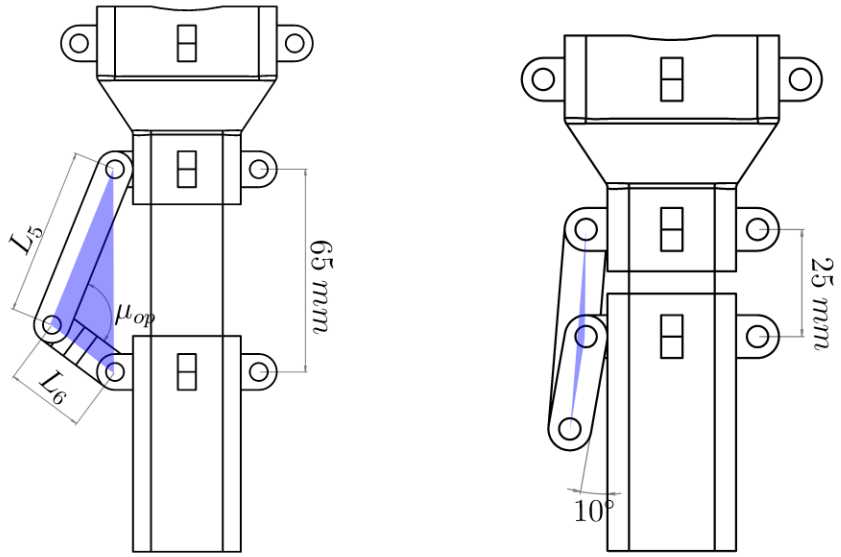

(a) Open mechanism. (b) Closed mechanism.

Source: Own author.

Figure 30 presents the locking device in its open and closed states. The blue triangles highlight the shape formed by the links in each state. Applying the cosine law to both triangles results in Eq. 39. Since this is a non-linear system of equations, it can be solved using an iterative method, such as Newton-Raphson.

$$\begin{cases} L_a^2 = L_5^2 + L_6^2 - 2L_5L_6cos(\mu_{op}) \\ L_5^2 = L_a^2 + L_6^2 - 2L_aL_6cos(170°) \end{cases} \tag{39}$$

4.3.4 Dimensional synthesis results

A new CAD model was developed considering the results of the optimization process. Figure 31 presents the new CAD model inside the landing gear in three positions. The path achieved by point P is also presented. It can be seen that the gripper's finger can be positioned inside the landing gear, and, as the UAV detaches, the trajectory of point P does not intersect with the landing gear's position at any time.

Since the mechanism accomplishes the desired motion when constructed with the dimensions obtained from the optimization process without colliding with the landing gear, it can be concluded that the dimensional optimization of the finger had satisfactory

Figure 31 – CAD model with the optimized dimensions.

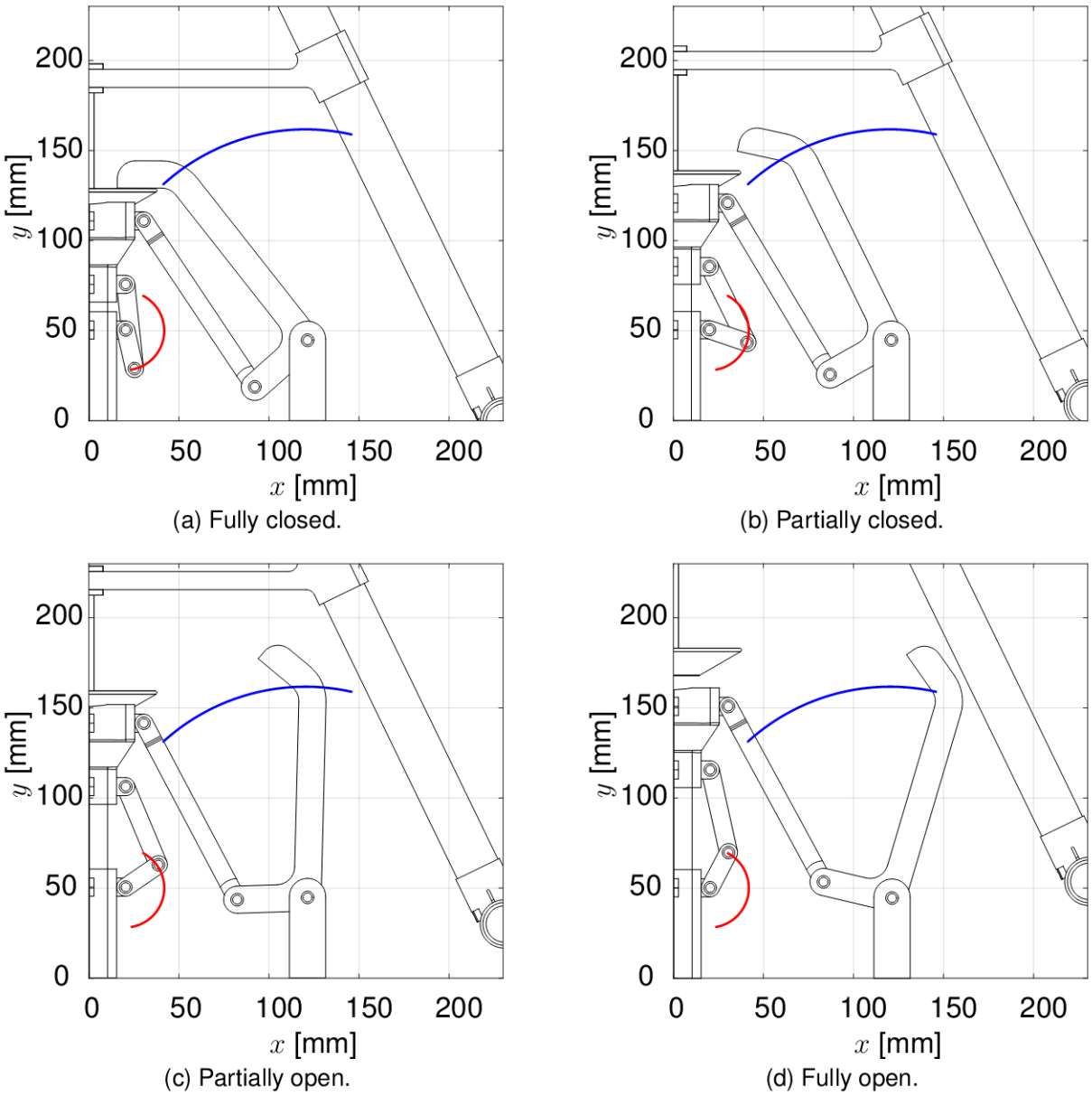

(a) Fully closed.

(b) Partially closed.

(c) Partially open.

(d) Fully open.

Source: Own author.

results. Table 2 presents the resulting dimensions. The transmission angle μ varied from $82°$ to $131°$, respecting the required range.

Table 2 – Results obtained from the Genetic Algorithm.

L_2 [mm]	L_3 [mm]	L_{c-P} [mm]	x_b [mm]	y_b [mm]
38.82	110.10	123.31	120.29	44.33

Source: Own author.

The dimensions obtained from the direct calculation of links L_5 and L_6 were also satisfactory, since there are no collisions to other links, and tghe mechanism performs

the expected motion. Table 3 presents the results.

Table 3 – Results obtained for the locking device.

L_5 [mm]	L_6 [mm]
46.70	21.88

Source: Own author.

4.4 STATIC ANALYSIS

Figure 32 presents the mechanism topology while a UAV DJI S900 lands on it. However, the thickness of the links is still arbitrary and may not represent the actual proportion. As a result, the static analysis of the mechanism must be performed. Once the load in each joint and consequently in the links are known, it is possible to estimate the links' cross-section area. This analysis considers the final mechanism to have four fingers equally distributed around the centered prismatic joint. It is also considered that the UAV's weight is evenly distributed to all fingers. Hence, the force applied to the prismatic joint is equivalent to one-fourth of the total weight.

To estimate the links' cross-section area, the highest forces should be considered. As exposed in Section 4.1, the gripper could be used to transport the gripper-UAV system through a ground vehicle and for aerial transport, in which the gripper must withstand the cargo weight. Therefore, the static analysis is performed for the closing motion, as the UAV lands on top of the mechanism, and for an aerial transport scenario. The dimensioning of the links' section area will consider the highest loads of each joint.

As mentioned in Section 4.1, the torsion spring positioned in joint g serves as an actuator for the opening motion. Once the links' cross-section area has been defined, it is possible to estimate the bodyweight of the elements. Hence, it is possible to evaluate if the spring is capable of returning the mechanism to its initial state.

The mechanism comprises prismatic and revolute joints, imposing two constraints and one degree of freedom per joint. Since the mechanism is planar ($\lambda = 3$), all wrenches have the format presented by Eq. 18.

As mentioned in Section 3.4, the external actions must be internalized. Therefore, the torsion around the z axis generated by the torsion spring positioned in joint g and the external force applied to the gripper must be implemented in the same manner as the reaction forces of the joints.

4.4.1 Landing motion

Figure 33a presents the gripper's topology and the external forces W and T_{g_z}. As mentioned in Section 4.1, one primary function of the torsion spring in joint g is to soften the closing motion. Hence, it is expected that, as the gripper closes, the torque

Figure 32 – Topology achieved.

(a) DJI S900 landing on top og the gripper.

(b) UAV fully attached.

Source: Own author.

generated in joint b gets closer to zero. T_{b_z} is considered an output of the system to evaluate the behavior of the generated torque in b.

Figure 33b presents the graph representation of the gripper's mechanism, with the respective external actions. As exposed in Section 3.4.2, defining the graph's chords and branches is necessary. Figure 34 presents five graphs, each representing one of the cuts. The edges denoting joints d and e, represented by the red dashed lines, were

Figure 33 – Forces acting on gripper during landing motion.

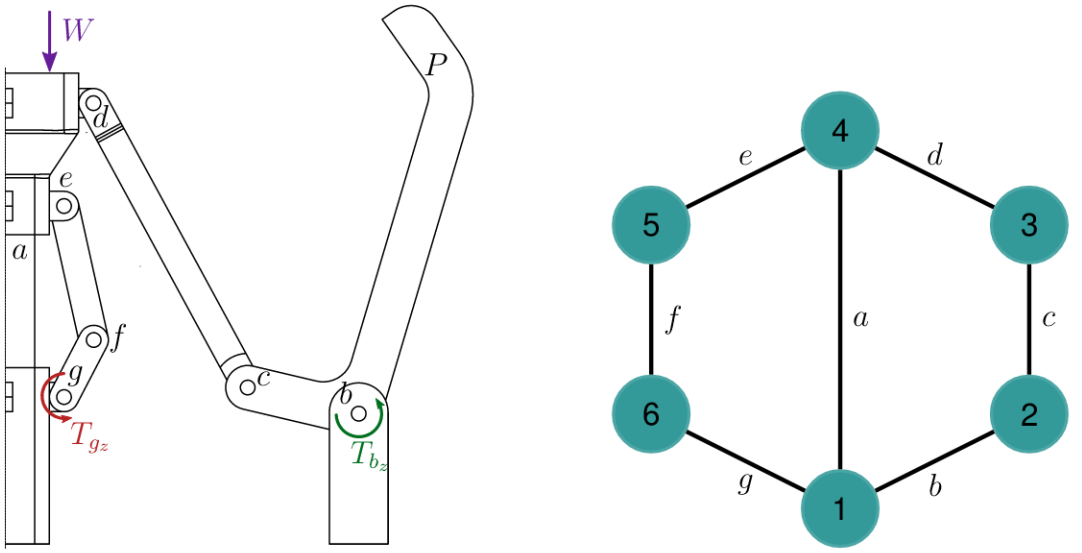

(a) Open mechanism.

(b) Closed mechanism graph representation.

Source: Own author.

arbitrarily chosen as chords, while the other five black edges were defined as branches. The blue line represents the external force applied to the gripper.

The cutset matrix $\boldsymbol{Q}$ was assembled following Eq. 12, which resulted in a 5×17 matrix. Due to its size, the cutset matrix presented only in Appendix A. Through the position kinematic process, described in Section 4.3.1, the coordinates of every joint were determined. Hence, it is possible to build the wrench for each joint following Eq. 18, which results in Eq. 40, Eq. 41, and Eq. 42. It should be noted that the wrench representing the UAV's weight is considered in the positive direction of the y axis. W must be negative, since the force is applied downwards to accomplish the closing motion.

$$\$_a = \begin{bmatrix} -y_a & 1 \\ 1 & 0 \\ 0 & 0 \end{bmatrix} \begin{bmatrix} F_{a_x} \\ T_{a_z} \end{bmatrix}, \$_b = \begin{bmatrix} -y_b & x_b & 1 \\ 1 & 0 & 0 \\ 0 & 1 & 0 \end{bmatrix} \begin{bmatrix} F_{b_x} \\ F_{b_y} \\ T_{b_z} \end{bmatrix}, \$_c = \begin{bmatrix} -y_c & x_c \\ 1 & 0 \\ 0 & 1 \end{bmatrix} \begin{bmatrix} F_{c_x} \\ F_{c_y} \end{bmatrix} \tag{40}$$

$$\$_d = \begin{bmatrix} -y_d & x_d \\ 1 & 0 \\ 0 & 1 \end{bmatrix} \begin{bmatrix} F_{d_x} \\ F_{d_y} \end{bmatrix}, \$_e = \begin{bmatrix} -y_e & x_e \\ 1 & 0 \\ 0 & 1 \end{bmatrix} \begin{bmatrix} F_{e_x} \\ F_{e_y} \end{bmatrix}, \$_f = \begin{bmatrix} -y_f & x_f \\ 1 & 0 \\ 0 & 1 \end{bmatrix} \begin{bmatrix} F_{f_x} \\ F_{f_y} \end{bmatrix} \tag{41}$$

$$\$_g = \begin{bmatrix} -y_g & x_g & 1 \\ 1 & 0 & 0 \\ 0 & 1 & 0 \end{bmatrix} \begin{bmatrix} F_{g_x} \\ F_{g_y} \\ T_{g_z} \end{bmatrix}, \$_W = \begin{bmatrix} x_W \\ 0 \\ 1 \end{bmatrix} \begin{bmatrix} W \end{bmatrix} \tag{42}$$

Figure 34 – Gripper's graph representation with every cut.

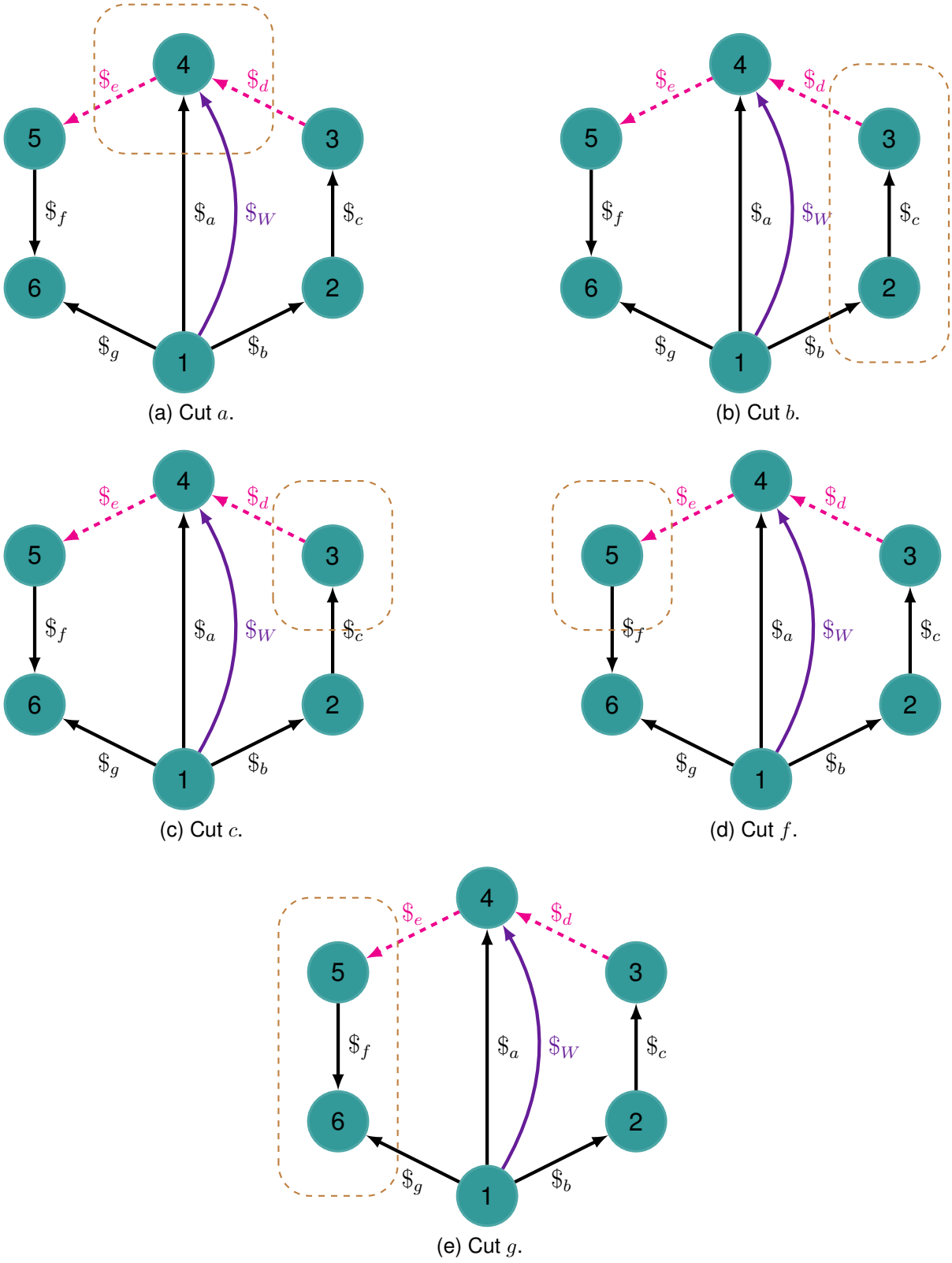

(a) Cut a.

(b) Cut b.

(c) Cut c.

(d) Cut f.

(e) Cut g.

Source: Own author.

The wrenches can be bound together in the unit action matrix $\boldsymbol{A_D}$, as exposed by Eq. 19. Similarly, the wrenches magnitudes are grouped in the action magnitude

vector, exposed by Eq. 20. This process results in Eq. 43 and 44.

$$\boldsymbol{A_D} = \begin{bmatrix} \$_{\boldsymbol{d}} & \$_{\boldsymbol{e}} & \$_{\boldsymbol{a}} & \$_{\boldsymbol{b}} & \$_{\boldsymbol{c}} & \$_{\boldsymbol{f}} & \$_{\boldsymbol{g}} & \$_{\boldsymbol{W}} \end{bmatrix} \tag{43}$$

$$\begin{aligned} \boldsymbol{\Psi} = [F_{d_x} \quad F_{d_y} \quad F_{e_x} \quad F_{e_y} \quad F_{a_x} \quad T_{a_z} \quad F_{b_x} \quad F_{b_y} \quad T_{b_z} \quad ... \\ ... \quad F_{c_x} \quad F_{c_y} \quad F_{f_x} \quad F_{f_y} \quad F_{g_x} \quad F_{g_y} \quad T_{g_z} \quad W_{drone}]^T \end{aligned} \tag{44}$$

The assembly of the network action matrix $\boldsymbol{A_N}$ was performed through Eq. 23, and resulted in a 15×17 matrix, presented in Appendix A. In order to solve this system of equations, matrix $\boldsymbol{A_N}$ must be square, and therefore it requires two primary variables. The first primary variable is the external force (the UAV's weight W), obtained from the drone's specification sheet.

As mentioned in Section 4.1, one primary function of the torsion spring in joint g is to soften the closing motion. Hence, it is expected that, as the gripper closes, the torque generated in joint b gets closer to zero. In order to determine the spring constant, the static analysis may consider a reasonably wide range of torques applied in g, so the resulting torque in b can be evaluated. Therefore, T_{g_z} is also considered as a primary variable in this case.

The torsion spring torque was evaluated in a range from zero to $30Nmm$, discretized in small displacements of $1Nmm$. The prismatic joint a displacement was discretized in forty points. For each position of a, the static analysis was performed for the entire range of T_{g_z}. The behavior of the generated torque in b, based on the torque in g as the gripper closes, can be evaluated in Fig. 35.

It can be seen from Fig. 35 that for a fully closed state, i.e. when $y_a = 110mm$, T_{b_z} is zero when $T_{g_z} = 20Nmm$. The constant of the torsion spring k_g can be calculated by Eq. 45. The angles θ_i and θ_f, presented by Fig. 30, can be determined using the results of the position kinematics.

$$k_g = \frac{T_{g_z}^{max}}{\theta_f - \theta_i} \tag{45}$$

Once the value of k_g has been determined, it is possible to perform the static analysis again. This time, however, the value of T_{g_z} can be calculated for each position. Figure 36 presents the same surface plot of Fig. 35, with the resulting output of T_{b_z} considering the value of k_g highlighted in black.

4.4.2 Aerial transport

Figure 37 presents the gripper in its closed state. The yellow circle concentric to joint f represents the solenoid that keeps the mechanism from moving. In order to simplify to process, it is considered that the UAV is hovering while carrying the load.

Figure 35 – Behavior of T_{b_z} in function of T_{g_z} and y_a.

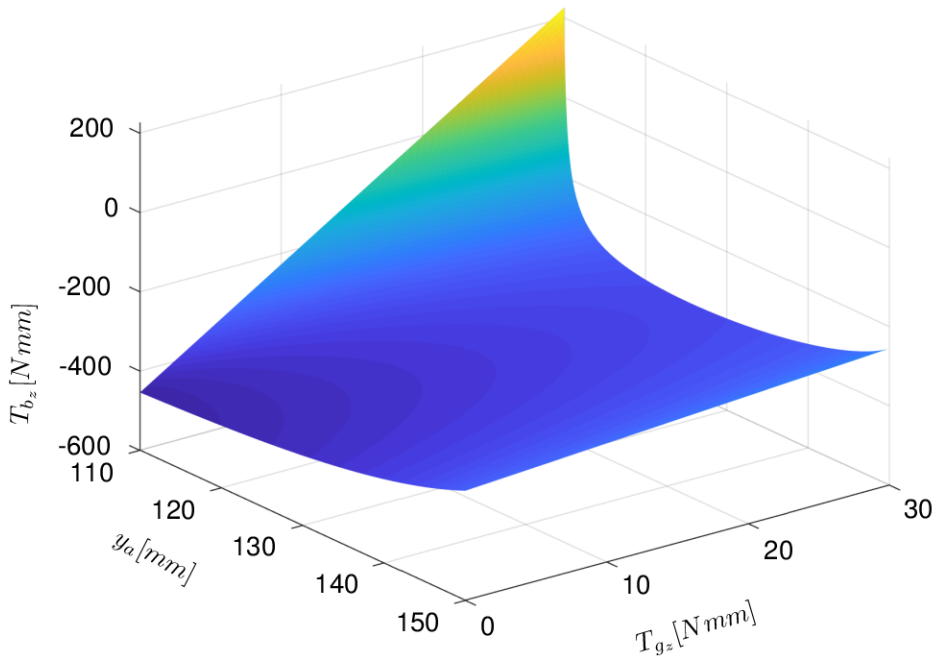

Figure 36 – Behavior of T_{b_z} considering the value of k_g.

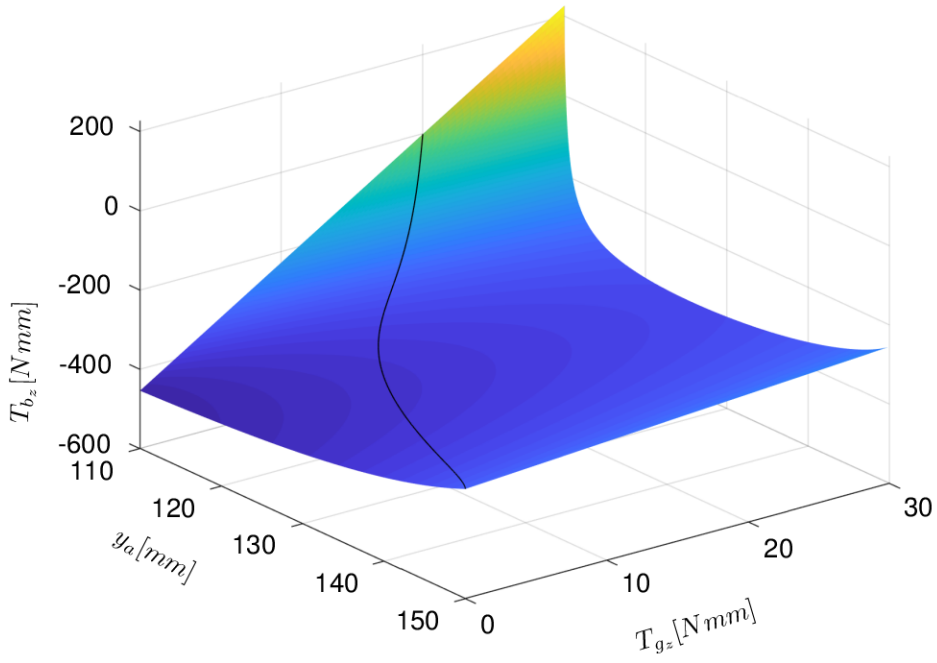

Therefore, the effort supported by the coupler's shaft, represented as F_{load} in Fig. 37 is equal to the load intensity and is distributed evenly to the fingers.

Since this analysis aims to evaluate the maximum loads imposed on the links, the load will be considered the UAV's maximum takeoff weight. The DJI Spreading Wings S900 specifications sheet states that the maximum takeoff weight is $8.2kg$. The value of

Figure 37 – Gripper's load representation for aerial transport.

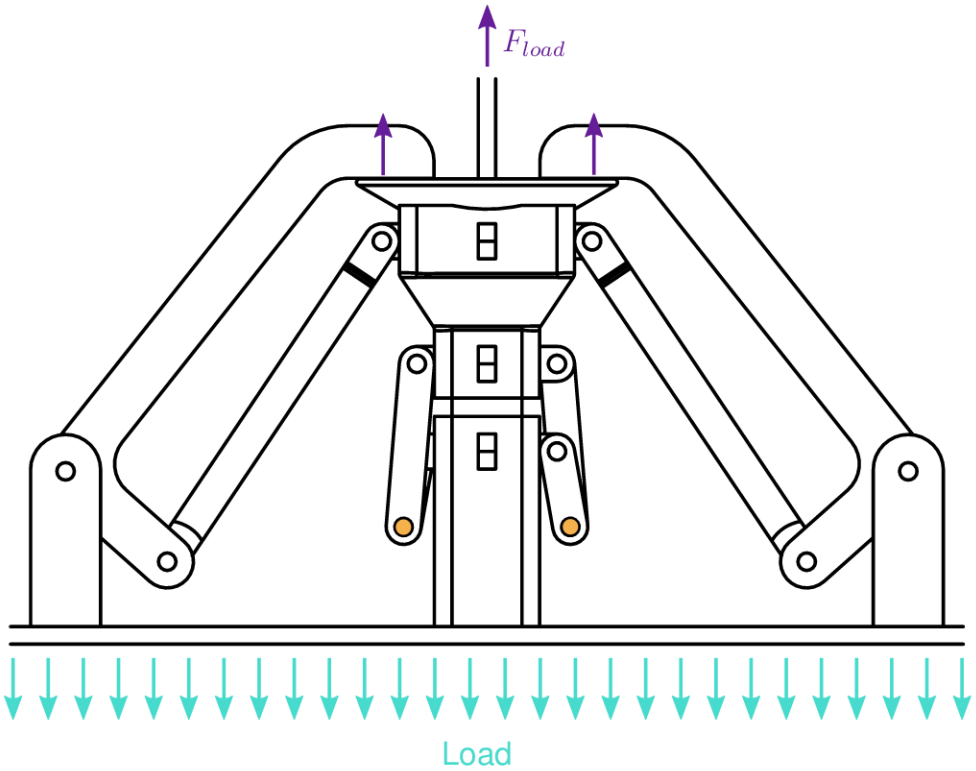

Source: Own author.

F_{load} can be obtained through Newton's second law, which results in $F_{load} = 80.442N$.

Following the same methodology implemented for the dimensional optimization and static analysis for the closing motion, this analysis is performed considering a single finger. It is also considered that the intensity of F_{load} is evenly distributed to all fingers.

Figure 38a presents the topology adopted for this analysis. Instead of considering the carried load, this model considers the force F_{EL}, equivalent to $\frac{1}{4}F_{load}$. Since the solenoid connects joint f to the fixed link, a new loop is created, as presented in Fig. 38b.

Analyzing Fig. 38, it can be seen that the torsion spring torque pushes the mechanism to an open position, generating an upward force in f through link 6. The solenoid compensates for this upward force, locking the mechanism in place. Therefore, it can be concluded that the force produced in f by the torsion spring does not contribute to the load in link 5 due to the solenoid absorbing it entirely. A similar effect occurs with link 5. The force F_{EL} produces an upward force in f through link 5, which is also absorbed by the solenoid. As a result, the force F_{EL} does not contribute to the load on link 6 due to the solenoid. As a result, the static analysis for the aerial transport scenario can be performed without considering link 6. However, the load acting on link 6 can be determined separately through a single-body diagram. Figure 39 presents the resulting graphs with the respective chords, branches, external loads, and cuts.

From Fig. 39, it is possible to create the cutset matrix $\boldsymbol{Q}$ following the procedure

Figure 38 – Evaluated configuration for aerial transport.

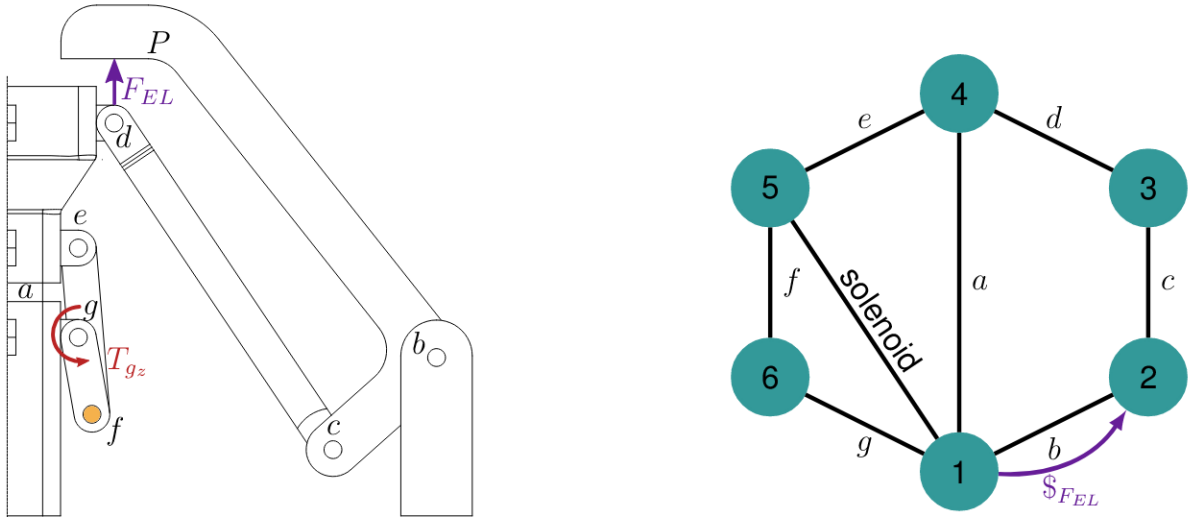

(a) Closed mechanism.

(b) Closed mechanism graph representation.

Source: Own author.

described in Section 3.4.2, which resulted in a 4×13 matrix, presented in Appendix B. The wrenches resulted in Eq. 46, Eq. 47, and Eq. 48.

$$\$_a = \begin{bmatrix} -y_a & 1 \\ 1 & 0 \\ 0 & 0 \end{bmatrix} \begin{bmatrix} F_{a_x} \\ T_{a_z} \end{bmatrix}, \$_b = \begin{bmatrix} -y_b & x_b \\ 1 & 0 \\ 0 & 1 \end{bmatrix} \begin{bmatrix} F_{b_x} \\ F_{b_y} \end{bmatrix}, \$_c = \begin{bmatrix} -y_c & x_c \\ 1 & 0 \\ 0 & 1 \end{bmatrix} \begin{bmatrix} F_{c_x} \\ F_{c_y} \end{bmatrix}, \tag{46}$$

$$\$_d = \begin{bmatrix} -y_d & x_d \\ 1 & 0 \\ 0 & 1 \end{bmatrix} \begin{bmatrix} F_{d_x} \\ F_{d_y} \end{bmatrix}, \$_e = \begin{bmatrix} -y_e & x_e \\ 1 & 0 \\ 0 & 1 \end{bmatrix} \begin{bmatrix} F_{e_x} \\ F_{e_y} \end{bmatrix}, \$_{sol} = \begin{bmatrix} -y_{sol} & x_{sol} \\ 1 & 0 \\ 0 & 1 \end{bmatrix} \begin{bmatrix} F_{sol_x} \\ F_{sol_y} \end{bmatrix}, \tag{47}$$

$$\$_{F_{EL}} = \begin{bmatrix} x_{F_{EL}} \\ 0 \\ 1 \end{bmatrix} \begin{bmatrix} W \end{bmatrix} \tag{48}$$

The unit action matrix $\boldsymbol{A_D}$ is assembled following the order of Eq. 49, and the action magnitude vector $\boldsymbol{\Psi}$ is assembled according to Eq. 50. The network action matrix $\boldsymbol{A_N}$ was assembled through Eq. 23 and resulted in a 12×13 matrix, presented in Appendix B. F_{EL} is a primary variable, which leads to the conclusion that the system of equations is well defined.

$$\boldsymbol{A_D} = \begin{bmatrix} \boldsymbol{\$_d} & \boldsymbol{\$_e} & \boldsymbol{\$_a} & \boldsymbol{\$_b} & \boldsymbol{\$_c} & \boldsymbol{\$_{sol}} & \boldsymbol{\$_{F_{EL}}} \end{bmatrix} \tag{49}$$

$$\begin{aligned} \boldsymbol{\Psi} = [F_{d_x} \quad F_{d_y} \quad F_{e_x} \quad F_{e_y} \quad F_{a_x} \quad T_{a_z} \quad F_{b_x} \quad F_{b_y} \quad \dots \\ \dots \quad F_{c_x} \quad F_{c_y} \quad F_{sol_x} \quad F_{sol_y} \quad F_{EL}]^T \end{aligned} \tag{50}$$

Figure 39 – Gripper's graph representation with every cut for aerial transport.

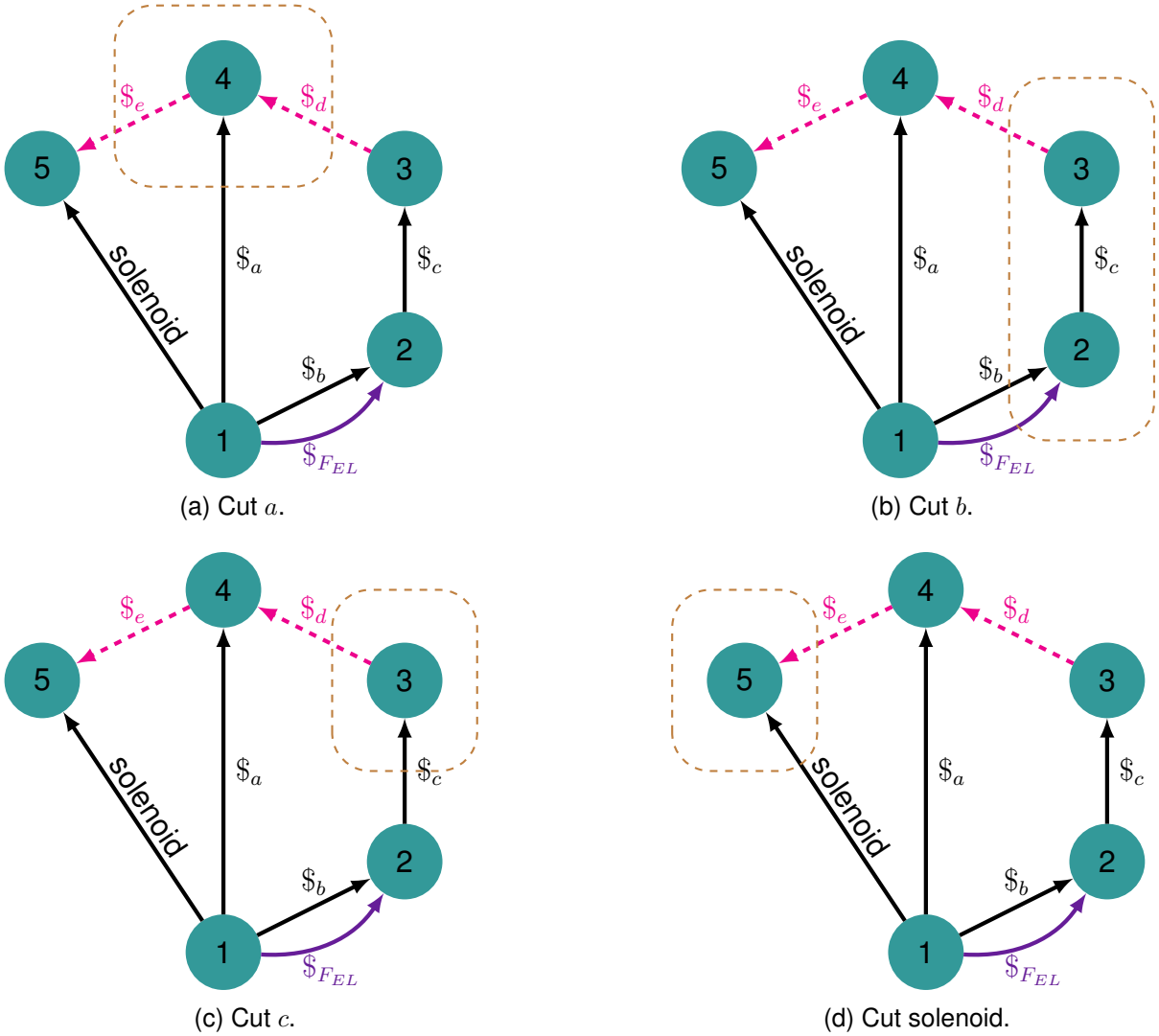

(a) Cut a. (b) Cut b.

(c) Cut c. (d) Cut solenoid.

Source: Own author.

Unlike the landing motion analysis, where the static analysis was performed for a set of discretized positions, the statics of the mechanism for aerial transport is performed only for the closed position. Table 4 presents the results of the static analysis for aerial transport and the maximum intensities obtained in Section 4.4.1.

4.5 CHAPTER OVERVIEW

This chapter presented the development of the coupling device. First, Section 4.1 presented the required and desired characteristics of the final mechanism. Next, Section 4.2 described how the kinematic chain was selected and how the kinematic pairs were defined to achieve the new topology. Section 4.3 developed a mathematical model that represents the new mechanism. This mathematical model was used to optimize the links' dimensions through an evolutionary algorithm process. Finally, the

Table 4 – Static analysis results for aerial transport and maximum values for landing motion.

joints:	a	b	c	d	e	f	g
Landing motion							
$\boldsymbol{F_x}$ $[N]$	5.91	5.49	5.49	5.49	0.80	0.80	0.80
$\boldsymbol{F_y}$ $[N]$	-	9.81	9.81	9.81	9.80	9.80	9.80
$\boldsymbol{T_z}$ $[Nmm]$	-98.10	-416.60	-	-	-	-	20.00
Aerial transport							
$\boldsymbol{F_x}$ $[N]$	-25.64	29.19	29.19	29.19	3.55	-3.55	-
$\boldsymbol{F_y}$ $[N]$	-	-23.46	-43.57	-43.57	-43.57	43.57	-
$\boldsymbol{T_z}$ $[Nmm]$	560.17	-	-	-	-	-	-

Source: Own author.

optimization results were used to perform the static analysis through Davies method on Section 4.4.

5 THICKNESS AND WEIGHT ESTIMATE

Since the developed gripper may be used for aerial transport of packages, the structure of the mechanism must handle the load without failing. Therefore, this chapter deals with the structural analysis of the gripper's components. At first, Section 5.1 presents a few of the most common materials used in UAVs and aircraft in general. Section 5.2 describes the method adopted to evaluate the structural integrity of the mechanism's components and to estimate each member's cross-section area. Once the material is known and the cross-section area is determined, it is possible to estimate the weight of each component. Section 5.3 describes the static analysis procedure considering the weight of each link and compares the results with the analysis performed in Chapter 4. Finally, Section 5.4 presents some final considerations.

5.1 MATERIAL SELECTION

The results presented in Table 4 may be used to estimate the minimum thickness of the links, so there is no risk of failure during operation. Additionally, the weight of each link may be determined, so the dimension of the torsion spring can be verified, i. e., the torsion spring defined in Section 4.4.1 is capable of returning the mechanism to its initial state. Both dimensions rely on material characteristics and cross-section dimensions. Even though this section deals with the definition of an estimate to the cross-section dimension and weight for each link, it does not dismiss the necessity of structural optimization.

All aircraft must be lightweight. The lighter the structure, the more efficient the system is, the more extensive range it can cover, the greater payload it can carry (NIU; NIU, 1988). The same applies to the gripper mechanism. The material selection for the mechanism's components must consider the stiffness-to-weight ratio.

Some inspiration to which materials to adopt might be obtained from the most common ones used in existing UAV frames. The frame gives a drone its shape and holds all the subsystems in place. Since it serves a mechanical function, strength is the essential property. Commercial drones are usually built with thermoplastics, such as variants of nylon, polyester, and polystyrene (SADRAEY, 2017). These options are popular because of their low manufacturing cost, good strength, and low density. Many thermoplastics are commercially available in filaments, allowing manufacturing through 3D printing.

There are very few reports of aluminum frames for UAVs, but adopting an aluminum alloy may be acceptable since it plays a vital role in aircraft construction. It has been the preferred choice of metal materials for aerospace applications due to its lightweight properties, high strength-to-weight ratio, and good formability, which eases the fabrication process.

High-end industrial UAVs prioritize performance. In this case, the frames are generally made of carbon fiber-reinforced composites. Carbon fiber is a polymer made of carbon atoms bound together with crystals during manufacturing. The fibers are woven into pliable sheets and are shaped into the design using a mold. Carbon fiber can be ten times stronger than steel, twice as stiff, and four times lighter.

This work considers the manufacturing of the gripper using three materials:

- **ABS**: it is a common thermoplastic polymer that provides a good balance of mechanical properties, outstanding surface finishing capability, good impact resistance, and superior processibility at a low cost (CAMPO, n.d.).
- **6061-T6 aluminum alloy**: it is widely employed in the aerospace industry for offering high mechanical strength at a relatively low density and corrosion resistance (YANG; LI; LI, 2014). It has good mechanical properties, is easily workable, and is often used on landing mats for aircraft, frames, and structural components.
- **XC110 Twill 3k prepeg carbon fiber**: according to the manufacturer, this carbon fiber is recommended for both structural and cosmetic applications. This material has been applied in several projects, such as high-performance drones, professional bike frames, and other high-precision parts.

Table 5 presents the relevant mechanical properties of the materials adopted. It can be seen that ABS is much weaker than the aluminum alloy and carbon fiber. However, since an ABS prototype is much easier to manufacture and less costly than the other options, it is worth considering it in the analysis.

Table 5 – Mechanical properties of the selected materials.

Property	**Symbol**	**ABS**	**AL 6061-T6**	**XC110 Carbon Fiber**
density	$\rho\ [\frac{kg}{m^3}]$	1020.0	2700.0	840
Yield Strength	$\sigma_{yield}\ [MPa]$	34.5	275.0	521
Young's Modulus	$E\ [MPa]$	2000.0	69000.0	55100.0
Shear Modulus	$G\ [MPa]$	318.9	25940	-

Source: Own author.

5.2 STRUCTURAL ANALYSIS

The external forces applied to the mechanism, whether during the closing motion or aerial transport, are transmitted from one point of the rigid body to another. This transmission of force can be envisioned as a flow or force distribution that can be further analyzed by inspecting internal surfaces, also known as cross-section areas,

within the body. To properly dimension the cross-section area of each link, it is essential to determine the maximum shear and moment acting in each element.

The goal of this structural analysis is only to estimate the thickness of each link. Therefore, all cross-sections are considered to have a rectangular shape. Table 4 shows that the forces acting on the joints are much higher when performing aerial transport. Hence, these forces are considered for dimensioning the cross-section area.

To ensure the structural safety of a mechanical member, the applied load must be less than the maximum load the member can support. This restriction is advised for many reasons, mainly to compensate for possible errors in manufacturing or variability in the materials' mechanical properties. A commonly used method of specifying the allowable load for a mechanical member is the **factor of safety**, defined by Eq. 51. Regulatory bodies demand a minimum safety of factor of 1.5 (ZIPAY; MODLIN; LARSEN, 2016), while the USAR 3.0, a first European regulation for unmanned air systems, requires a factor of safety of 1.3 (NEUBAUER; GÜNTHER; FÜLLHAS, 2007). Therefore, this work adopts a safety of factor of 1.5 as the minimum.

$$\eta = \frac{\sigma_{yield}}{\sigma_{allowed}} \tag{51}$$

Figure 40 – Force, Shear and Moment diagrams for link 2.

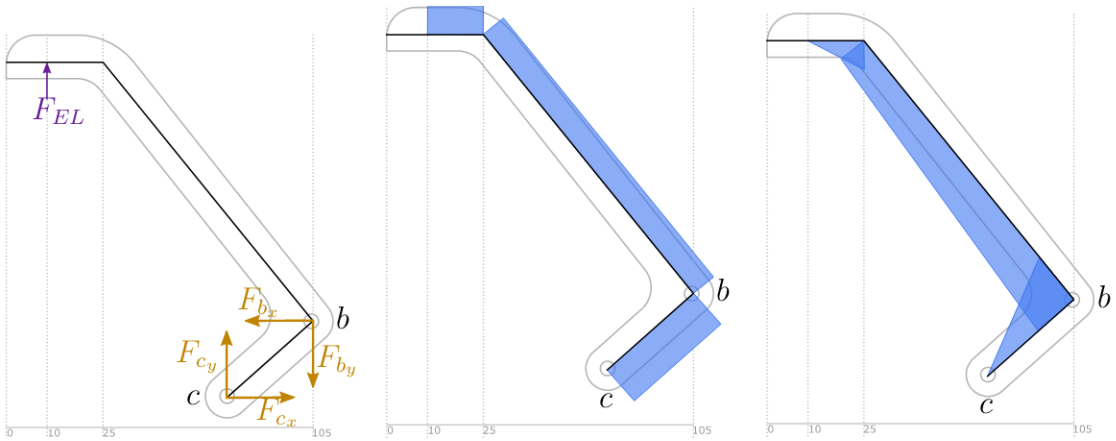

(a) Force diagram. (b) Shear diagram. (c) Momentum diagram.

Source: Own author.

Figure 40a presents the force diagram for link 2. The distributed load F_{EL} represents the force transmission from the UAV's coupler to the finger. Figure 40b presents the resulting shear diagram, while Fig. 40c presents the resulting moment diagram for link 2. It can be seen that the maximum load occur around joint b. Although there are effects from axial stress, it is negligible and will not be considered in this case. The same occurs on link 6, where The maximum load occur on joint g, as presented by Fig. 41. Therefore, the total stress on joints b and g can be calculated through Eq. 52.

Figure 41 – Force, Shear and Moment diagrams for link 6.

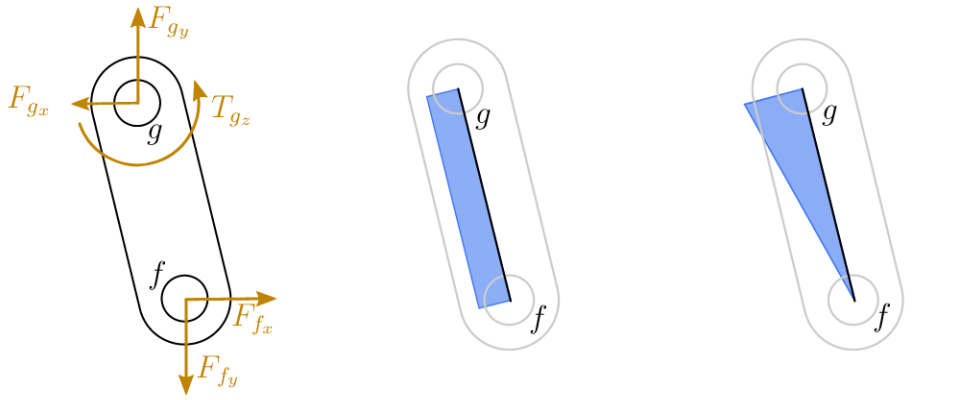

(a) Force diagram. (b) Shear diagram. (c) Momentum diagram.

Source: Own author.

$$\sigma = \sigma_{bending} + \sigma_{shear} = \frac{Mc}{I} + \frac{3V}{2A} \tag{52}$$

Even though the factor of safety reduces the chance of material failure, the material deflection must also be analyzed to guarantee that the mechanism does not deflect to a point in which it is no longer operable. The deflection analysis is performed using Castigliano's theorem. This theorem states that "when forces act on elastic systems subject to small displacements, the displacement corresponding to any force, in the direction of the force, is equal to the partial derivative of the total strain energy with respect to that force" (BUDYNAS; NISBETT, et al., 2011). In mathematical terms, Castigliano's theorem is defined by Eq. 53, while the displacement δ due to axial, shear, and bending stresses may be computed directly through Eq. 54, 55 and 56, respectively.

$$\delta = \frac{\partial U}{\partial F_i} \tag{53}$$

$$\delta_{axial} = \frac{\partial U}{\partial F_i} = \int \frac{1}{AE}\left(F\frac{\partial F}{\partial F_i}\right) dx \tag{54}$$

$$\delta_{shear} = \frac{\partial U}{\partial F_i} = \int \frac{cF}{AG}\, dx \tag{55}$$

$$\delta_{bending} = \frac{\partial U}{\partial F_i} = \int \frac{1}{EI}\left(M\frac{\partial M}{\partial F_i}\right) dx \tag{56}$$

For link 2, a potentially problematic displacement is in the y-axis, at the finger's tip. If the displacement is large enough, it may cause unwanted detachment. Figure 42a presents the parameters adopted for applying Castigliano's theorem. The imaginary force F_i is related to Castigliano's theorem. More information about it and how it influences the displacement analysis may be obtained from Budynas, Nisbett, et al. (2011).

It can be concluded that two equations define the shear stress, one considering only the effect of the imaginary force F_i, and a second one considering the effect of both F_i and F_{EL}. Equation 57 describes the shear displacement considering both behaviors. Similarly, there are two moment equations. Equation 58 describes the bending displacement, and finally, the total displacement for link 2 in the y-axis may be computed by Eq. 59.

Figure 42 – Adopted parameters for Castigliano's theorem.

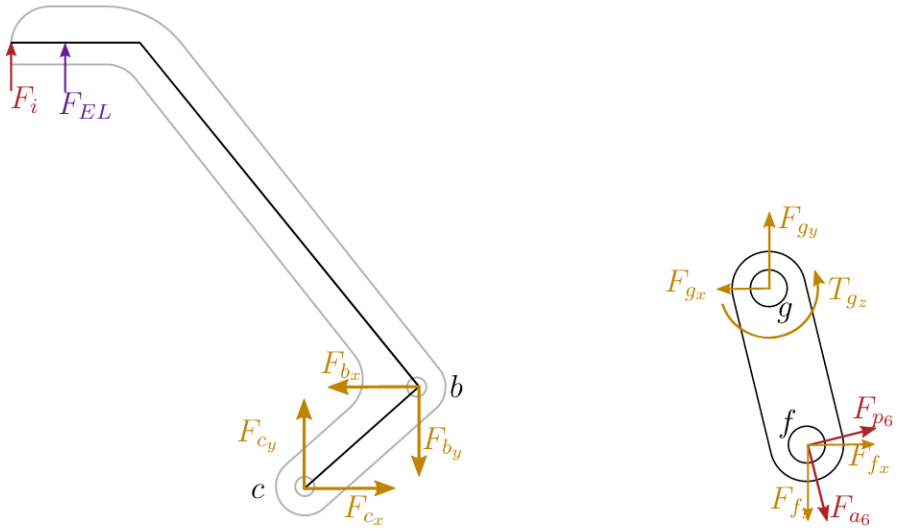

(a) Castigliano force diagram for link 2.

(b) Castigliano force diagram for link 6.

Source: Own author.

$$\delta_{Link2_{shear}} = \int_{10}^{25} \frac{c}{AG} F_{EL}\, dx + \int_{25}^{105} \frac{c}{AG} \frac{F_{EL}}{sin(90-\alpha)}\, dx \tag{57}$$

$$\begin{aligned} \delta_{Link2_{bending}} = &\int_{0}^{10} \frac{1}{EI} \left(F_i x \frac{\partial F_i x}{\partial F_i} \right) dx + ... \\ &+ \int_{20}^{105} \frac{1}{EI} \left((F_i x + F_{EL} x) \frac{\partial (F_i x + F_{EL} x)}{\partial F_i} \right) dx \end{aligned} \tag{58}$$

$$\delta_{Link2} = \delta_{Link2_{shear}} + \delta_{Link2_{bending}} \tag{59}$$

According to Budynas, Nisbett, et al. (2011), the contribution of transverse shear to the deflection decreases as the length-to-height ratio increases, and it may be considered negligible for thin bodies, i.e., when the length-to-height ratio is higher than 10. However, the deflection analysis considers the transverse shear, since the cross-section area is still unknown.

It has been defined how to determine the expected displacement for the links of the mechanism. However, the displacement limit, i.e., how much deformation is

acceptable for each link so it can still be considered operable is undetermined. The definition of this limit is only possible after a thorough analysis of the risks involved, such as unwanted detaching. Since this section's objective is to estimate the dimensions of the cross-section areas, a deflection of up to 1% of the link's length is considered acceptable.

Figure 43 – Force diagrams for links 3 and 5.

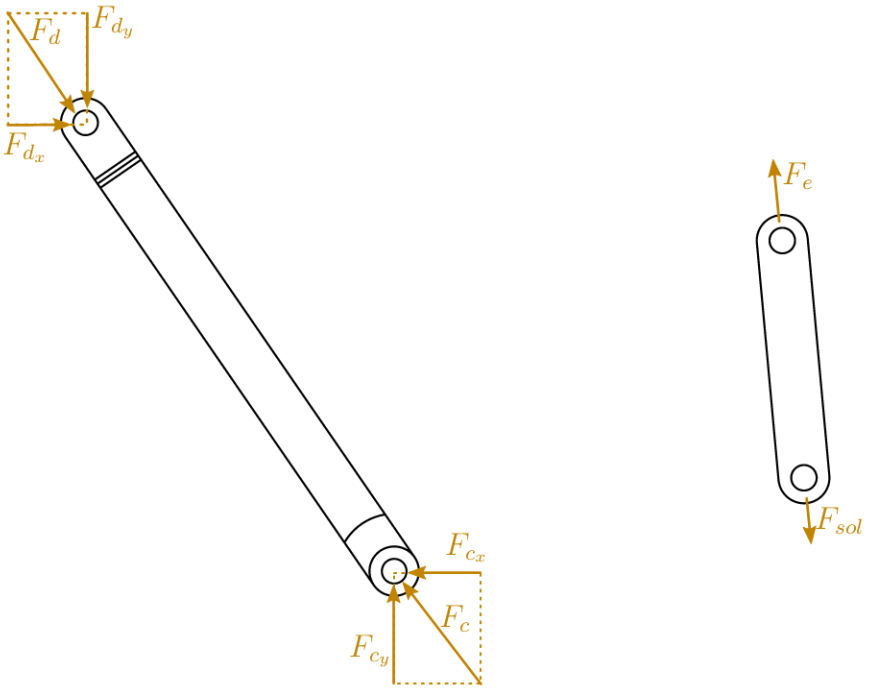

(a) Link 3 force diagram. (b) Link 5 force diagram.

Source: Own author.

Figures 43a and 43b present the reaction forces acting on links 3 and 5, respectively. It can be seen that both links are two-force members, i.e., there are only two collinear forces acting on each link, with opposite directions. Hence, these links are only subject to axial stress, given by Eq. 60.

$$\sigma_{axial} = \frac{F}{A} \tag{60}$$

As discussed for link 2, links 3 and 5 are also subject to deflection, which may also be determined using Castigliano's theorem. Since they are only under axial stress, the deflection can be determined using Eq. 54. From Fig. 43a and Fig. 43b, it can be seen that links 3 is under compression and 5 is under tension. The state of compression may cause a lateral deflection called *buckling*. According to Hibbeler (2017), buckling can lead to a sudden failure. The critical axial load a two-force member can support without buckling may be calculated by Eq. 61. Rearranging Eq. 61, it is possible to determine the minimum value for the moment of inertia I. Considering a factor of safety of 1.5, the relation $F_c r = 1.5 F_{axial}$ may be implemented directly in Eq. 62.

$$F_{cr} = \frac{\pi^2 EI}{L^2} \tag{61}$$

$$I = \frac{1.5 F_{axial} L^2}{\pi^2 E} \tag{62}$$

Similar to link 2, link 6 is also subject to bending and shear stresses. First, the reaction forces in joint f were decomposed in an axial force (F_{a_6}) and a perpendicular force to link 6 (F_{p_6}), as presented by Fig. 42b. Afterwards, to compute the deflection follows the same procedure used on link 2. Equations 63 and 64 are used to calculate the deflection due to shear and bending stresses, respectively.

$$\delta_{Link6_{shear}} = \int_0^{L_6} \frac{c}{AG} F_{p_6}\, dx \tag{63}$$

$$\delta_{Link6_{bending}} = \int_0^{L_6} \frac{1}{EI} \left(F_{p_6} x \frac{\partial F_{p_6} x}{\partial F_{p_6}} \right) dx \tag{64}$$

Determining the dimensions of the cross-section area is an iterative task. Equations 52 and 60 are solved using an initial guess for the cross-section dimensions, so it is possible to calculate the cross-section area (A) and moment of inertia (I). The resulting stress is evaluated considering the factor of safety, and the dimensions are adjusted accordingly. Additionally, the deflections are calculated and evaluated if they fit the determined criteria. This process resulted in the dimensions presented in Fig. 44. Table 6 presents the stresses and deflections calculated for each link. It can be seen that, although the factor of safety η is much higher than the minimum value, the deflection that occurs on link 2 is very close to the designated limit.

Table 6 – Stress and deflections calculated for all links with ABS.

	L_2	L_3	L_5	L_6
$\sigma_{axial}[MPa]$	-	2.0978	2.9143	-
$\sigma_{shear}[MPa]$	0.2784	-	-	0.0914
$\sigma_{bending}[MPa]$	2.9082	-	-	1.6000
$\sigma_{total}[MPa]$	3.1865	2.0978	2.9143	1.6914
η	10.8268	16.4460	11.8382	20.3974
$\delta_{axial}[mm]$	-	0.1155	0.0680	-
$\delta_{shear}[mm]$	0.0386	-	-	0.0050
$\delta_{bending}[mm]$	0.8477	-	-	0.0510
$\delta_{total}[mm]$	0.8862	0.1155	0.0680	0.0561
$\Delta\delta[\%]$	1.059	0.010	0.145	0.256

Source: Own author.

Figure 44 – Cross-section dimensions considering the ABS mechanical properties.

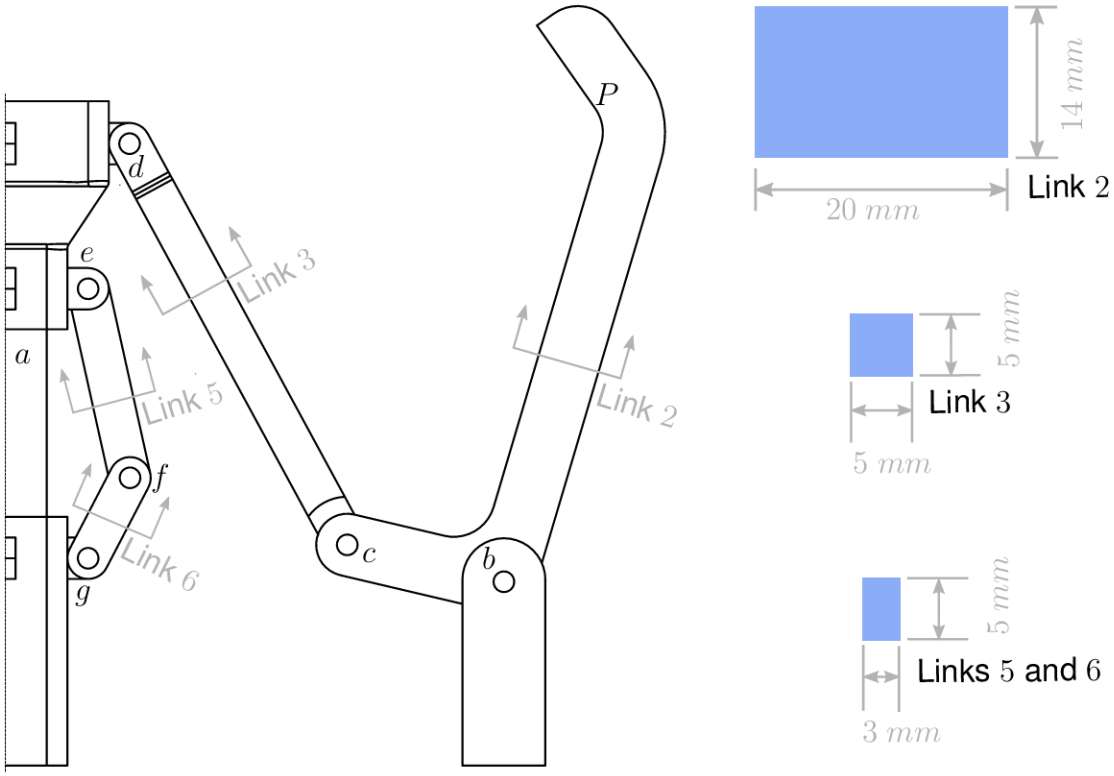

Source: Own author.

As presented in Table 5, the aluminum alloy and carbon fiber are much stronger than the ABS. Hence, hollow shafts will be used instead of a solid cross-section to reduce weight, and the thickness t for each material is dimensioned accordingly. Figure 45 presents the resulting cross-sections for each link considering the aluminum alloy mechanical properties.

Table 7 presents the stress and deflection calculated considering aluminum components. Compared to the results of table 6, the stress is much higher due to the differences in the cross-section areas. The deflections are also much smaller, which was expected due to the huge difference in the materials Elastic Modulus.

Figure 46 presents the cross-sections determined considering carbon-fiber properties. Compared to the dimensions for aluminum, in Fig. 45, it can be seen that they are very similar. The results for stresses and deflections, presented in table 8 are also very similar due to the similarity of the cross-section areas. The major differences are the resulting deflections, which the smaller Elastic Modulus can explain.

5.3 STATIC ANALYSIS CONSIDERING THE LINKS' WEIGHT

The resulting weight of the links that compose the mechanism may influence the results of the first static analysis. Therefore, two additional analyses are conducted. The first analysis aims to determine if the torsion spring dimensioned in Section 4.4.1

Figure 45 – Cross-section dimensions considering Aluminum mechanical properties.

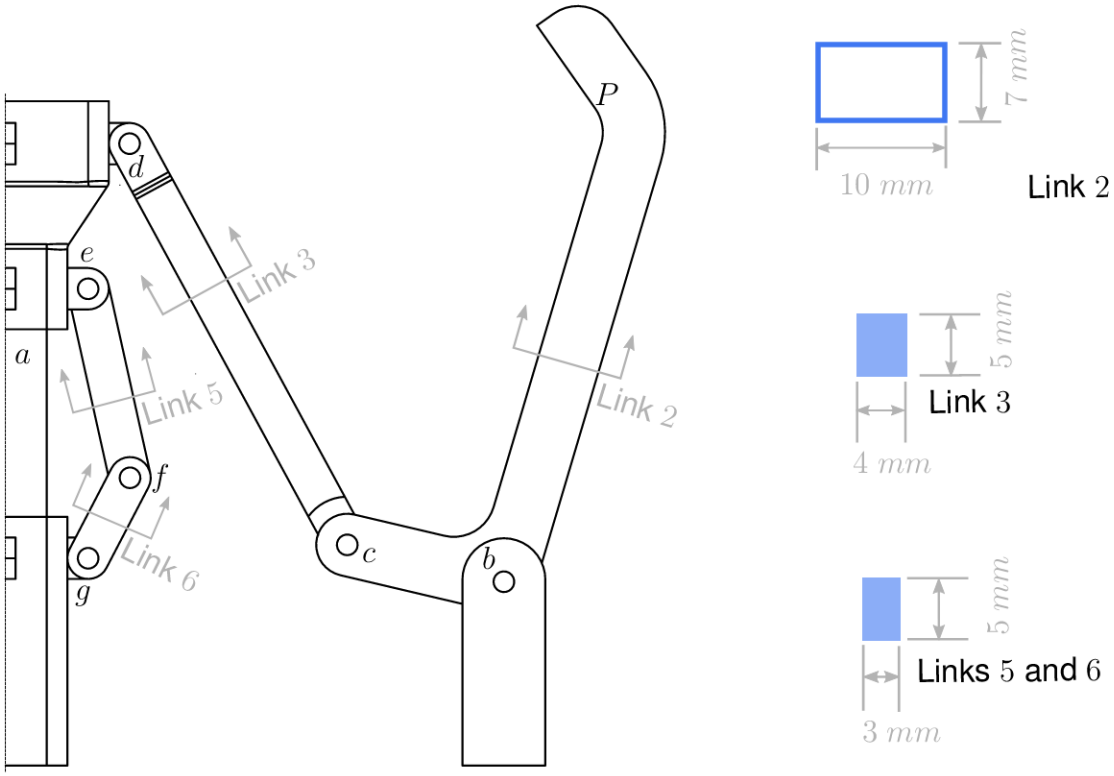

Source: Own author.

is enough to move the gripper to its original state. Therefore, the same model of the landing motion analysis is used, but considering $W = 0$, i.e., the UAV's weight does not contribute in this case, and T_{g_z} as an unknown variable. The gravitational effect of the mass of the components is modeled as external forces being applied on each

Table 7 – Stress and deflections calculated for all links with Aluminum.

	L_2	L_3	L_5	L_6
$\sigma_{axial}[MPa]$	-	2.6222	2.9143	-
$\sigma_{shear}[MPa]$	4.7237	-	-	0.0914
$\sigma_{bending}[MPa]$	48.9375	-	-	1.600
$\sigma_{total}[MPa]$	53.6612	2.6222	2.9143	1.6914
η	5.1247	104.8732	94.3625	162.5882
$\delta_{axial}[mm]$	-	0.0042	0.0020	-
$\delta_{shear}[mm]$	0.0080	-	-	6.16e-5
$\delta_{bending}[mm]$	0.7718	-	-	0.0015
$\delta_{total}[mm]$	0.7798	0.0042	0.0020	0.0015
$\Delta\delta[\%]$	0.931	0.003	0.004	0.006

Source: Own author.

Figure 46 – Cross-section dimensions considering Carbon Fiber mechanical properties.

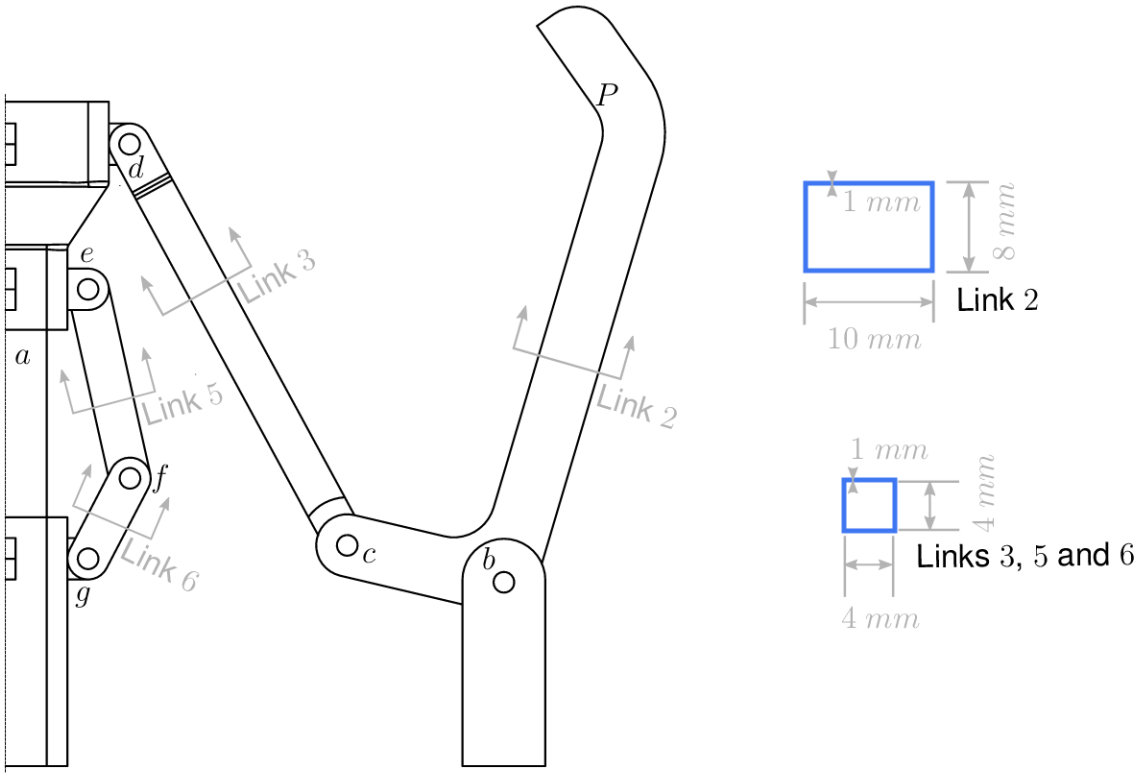

Source: Own author.

Table 8 – Stress and deflections calculated for all links with Carbon Fiber.

	L_2	L_3	L_5	L_6
$\sigma_{axial}[MPa]$	-	7.4920	6.2449	-
$\sigma_{shear}[MPa]$	4.5848	-	-	0.1958
$\sigma_{bending}[MPa]$	44.8598	-	-	2.7429
$\sigma_{total}[MPa]$	49.4446	7.4920	6.2449	2.9387
η	10.5371	69.5405	83.4279	177.2897
$\delta_{axial}[mm]$	-	0.0150	0.0053	-
$\delta_{bending}[mm]$	0.8306	-	-	0.0040
$\delta_{total}[mm]$	0.8306	0.0150	0.0053	0.0040
$\Delta\delta[\%]$	0.992	0.013	0.011	0.018

Source: Own author.

link's center of mass, as illustrated in Fig. 47. This way, it is possible to compare the spring's minimum requirement to the adopted one. The second analysis is the same static analysis performed in Section 4.4.1, considering the mass of the components and analyzing the difference of the results.

Figure 48 presents the gripper's graph representation, along with each cut, with

Table 9 – Weight of the grippers components for each material, measured in grams.

	ABS	**Al 6061-T65**	**XC 110 Carbon Fiber**
L_2	53.58	16.00	5.16
L_3	2.88	6.09	0.67
L_4	35.43	93.79	29.18
L_5	0.76	2.00	0.29
L_6	0.38	0.99	0.14

Source: Own author.

Figure 47 – Links' weight model applied in the static analysis.

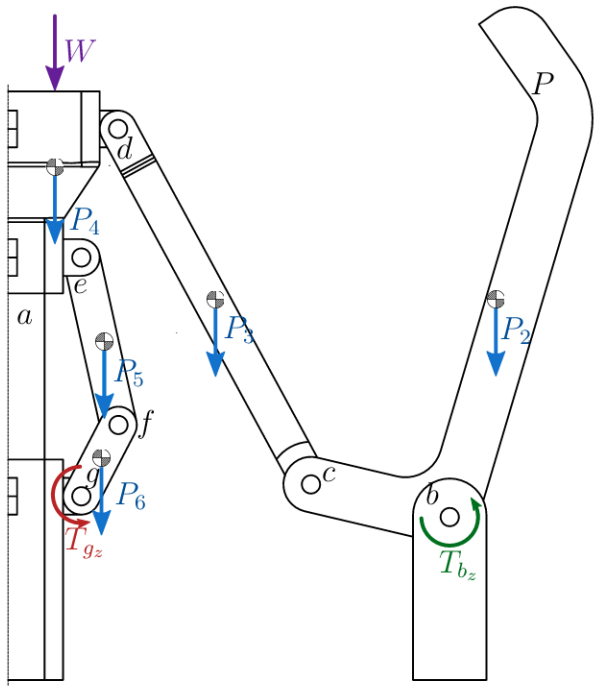

Source: Own author.

the weights of the links and the UAV's weight as external loads. The wrenches defined in Eq. 40, 41 and 42 are still valid. The wrenches presented by Eq. 65 and 66 must be added to unit action matrix A_D to include the links' weights effect. Hence, matrix A_D is extended to Eq. 67, and the action magnituve vector Ψ is extended to Eq. 68.

$$\$_{W_2} = \begin{bmatrix} x_{W_2} \\ 0 \\ 1 \end{bmatrix} \left[W_2\right], \$_{W_3} = \begin{bmatrix} x_{W_3} \\ 0 \\ 1 \end{bmatrix} \left[W_3\right], \$_{W_4} = \begin{bmatrix} x_{W_4} \\ 0 \\ 1 \end{bmatrix} \left[W_4\right] \tag{65}$$

$$\$_{W_5} = \begin{bmatrix} x_{W_5} \\ 0 \\ 1 \end{bmatrix} \left[W_5\right], \$_{W_6} = \begin{bmatrix} x_{W_6} \\ 0 \\ 1 \end{bmatrix} \left[W_6\right] \tag{66}$$

Figure 48 – Gripper's graph representation with every cut.

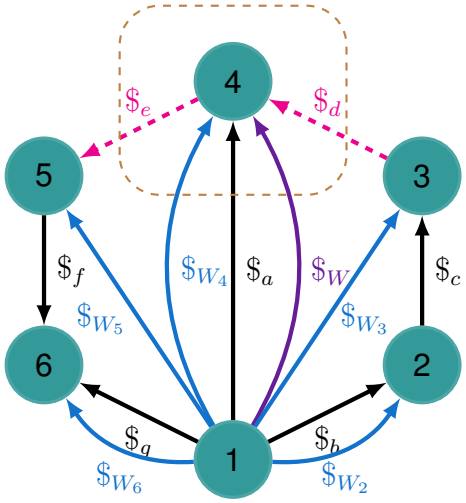

(a) Cut a.

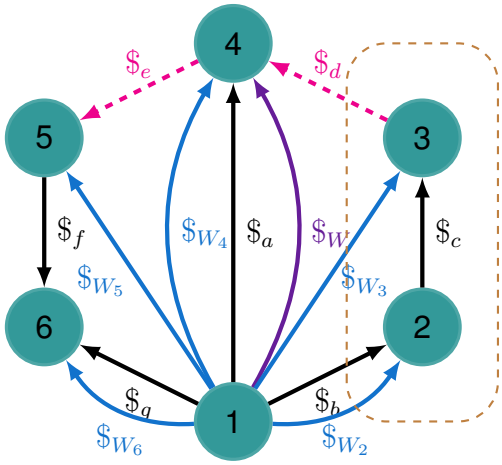

(b) Cut b.

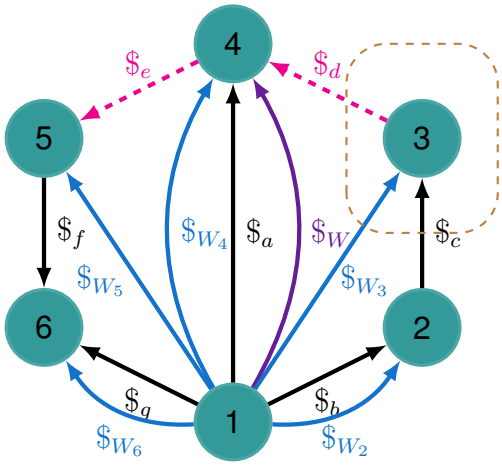

(c) Cut c.

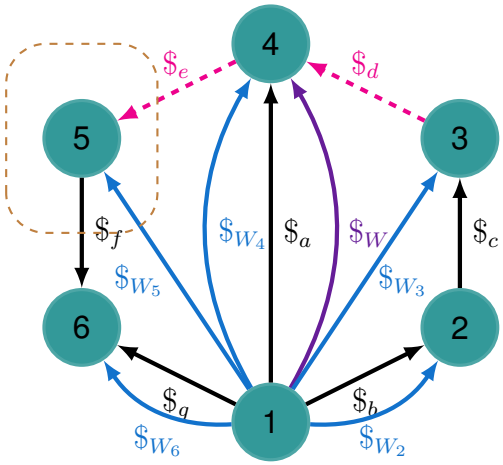

(d) Cut f.

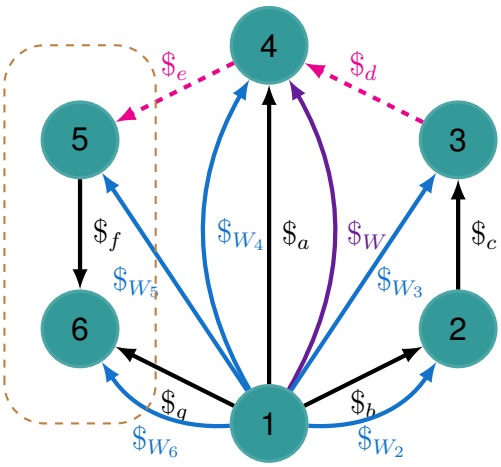

(e) Cut g.

Source: Own author.

$$\boldsymbol{A_D} = [\$_d \quad \$_e \quad \$_a \quad \$_b \quad \$_c \quad \$_f \quad \$_g \quad \$_W \quad \$_{W_2} \quad \dots \quad \dots \quad \$_{W_3} \quad \$_{W_4} \quad \$_{W_5} \quad \$_{W_6}] \tag{67}$$

$$\begin{aligned}\mathbf{\Psi} = [&F_{d_x} \quad F_{d_y} \quad F_{e_x} \quad F_{e_y} \quad F_{a_x} \quad T_{a_z} \quad F_{b_x} \quad F_{b_y} \quad T_{b_z} \quad ... \\ &... \quad F_{c_x} \quad F_{c_y} \quad F_{f_x} \quad F_{f_y} \quad F_{g_x} \quad F_{g_y} \quad T_{g_z} \quad W \quad ... \\ &... \quad W_2 \quad W_3 \quad W_4 \quad W_5 \quad W_6]^T\end{aligned} \tag{68}$$

The assembly of the network action matrix A_N followed the same procedure adopted in Section 4.4.1, and is presented in Appendix C. To evaluate the intensity of the torsion spring, the weight of the drone is set to zero ($W = 0$), and the torque in joint g is considered an unknown output.

Figure 49a presents the resulting torques for each material. It also presents the torque provided by the spring dimensioned in Section 4.4.1. It can be seen that the current spring is higher than the minimum torque obtained for the mechanism manufactured with Carbon Fiber. Considering the mechanism produced with ABS, there is a region in which the minimum torque is higher than the torque produced by the spring, and for aluminum, the required torque is much higher. Therefore, the previously designed spring is not suitable for ABS and aluminum. A possible solution for the mechanism manufactured with ABS is to apply a pretension to the spring, which results in the behavior presented in Fig. 49b. It should be noted that the parabolic behavior of the minimum torques presented in Fig. 49 is mainly due to the mass of link 4, which is considered a solid piece. A better dimensioning through a structural synthesis would probably decrease this body's weight and flatten the curve, as it occurs with Carbon Fiber.

The static analysis performed in Section 4.4.1 was repeated, considering the effect of the links' mass and a pre-tensioned torsion spring. In order to compare the effect of the weight of the links in the static analysis, Fig. 50, Fig. 51 and Fig. 52 present the reaction forces of each joint along the entire range of motion for the three materials considered, and without considering the mass of the links.

Table 10 presents the mean error of the reaction forces considering the effect of the links' weight of each material compared to the results of the analysis from Section 4.4.1. The comparison graphs of the static analysis results for each material shows that $F_{x_b} = F_{x_c} = F_{x_d}$, and $F_{x_e} = F_{x_f}$. Therefore, Table 10 includes only the results of F_{x_b} and F_{x_e}.

5.4 CHAPTER OVERVIEW

This chapter presented the structural analysis of the gripper's links. Section 5.1 presented a brief overview of the mechanical properties and features of ABS, Aluminum alloy, and carbon fiber and their applications in UAV and aircraft manufacturing. Section 5.2 performed a structural analysis of each link that composes the gripper. The internal stress was calculated considering the results obtained from the static analysis, and

Figure 49 – Minimum torques in joint g for the entire range of motion.

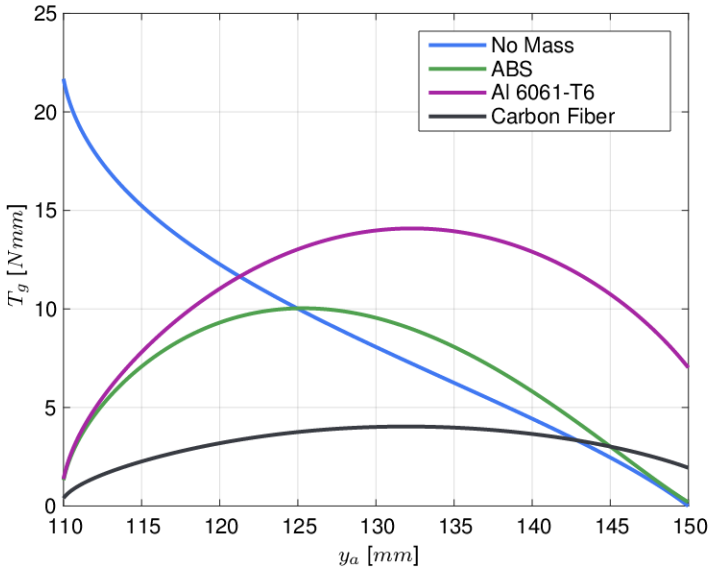

(a) Initial torsion spring behavior.

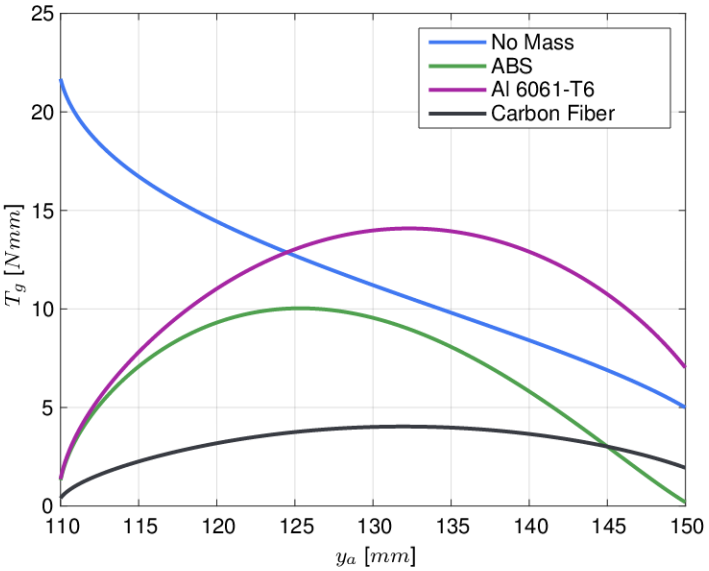

(b) Pre-loaded torsion spring behavior.

an estimate of the cross-section area was made considering a factor of safety. This estimate also considered the deflection of each link, determined through Castigliano's theorem. Finally, Section 5.3 described the static analysis considering the weight of each link, and the results were compared to the ones obtained in Chapter 4.

Table 10 – Mean error and standard deviation of the static analysis results.

	ABS		Al		CF	
	Mean error	**Std**	**Mean error**	**Std**	**Mean error**	**Std**
$\boldsymbol{F_{x_a}[N]}$	0.2085	0.0161	0.5475	0.0422	0.1656	0.0124
$\boldsymbol{T_a[N]}$	-6.1989	0.0380	-16.4057	0.0998	-5.0256	0.0143
$\boldsymbol{F_{x_b}[N]}$	-0.2109	0.0165	-0.5538	0.0432	-0.1665	0.0126
$\boldsymbol{F_{y_b}[N]}$	0.9109	0.0017	1.1616	0.0044	0.3470	6.36e-4
$\boldsymbol{T_b[Nmm]}$	-24.1485	9.0064	-44.4466	5.8105	-13.2086	1.7842
$\boldsymbol{F_{x_e}[N]}$	-0.0024	7.47e-4	-0.0063	0.0020	-9.09e-4	2.81e-4
$\boldsymbol{F_{y_e}[N]}$	0.0095	0.0017	0.0248	0.0044	0.0036	6.36e-4
$\boldsymbol{F_{x_g}[N]}$	0.0024	7.47e-4	0.0063	0.0020	9.09e-4	2.81e-4
$\boldsymbol{F_{y_g}[N]}$	0.0017	0.0017	0.0045	0.0044	6.33e-4	6.36e-4

Source: Own author.

Figure 50 – Comparison of the static analysis results.

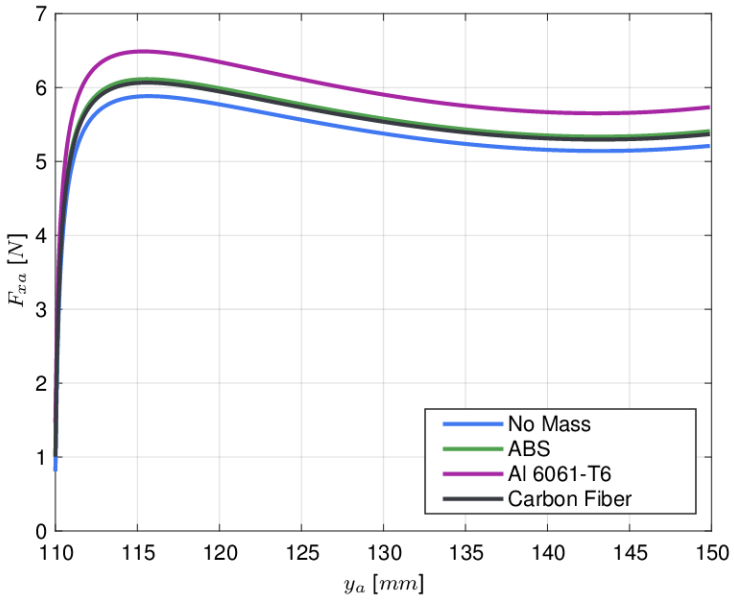

(a) F_{x_a}.

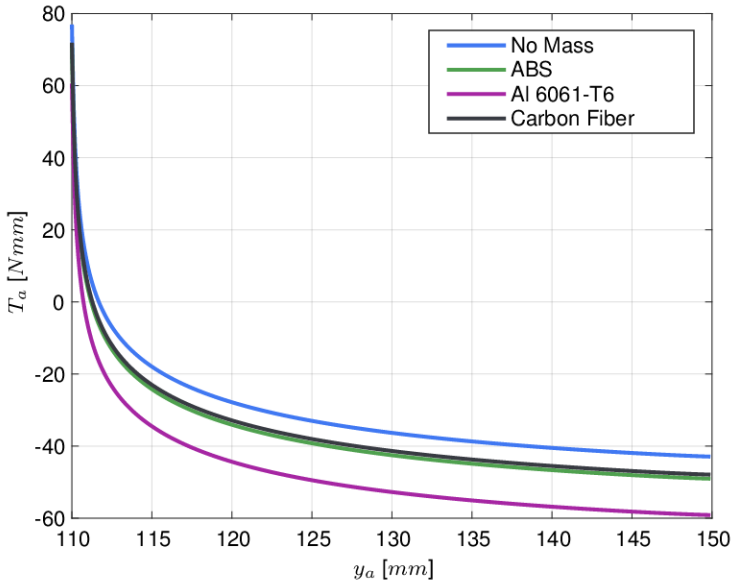

(b) T_a.

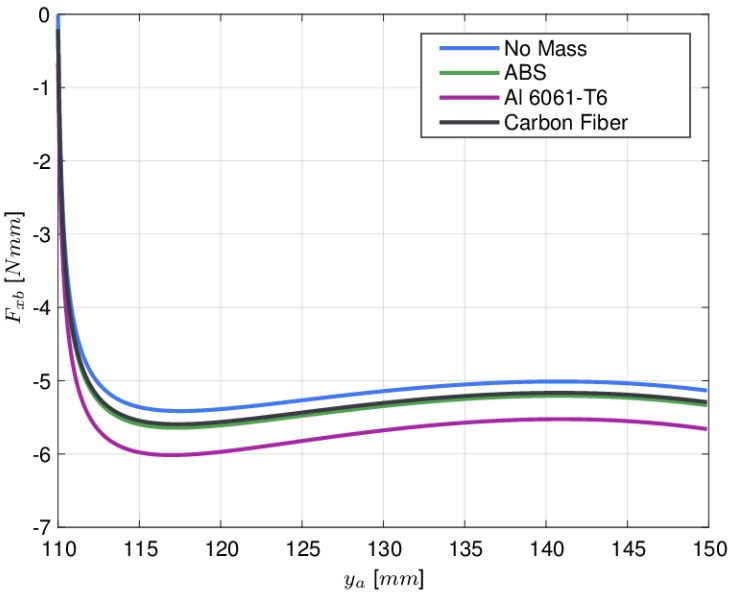

(c) F_{x_b}, F_{x_c} and F_{x_d}.

Figure 51 – Comparison of the static analysis results.

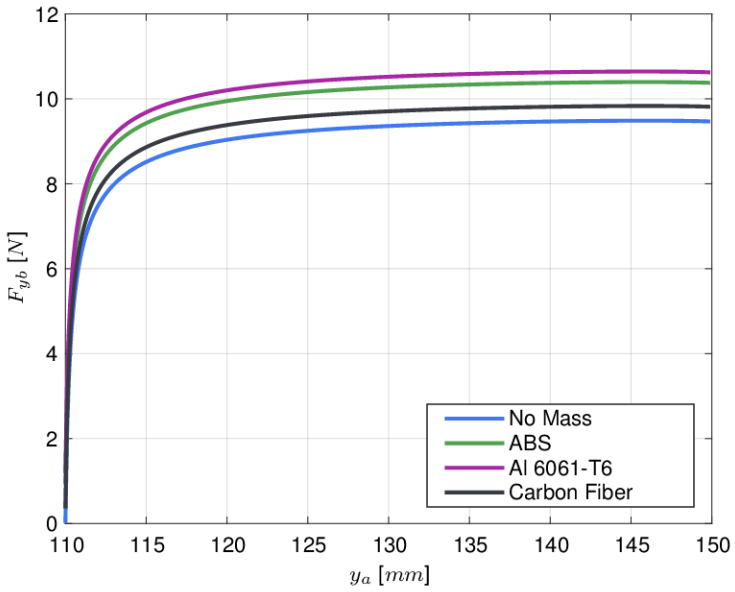

(a) F_{y_b}, F_{y_c} and F_{y_d}.

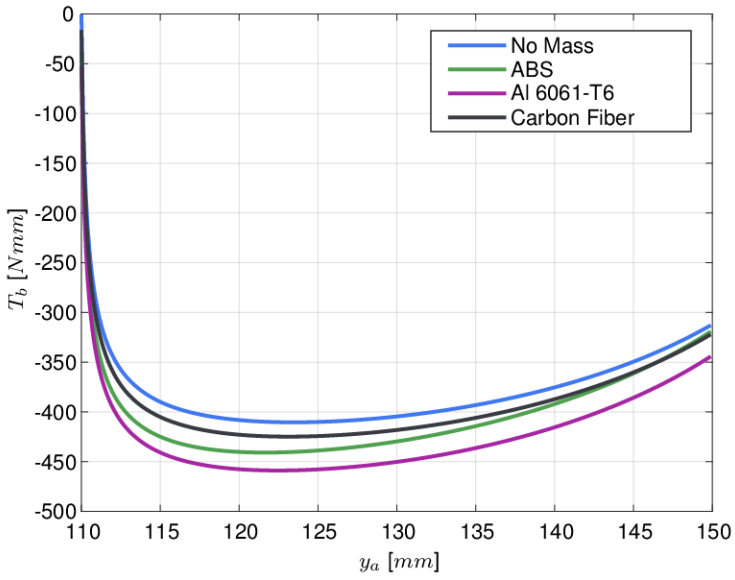

(b) T_b.

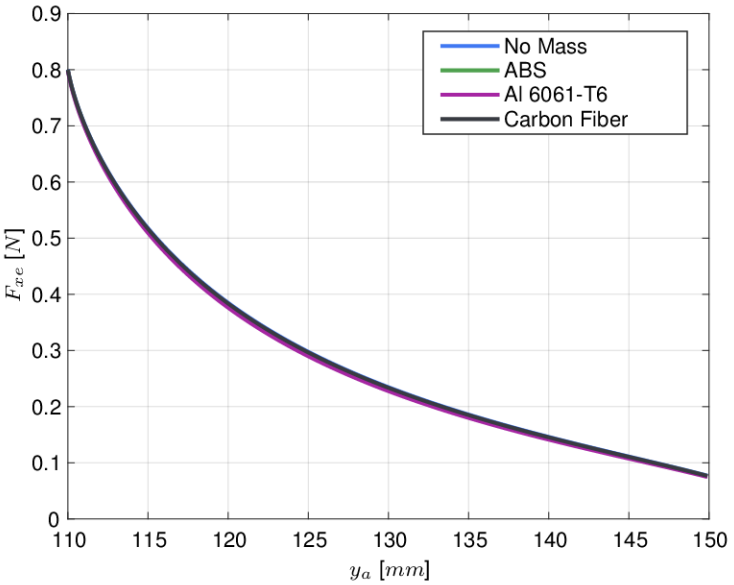

(c) F_{x_e} and F_{x_f}.

Figure 52 – Comparison of the static analysis results.

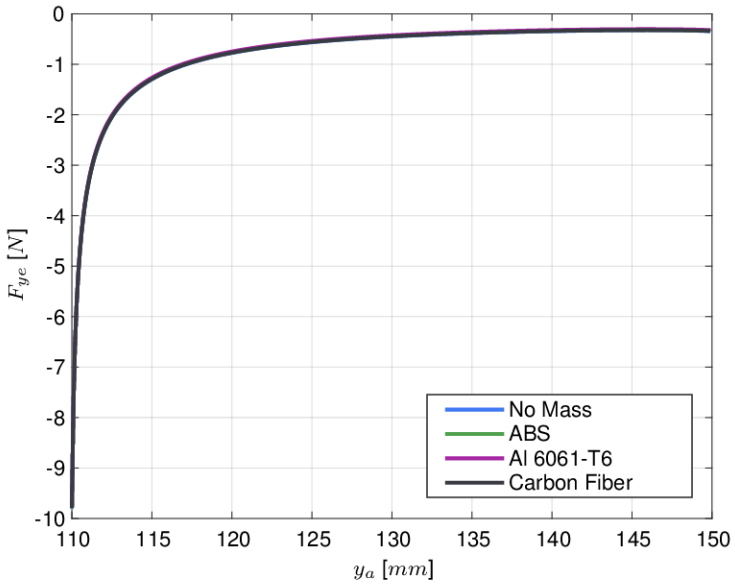

(a) F_{y_e} and F_{y_f}.

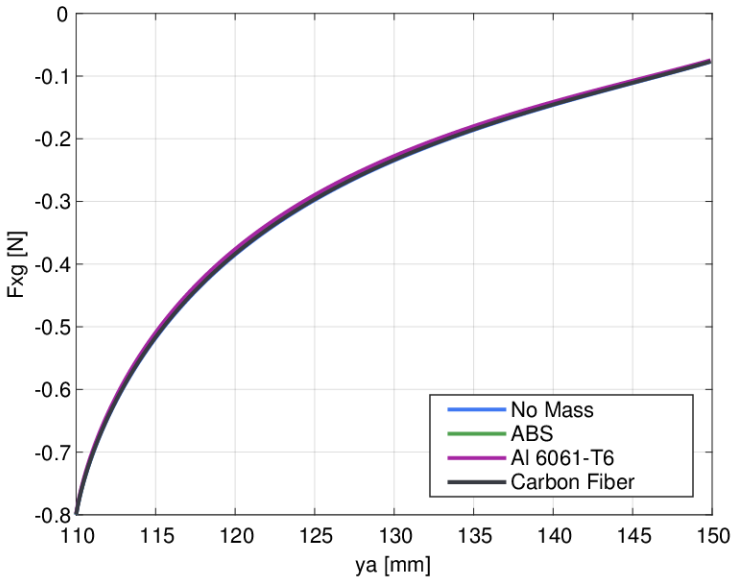

(b) F_{x_g}.

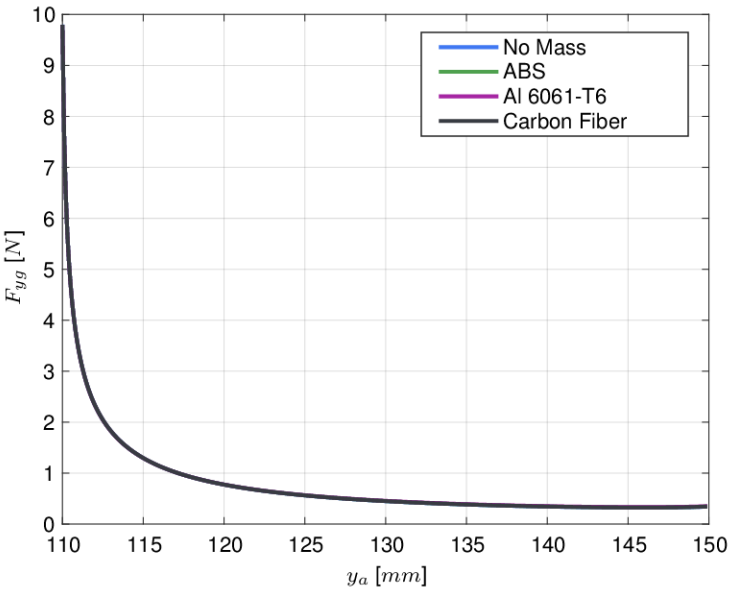

(c) F_{y_g}.

6 SPATIAL MECHANISM

The gripper's analysis has been explored throughout this work considering a planar workspace. This chapter explores the spatial analysis of the mechanism. Section 6.1 presents a method to extend the kinematic analysis previously performed on the planar mechanism to the spatial workspace. Section 6.2 performs the self-alignment analysis of the gripper, as described in Section 3.5. Section 6.3 performs a new static analysis, this time considering the spatial workspace. Finally, Section 6.4 draws some final considerations.

6.1 FINGER DISTRIBUTION

Chapters 4 and 5 presented the development of a single finger. The gripper's final topology can be obtained by distributing the required number of fingers around the centered prismatic joint. Figure 53 presents a tridimensional view of the UAV landing on top of the gripper. This chapter presents the analysis of the extended mechanism to a spatial workspace.

The procedure adopted through chapters 4 and 5 considered a single planar finger. The coordinates calculated in Section 4.3.1 may be expanded to a spatial workspace through a rotation around the y axis. Therefore, let $\boldsymbol{x}$ be the coordinates of a random point in space. The rotation of $\boldsymbol{x}$ around the y axis can be calculated through a rotation matrix, as presented by Eq. 69.

$$\boldsymbol{x} = \begin{bmatrix} \cos(\alpha) & 0 & \sin(\alpha) \\ 0 & 1 & 0 \\ -\sin(\alpha) & 0 & \cos(\alpha) \end{bmatrix} \boldsymbol{x_i} \tag{69}$$

This work considers a gripper composed of four fingers equally distributed around the center prismatic joint. Hence, applying Eq. 69 to all joints results in the distribution presented by Fig. 54. Although joints e, f, and g are not visible, the same rule applies.

6.2 SELF-ALIGNMENT

Section 3.5 presented an overview of the self-alignment concept and Reshetov's table method. This section aims to determine if the gripper is overconstrained and adapt it to a self-aligned mechanism. Similar to the grippers synthesis process, the self-alignment analysis can also be performed on a single finger, and the results extended to the other members.

The gripper is composed of two loops, $abcd$, and $aefg$, which are identified in Fig. 33. The mobility of the mechanism is provided by joint a. Therefore, any loop that

Figure 53 – Tridimensional view of the UAV landing on top of the spatial gripper.

Source: Own author.

does not include joint a does not have any mobility. Considering that the mechanism should preserve the self-alignment characteristics when adding an indefinite number of fingers, joint a will not be considered part of any loop. This way, Reshetov's method will result in two loops (one for the finger and one for the locking mechanism) with zero mobility. Nevertheless, when added to the gripper's mechanism, they will preserve the self-alignment characteristic of the entire mechanism.

Table 11 presents Reshetov's table, containing the degrees of freedom provided by each loop. It can be seen that each loop has three redundant constraints, two rotational constraints, and a translational constraint, resulting in a total of 6 redundant constraints. Therefore, to obtain a self-aligning mechanism, it is necessary to replace some of the gripper's current joints.

The first evaluated option was to replace all revolute joints with universal joints. Applying Reshetov's table, this solution would result in a mechanism free from overconstrains, as presented in Table 12. However, the development of this approach through a CAD software showed that this solution would not be practical due to joints c and f

Figure 54 – Top view of the spatial distribution.

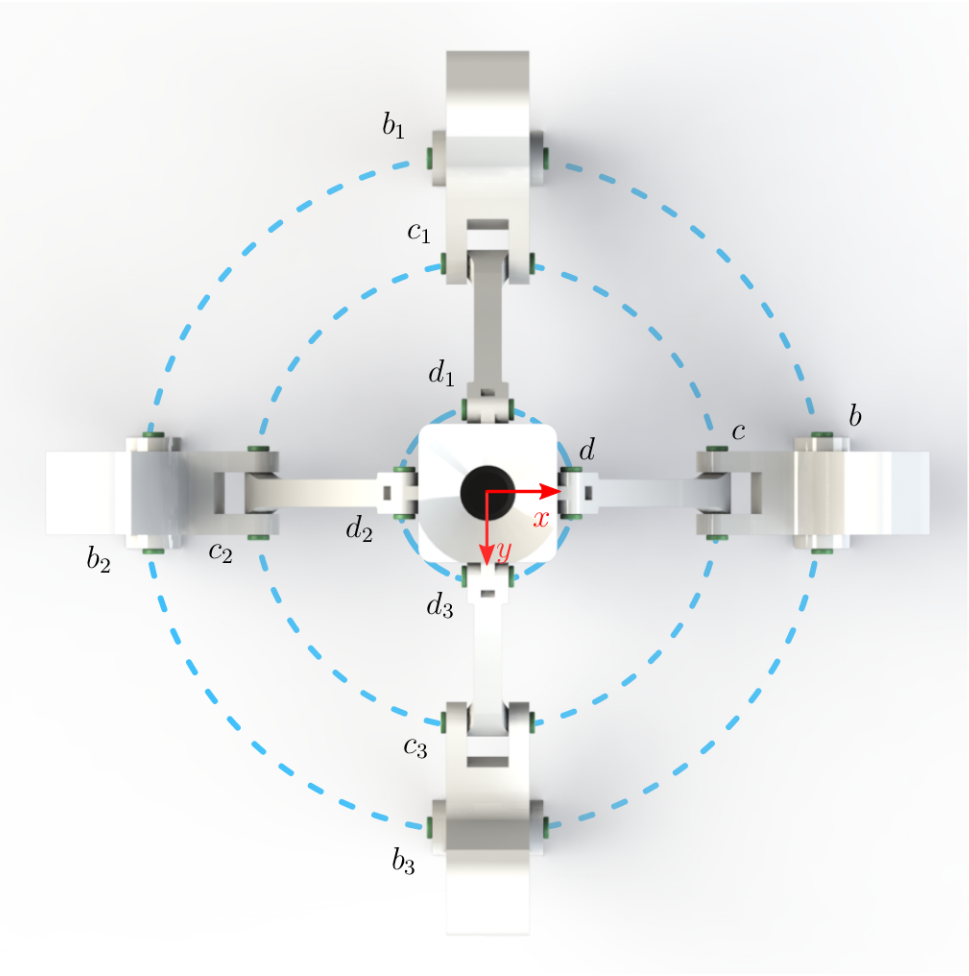

Source: Own author.

Table 11 – Reshetov's table of the gripper mechanism.

Loop bcd			
$\boldsymbol{R_x}$	0	$\boldsymbol{T_x}$	0 (c)
$\boldsymbol{R_y}$	0	$\boldsymbol{T_y}$	0 (d)
$\boldsymbol{R_z}$	$b\ c\ d$	$\boldsymbol{T_z}$	0

Loop efg			
$\boldsymbol{R_x}$	0	$\boldsymbol{T_x}$	0 (f)
$\boldsymbol{R_y}$	0	$\boldsymbol{T_y}$	0 (g)
$\boldsymbol{R_z}$	$e\ f\ g$	$\boldsymbol{T_z}$	0

Source: Own author.

angular displacement.

The second attempt was to replace joints c and f with spherical joints, adding two degrees of freedom to each loop, and joints d and e to universal joints, adding the last degree of freedom needed for each loop. Table 13 confirms that this configuration does not result in an overconstrained mechanism. Figure 55 presents the final, self-

Table 12 – Reshetov's table of the gripper mechanism using universal joints.

Loop bcd				Loop efg			
$\boldsymbol{R_x}$	c	$\boldsymbol{T_x}$	$0\ (c)$	$\boldsymbol{R_x}$	f	$\boldsymbol{T_x}$	$0\ (f)$
$\boldsymbol{R_y}$	$b\ d$	$\boldsymbol{T_y}$	$0\ (d)$	$\boldsymbol{R_y}$	$e\ g$	$\boldsymbol{T_y}$	$0\ (g)$
$\boldsymbol{R_z}$	$b\ c\ d$	$\boldsymbol{T_z}$	$0\ (b)$	$\boldsymbol{R_z}$	$e\ f\ g$	$\boldsymbol{T_z}$	$0\ (e)$

Source: Own author.

Table 13 – Reshetov's table of the gripper mechanism using spherical joints.

Loop bcd				Loop efg			
$\boldsymbol{R_x}$	c	$\boldsymbol{T_x}$	$0\ (b)$	$\boldsymbol{R_x}$	f	$\boldsymbol{T_x}$	$0\ (f)$
$\boldsymbol{R_y}$	$c\ d$	$\boldsymbol{T_y}$	$0\ (c)$	$\boldsymbol{R_y}$	$e\ f$	$\boldsymbol{T_y}$	$0\ (g)$
$\boldsymbol{R_z}$	$b\ c\ d$	$\boldsymbol{T_z}$	$0\ (d)$	$\boldsymbol{R_z}$	$e\ f\ g$	$\boldsymbol{T_z}$	$0\ (e)$

Source: Own author.

aligned gripper. Figure 56a presents a closer look at the universal joint used in joints d and e, and Fig. 56b a close-up of the spherical joints used in joints c and f. To prevent a mechanical constraint in joint c, there is a gap between links 2 and 3, as presented in Figure 56c.

6.3 STATIC ANALYSIS OF SELF-ALIGNED MECHANISM

A new static analysis is performed to the final gripper to evaluate if the behavior of the spatial mechanism is coherent to the results obtained from the planar analysis. Figure 57 presents the expanded graph representation, along with cut a. Since the other cuts follow the same pattern used in Sections 4.4.1, 4.4.2, and 5.3, they are omitted here.

Initially, the static analysis is performed without considering the weight of the links. From the graph representation, this analysis is composed of 17 cuts and eight chords. The self-aligned mechanism comprises eight spherical joints, eight universal joints, eight revolute joints, and a cylindric joint, which results in a hundred constraints imposed by the joints of the mechanism. Adding the external action of the UAV's weight, the four torsion springs, and four output torques in joints b_i result in 109 constraints,

Figure 55 – Tridimensional view of the self-aligned gripper.

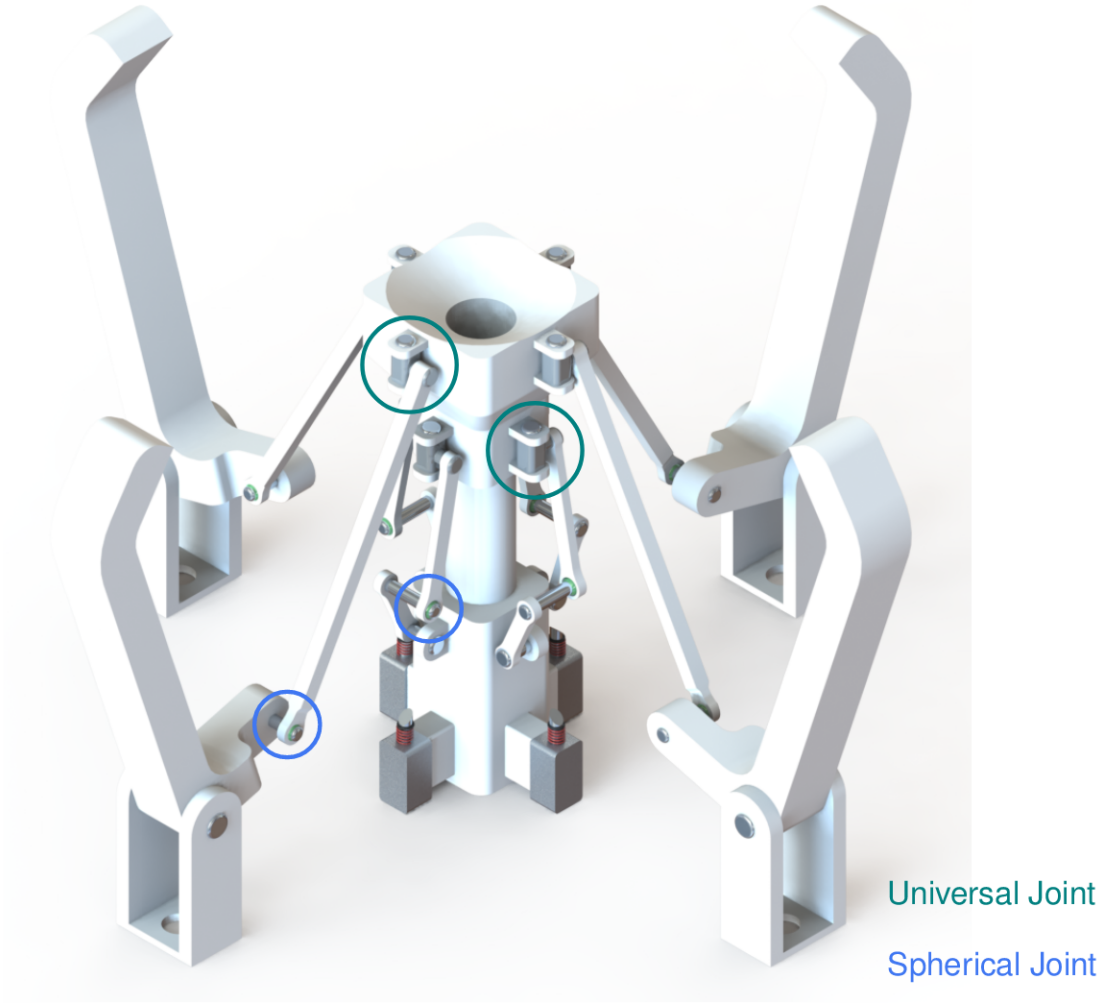

Source: Own author.

Figure 56 – Close-up look of the gripper's universal and spherical joints.

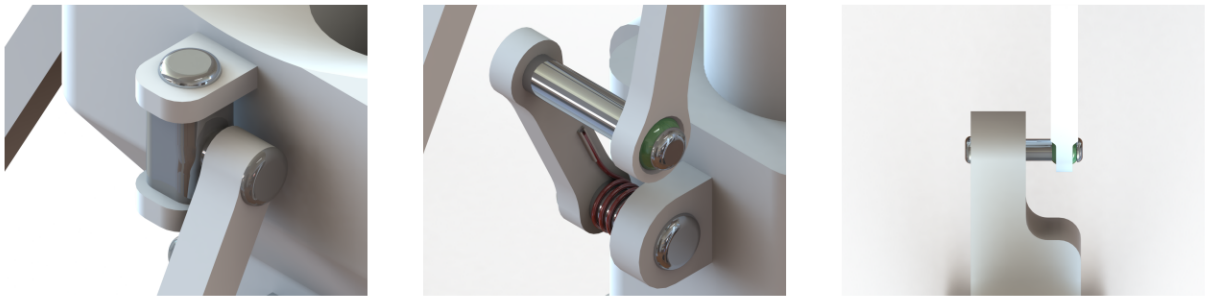

(a) Universal joint. (b) Spherical joint. (c) Spherical joint (top view).

Source: Own author.

which means the cutset matrix Q is a 17×105 matrix. Hence, the network action matrix, A_N, is a 102×109 matrix. When considering the weight of the links, there are 17 extra loads. Hence, the Q matrix is extended to a 17×126 matrix, and A_N is extended to a

Figure 57 – Gripper's graph representation with every cut for the spatial mechanism.

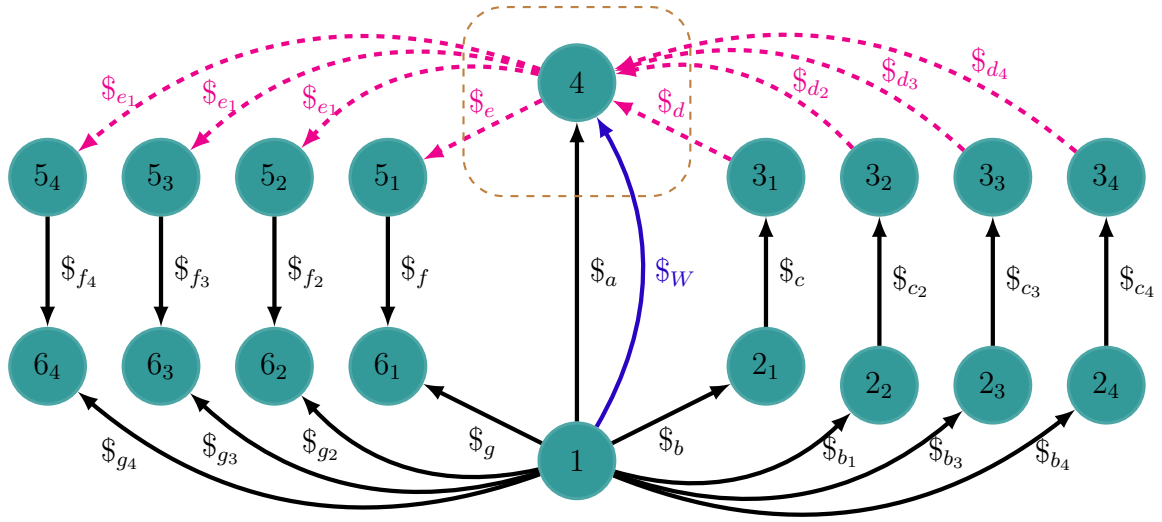

Source: Own author.

102×126 matrix.

Since the torque produced by the torsion springs and the UAV's weight are known, this problem has five primary variables. Once the network action matrix is manipulated according to Eq. 26, the A_N matrix is transformed to a 102×104. The same applies when considering the weight of the links, as all the extra loads are known variables. This analysis was carried out only for ABS manufactured links. There are topological differences between the tridimensional self-aligned gripper evaluated in this section and the planar gripper evaluated in Section 4.4.1, such as the universal and spherical joints. However, for comparison reasons, the weights considered in this analysis are the same presented in Table 9.

A problem faced in this analysis is the redundancy of the mechanism's configuration. Mathematically, the UAV's weight may be distributed to the fingers in an infinite number of combinations. Since the static analysis of the planar finger considered an even distribution of the external load, extra equations may be added to the system of equations as an attempt to force this even distribution. This is accomplished by specifying that the reaction forces in joints d_1, d_2, d_3 and d_4 are equivalent, as are e_1, e_2, e_3 and e_4. The extra equations are presented in Eq. 70. Hence, the network action matrix is extended to 108×104. As the number of lines is greater than the number of columns, this is an overdetermined system of equations.

$$
\begin{aligned}
F_{y_{d1}} - F_{y_{d2}} &= 0 \\
F_{y_{d2}} - F_{y_{d3}} &= 0 \\
F_{y_{d3}} - F_{y_{d4}} &= 0 \\
F_{y_{e1}} - F_{y_{e2}} &= 0 \\
F_{y_{e2}} - F_{y_{e3}} &= 0 \\
F_{y_{e3}} - F_{y_{e4}} &= 0
\end{aligned}
\tag{70}
$$

The results obtained from the tridimensional analysis were compared to the ones obtained for the planar mechanism. The output torque in joints b_1 were plotted in function of the y coordinate of the cylindrical joint a, and compared to the output in joint b from the planar analysis, which resulted in a perfectly overlapped graph, as presented in Fig. 58. The same happens for the tridimensional static analysis considering the weight of the links. Figure 59a presents the results of the output torque in joints b_1 and b_2, and Fig. 59b presents the output torque in joints b_3 and b_4 for both tridimensional analyses. It is possible to see the similarity of the results on Fig. 59a and Fig. 51b.

Figure 58 – Plot of the output torque in joint b_1 obtained from the planar static analysis and tridimensional static analysis.

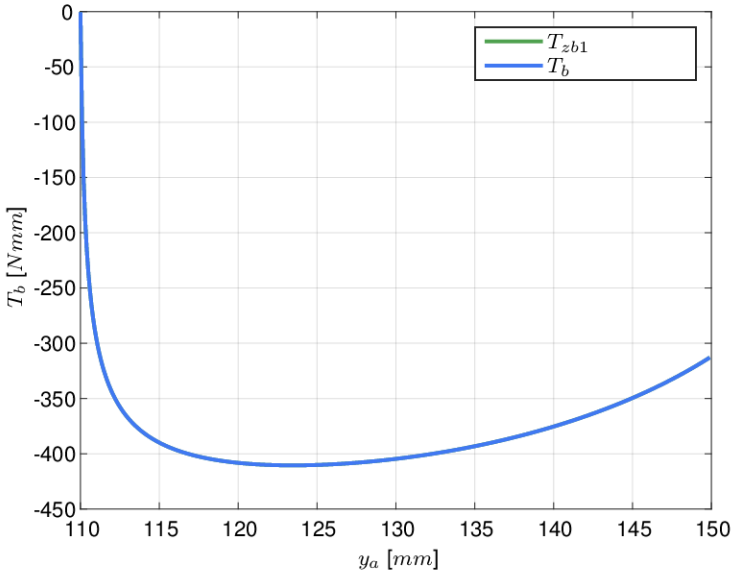

Source: Own author.

Unlike the planar analysis, where the reaction force and torque on joint a vary along with the closing motion, as presented in Fig. 50a, in the tridimensional case, all reaction forces and torques are zero for the entire range of motion. Since the mechanism is symmetric, it was expected that the forces acting on joint a would cancel each other out. The other reaction forces were also compared, and no other differences were observed.

Figure 59 – Output torque in joint b_i for both tridimensional static analyses.

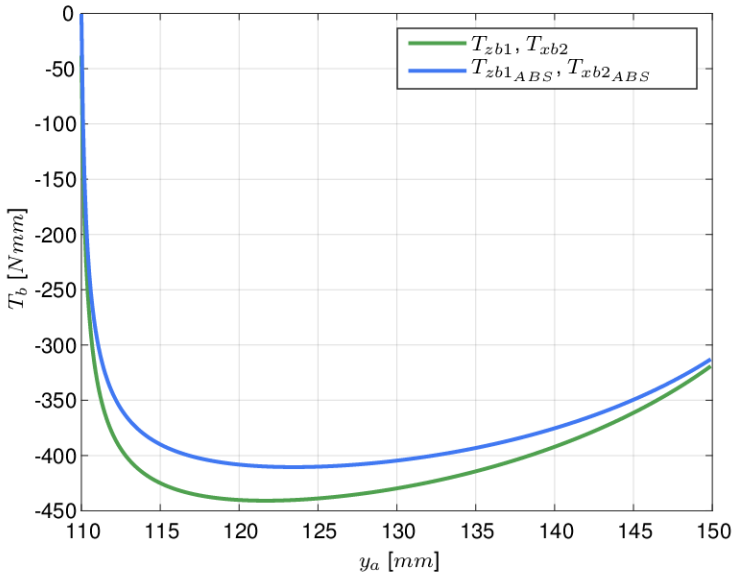

(a) $T_{z_{b1}}$ and $T_{x_{b2}}$.

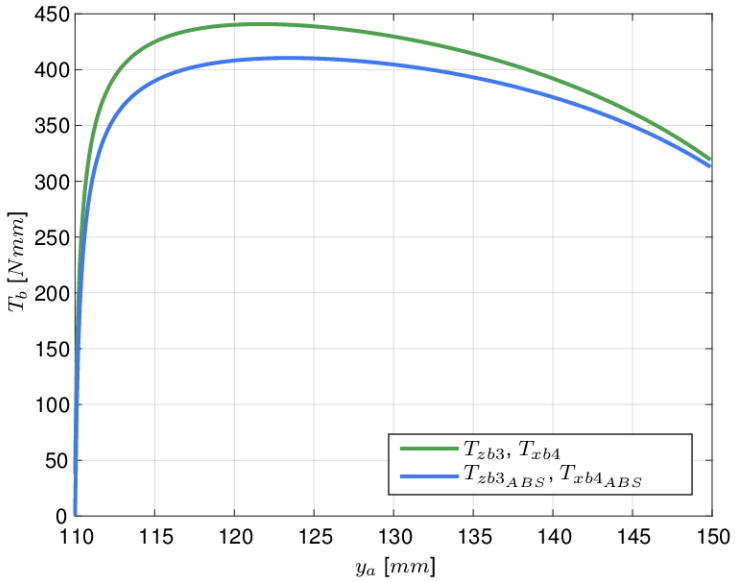

(b) $T_{z_{b3}}$ and $T_{x_{b4}}$.

Source: Own author.

6.4 CHAPTER OVERVIEW

This chapter explored the spatial configuration of the gripper mechanism. At first, Section 6.1 applied a rotation matrix to extend the planar mechanism to the spatial workspace. Next, Section 6.2 conducted a self-alignment analysis, identifying the redundant constraints present on the gripper. Afterwards, some joints were replaced to achieve a self-aligning mechanism. Finally, Section 6.3 described the static analysis performed on the spatial, self-aligned mechanism, which presented results obtained coherent to the results from the planar mechanism.

7 FINAL CONSIDERATIONS AND FUTURE WORK

The main objective of this master thesis was to develop a passive gripping device to be employed with unmanned aerial vehicles and being capable of attaching the UAV to the payload remotely. This new device might contribute to the fast-growing transport and logistics sector adopting UAVs.

The growth of the UAV market over the last few years triggered an interest in the research and development of UAV-related devices. Therefore, the first specific objective defined in this work was to evaluate the current state-of-the-art technologies for remote load transport through UAVs. This research allowed a better understanding of the explored approaches of remote load transport and the main challenges faced in this area. A survey on the recent developments of UAV docking systems was also performed, which contributed to the analysis of several geometrical shapes and possible approaches for connecting the UAV to the payload.

The next specific objective was to develop a new mechanism topology capable of remotely grasping a load. From the state-of-the-art survey conducted, it was possible to establish the required and desired requirements of the final mechanism. These characteristics were used to enumerate and select the kinematic chain that best fits the listed features and define which kinematic pairs should be employed. Afterwards, the new topology was mathematically modeled through Natural Coordinates, and a dimensional optimization process using an evolutionary algorithm was carried out. To simplify the process, this initial development considered a single gripper's finger, operating on a planar workspace. Then, multiple fingers would be used to define a spatial, symmetric gripping device.

Once the new, optimized topology has been achieved, it was possible to perform the static analysis of the new mechanism. Initially, the study was conducted for the gripper's closing motion as the UAV grasps the object, analyzing the reaction forces of the joints throughout the entire range of motion. Then, a new static analysis was performed considering the aerial transport of a package. Both analyses were implemented considering the characteristics of a DJI Spreading Wings S900 UAV, such as its maximum takeoff-weight capacity and geometrical constraints. The results of the reaction forces on each joint allowed to estimate the internal stresses of the gripper's links, and consequently, to estimate the cross-section area and the weight of the links. Therefore, new analyses were conducted, considering the weight of the links for three different materials. This new analysis permitted the comparison of the results and evaluation of the effect of the link's weight on the static behavior of the system.

Finally, the gripper was extended to a spatial workspace, and a self-alignment process was carried out. The resulting self-aligned mechanism was subjected to a new static analysis, considering the spatial workspace. The results obtained from this

last analysis were coherent to the results obtained for the planar mechanism, which indicates that the simplification adopted at the beginning of this work did not affect the final outcome.

Finally, it can be concluded that the adopted method for developing a UAV gripping device has been successfully implemented. This method must consider the geometric constraints of the UAV, and therefore a specific UAV was selected. However, the process is replicable for any other aerial vehicle.

7.1 SUGGESTIONS FOR FUTURE WORK

Even though the development presented in this work focused on the gripper mechanism, further development is still required. Some topics are presented in this section as suggestions for future work.

- A prototype of the final mechanism should be built to run tests with a real UAV.
- During an aerial transport, some maneuvers may generate dynamic loads. An evaluation of these dynamic loads and their possible effects should be performed.
- The structural analysis performed in this work was useful to estimate the weight and the cross-section area of the links, but it does not necessarily represent the best structural option. Therefore, a structural optimization should be conducted for this topology.
- The operational safety of load transport through UAVs relies on the stiffness of the mechanism. Therefore, a stiffness analysis should be performed.
- So far, little attention has been given to the structure fixed to the UAV to accomplish the coupling. A structural optimization should be performed for this element to reduce the overall weight.

REFERENCES

ALMEIDA, Bruno Seixas Gomes de; LEITE, Victor Coppo. Particle swarm optimization: A powerful technique for solving engineering problems. In: SWARM Intelligence-Recent Advances, New Perspectives and Applications. [S.l.]: IntechOpen, 2019.

ANTONINI, Roberto; FICI, Gian Piero; GASPARDONE, Marco. **Landing platform for an unmanned aerial vehicle**. [S.l.]: Google Patents, Oct. 2019. US Patent 10,434,885.

ARORA, Jasbir Singh. **Introduction to optimum design**. [S.l.]: Elsevier, 2004.

AVELLO-ITURRIAGAGOITIA, Alejo. **Teoria de maquinas**. [S.l.]: Tecnun, Universidad de Navarra, 2014. Segunda Edición.

BARBASOV K.V.; BARBASOV, V.K. **System of Landing of Unmanned Aerial Vehicle and Landing Vehicle ofVertical Take-Off and Landing.** [S.l.]: Google Patents, Nov. 2017. RU Patent 2666975-C1.

BUDYNAS, Richard Gordon; NISBETT, J Keith, et al. **Shigley's mechanical engineering design**. [S.l.]: McGraw-Hill New York, 2011. v. 9.

CAMPO, E. **The complete part design handbook: for injection molding of thermoplastics**. [S.l.]: Cincinnati: HanserGardnerPublications, c2006, xxi.

CARRETO, Victor. **Estudo de mecanismos auto-alinháveis usando análise de dependências estáticas e cinemáticas**. 2010. S. 162. MA thesis – Universidade Federal de Santa Catarina, Centro Tecnológico, Programa de Pós-graduação em Engenharia Mecânica, Florianópolis, SC.

CAZANGI, Humberto Reder. **Aplicação do método de Davies para análise cinemática e estática de mecanismos com múltiplos graus de liberdade**. 2008. S. 290. MA thesis – Universidade Federal de Santa Catarina, Centro Tecnológico, Programa de Pós-graduação em Engenharia Mecânica, Florianópolis, SC.

COMPAGNIN, Alberto et al. Autoport Project: a Docking Station for Planetary Exploration Drones. In: 55TH AIAA Aerospace Sciences Meeting. [S.l.: s.n.], 2017. P. 1680.

CONTROZZI, Marco; CIPRIANI, Christian; CARROZZA, Maria Chiara. Miniaturized non-back-drivable mechanism for robotic applications. **Mechanism and Machine Theory**, Elsevier, v. 45, n. 10, p. 1395–1406, 2010.

CRUZ, Patricio; FIERRO, Rafael. Cable-suspended load lifting by a quadrotor UAV: hybrid model, trajectory generation, and control. **Autonomous Robots**, v. 41, p. 1629–1643, 2017.

DAVIES, TH. Kirchhoff's circulation law applied to multi-loop kinematic chains. **Mechanism and machine theory**, Elsevier, v. 16, n. 3, p. 171–183, 1981.

DE JALON, J Garcia; UNDA, J; AVELLO, Al. Natural coordinates for the computer analysis of multibody systems. **Computer Methods in Applied Mechanics and Engineering**, Elsevier, v. 56, n. 3, p. 309–327, 1986.

DOWNEY, Kris; PARKINSON, Alan; CHASE, Ken. An introduction to smart assemblies for robust design. **Research in Engineering Design**, Springer, v. 14, n. 4, p. 236–246, 2003.

DRONE INDUSTRY INSIGHTS. **THE DRONE MARKET SIZE 2020-2025: 5 KEY TAKEAWAYS**. [S.l.: s.n.], 2021. https://droneii.com/the-drone-market-size-2020-2025-5-key-takeaways. Disponível em: https://droneii.com/the-drone-market-size-2020-2025-5-key-takeaways.

ELLIOTT, Grant et al. The biomechanics and energetics of human running using an elastic knee exoskeleton. In: IEEE. 2013 IEEE 13th international conference on rehabilitation robotics (ICORR). [S.l.: s.n.], 2013. P. 1–6.

ERTHAL, Jorge Luiz. **Modelo cinestático para análise de rolagem em veículos**. 2010. S. 130. PhD thesis – Universidade Federal de Santa Catarina, Centro Tecnológico, Programa de Pós-graduação em Engenharia Mecânica, Florianópolis, SC.

GEEROMS, J. et al. Ankle-Knee prosthesis with powered ankle and energy transfer for CYBERLEGs α-prototype. In: 2013 IEEE 13th International Conference on Rehabilitation Robotics (ICORR). [S.l.: s.n.], 2013. P. 1–6. DOI: 10.1109/ICORR.2013.6650352.

GLOBE NEWSWIRE. **The global UAV market is estimated to be USD 27.4 billion in 2021**. [S.l.: s.n.], 2021. https://www.globenewswire.com/news-release/2021/06/18/2249504/0/en/The-global-UAV-market-is-estimated-to-be-USD-27-4-billion-in-2021-and-is-projected-to-reach-USD-58-4-billion-by-2026-at-a-CAGR-of-16-4.html. Disponível em: https://www.precedenceresearch.com/unmanned-aerial-vehicle-market.

GU, Hao; CECCARELLI, Marco; CARBONE, Giuseppe. An experimental characterization of a 1-DOF anthropomorphic arm for humanoid robots. In: 13TH WSEAS International Conference on Computers. [S.l.: s.n.], 2009. P. 92–99.

GUPTA, Anunay et al. Advances of UAVs toward Future Transportation: The State-of-the-Art, Challenges, and Opportunities. **Future Transportation**, Multidisciplinary Digital Publishing Institute, v. 1, n. 2, p. 326–350, 2021.

HARTENBERG, Richard; DENAVIT, Jacques. **Kinematic synthesis of linkages**. [S.l.]: New York: McGraw-Hill, 1964.

HAUPT, Randy L; ELLEN HAUPT, Sue. Practical genetic algorithms. Wiley Online Library, 2004.

HIBBELER, R. **Mechanics of materials**. [S.l.]: Pearson, New York, 2017. 10th edition.

HILD, Manfred; SIEDEL, Torsten; GEPPERT, Tim. Design of a passive, bidirectional overrunning clutch for rotary joints of autonomous robots. In: SPRINGER. INTERNATIONAL Conference on Intelligent Robotics and Applications. [S.l.: s.n.], 2011. P. 397–405.

HIRZINGER, Gerd et al. On a new generation of torque controlled light-weight robots. In: IEEE. PROCEEDINGS 2001 ICRA. IEEE International Conference on Robotics and Automation (Cat. No. 01CH37164). [S.l.: s.n.], 2001. P. 3356–3363.

HUANG, Zhen; LI, Qinchuan; DING, Huafeng. Basics of screw theory. In: THEORY of Parallel Mechanisms. [S.l.]: Springer, 2013. P. 1–16.

KARSSEN, J; WISSE, M. Running robot phides. In: DYNAMIC Walking Conference. [S.l.: s.n.], 2012.

KESSENS, Chad C et al. Versatile aerial grasping using self-sealing suction. In: IEEE. 2016 IEEE international conference on robotics and automation (ICRA). [S.l.: s.n.], 2016. P. 3249–3254.

KRAUSS, Ran; KLINER, Meir. **Centering and Landing Platform for Hovering Flying Vehicles**. [S.l.]: Google Patents, May 2020. US Patent App. 16/073,399.

LEE, Wen-Tzong; RUSSELL, Kevin. Developments in quantitative dimensional synthesis (1970–present): four-bar path and function generation. **Inverse Problems in Science and Engineering**, Taylor & Francis, v. 26, n. 9, p. 1280–1304, 2018.

LI, Bing; DENG, Qiang; LIU, Zhichao. A spherical hopping robot for exploration in complex environments. In: IEEE. 2009 IEEE International Conference on Robotics and Biomimetics (ROBIO). [S.l.: s.n.], 2009. P. 402–407.

MARTINS, Daniel; MURAI, Estevan Hideki. **Mecanismos: síntese e análise com aplicações em robótica**. [S.l.]: UFSC, 2019.

MATHIJSSEN, Glenn; LEFEBER, Dirk; VANDERBORGHT, Bram. Variable recruitment of parallel elastic elements: Series–parallel elastic actuators (SPEA) with dephased mutilated gears. **IEEE/ASME Transactions on Mechatronics**, IEEE, v. 20, n. 2, p. 594–602, 2014.

MELLINGER, Daniel et al. Cooperative grasping and transport using multiple quadrotors. In: DISTRIBUTED autonomous robotic systems. [S.l.]: Springer, 2013. P. 545–558.

MINGXI HANPING, Xiangyu; YUAN. **Positioning Mechanism and UAV Base Station Using Positioning Mechanism**. [S.l.]: Google Patents, Nov. 2014. CN Patent 204250382-U.

MITSUI, Kazuki; OZAWA, Ryuta; KOU, Toshiyuki. An under-actuated robotic hand for multiple grasps. In: 2013 IEEE/RSJ International Conference on Intelligent Robots and Systems. [S.l.: s.n.], 2013. P. 5475–5480. DOI: 10.1109/IROS.2013.6697149.

MOHIUDDIN, Abdullah et al. A survey of single and multi-UAV aerial manipulation. **Unmanned Systems**, World Scientific, v. 8, n. 02, p. 119–147, 2020.

MONKMAN, Gareth J et al. **Robot grippers**. [S.l.]: John Wiley & Sons, 2007.

MURAI, Estevan Hideki. **Number synthesis methods for mechanism design : an alternative approach / Estevan Hideki Murai ; orientador, Daniel Martins, coorientador, Roberto Simoni**. 2019. PhD thesis – Universidade Federal de Santa Catarina, Centro Tecnológico, Programa de Pós-graduação em Engenharia Mecânica, Florianópolis, SC. Disponível em: http://www.bu.ufsc.br/teses/PEMC1939-T.pdf.

NARIMAN-ZADEH, N. et al. Pareto optimal synthesis of four-bar mechanisms for path generation. **Mechanism and Machine Theory**, Pergamon, v. 44, n. 1, p. 180–191, 2009. ISSN 0094114X. DOI: 10.1016/j.mechmachtheory.2008.02.006.

NEUBAUER, Martin; GÜNTHER, Georg; FÜLLHAS, Konrad. **Structural design aspects and criteria for military UAV**. [S.l.], 2007.

NIU, Chunyun; NIU, Michael C. **Airframe structural design: practical design information and data on aircraft structures**. [S.l.]: Conmilit Press, 1988.

NUÑEZ, Neider Nadid Romero. **Síntese estrutural e otimização dimensional de mecanismos de direção**. 2014. S. 97. MA thesis – Universidade Federal de Santa Catarina, Centro Tecnológico, Programa de Pós-Graduação em Engenharia Mecânica, Florianópolis, SC.

PALPACELLI, Matteo; CARBONARI, Luca; PALMIERI, Giacomo. A lockable spherical joint for robotic applications. In: IEEE. 2014 IEEE/ASME 10th International Conference on Mechatronic and Embedded Systems and Applications (MESA). [S.l.: s.n.], 2014. P. 1–6.

PARROTT, Christopher; DODD, Tony J.; GROSS, Roderich. HiGen: A high-speed genderless mechanical connection mechanism with single-sided disconnect for self-reconfigurable modular robots. In: 2014 IEEE/RSJ International Conference on

Intelligent Robots and Systems. [S.l.: s.n.], 2014. P. 3926–3932. DOI: 10.1109/IROS.2014.6943114.

PLOOIJ, Michiel et al. Lock your robot: A review of locking devices in robotics. **IEEE Robotics & Automation Magazine**, IEEE, v. 22, n. 1, p. 106–117, 2015.

PR NEWSWIRE. **Drone Logistics and Transportation Market Size**. [S.l.: s.n.], 2021. https://www.prnewswire.com/in/news-releases/drone-logistics-and-transportation-market-size-to-reach-usd-10-990-million-by-2026-at-cagr-10-8-valuates-reports-857193310.html. Disponível em: https://www.prnewswire.com/in/news-releases/drone-logistics-and-transportation-market-size-to-reach-usd-10-990-million-by-2026-at-cagr-10-8-valuates-reports-857193310.html.

PRECEDENCE RESEARCH. **Unmanned Aerial Vehicle Market Size**. [S.l.: s.n.], 2021. https://www.precedenceresearch.com/unmanned-aerial-vehicle-market. Disponível em: https://www.precedenceresearch.com/unmanned-aerial-vehicle-market.

RESHETOV, L. **Self-aligning mechanism,2nd revised edition**. [S.l.]: MIR, Moscow, 1979.

ROSA, Fabíola da Silva. **Sistemática para o desenvolvimento de atuadores com rigidez variável utilizando metodologia para o projeto de mecanismos**. 2018. S. 140. MA thesis – Universidade Federal de Santa Catarina, Centro Tecnológico, Programa de Pós-Graduação em Engenharia Mecânica, Florianópolis, SC.

SADRAEY, Mohammad. Unmanned aircraft design: A review of fundamentals. **Synthesis Lectures on Mechanical Engineering**, Morgan & Claypool Publishers, v. 1, n. 2, p. i–193, 2017.

SCIENCE, Korea Advanced Institute of; TECHNOLOGY. **APPARATUS AND METHOD FOR SUPPLYING POWER OF DRONE**. [S.l.]: Google Patents, Aug. 2016. KR Patent 101858619-B1.

SHIMAHARA, Syohei et al. Aerial torsional manipulation employing multi-rotor flying robot. In: IEEE. 2016 IEEE/RSJ International Conference on Intelligent Robots and Systems (IROS). [S.l.: s.n.], 2016. P. 1595–1600.

SIMONI, Roberto; CARBONI, Andrea Piga; MARTINS, Daniel. Enumeration of kinematic chains and mechanisms. **Proceedings of the Institution of Mechanical Engineers, Part C: Journal of Mechanical Engineering Science**, SAGE Publications Sage UK: London, England, v. 223, n. 4, p. 1017–1024, 2009.

STEFÁNSSON, Tryggvi. **A UAV mechanism for autonomous landingand transportation of cargo**. [S.l.: s.n.], 2014.

SUGAHARA, Yusuke et al. Design of a battery-powered multi-purpose bipedal locomotor with parallel mechanism. In: IEEE. IEEE/RSJ International Conference on Intelligent Robots and Systems. [S.l.: s.n.], 2002. P. 2658–2663.

SULLIVAN, Richard M; WILLIAMS, Paxton S; PROKHOROV, Danil V. **Systems for transporting, deploying, and docking unmanned aerial vehicles mountable on a ground vehicle**. [S.l.]: Google Patents, Feb. 2019. US Patent 10,207,820.

TISCHLER, C.R; SAMUEL, A.E; HUNT, K.H. Kinematic chains for robot hands—II. Kinematic constraints, classification, connectivity, and actuation. **Mechanism and Machine Theory**, Pergamon, v. 30, n. 8, p. 1217–1239, 1995. ISSN 0094-114X. DOI: 10.1016/0094-114X(95)00044-Y. Disponível em: https://www.sciencedirect.com/science/article/pii/0094114X9500044Y.

TSAI, Lung-Wen. **Mechanism design: enumeration of kinematic structures according to function**. [S.l.]: CRC press, 2000.

UNAL, R. et al. Prototype design and realization of an innovative energy efficient transfemoral prosthesis. In: 2010 3rd IEEE RAS EMBS International Conference on Biomedical Robotics and Biomechatronics. [S.l.: s.n.], 2010. P. 191–196. DOI: 10.1109/BIOROB.2010.5626778.

VAN OORT, Gijs et al. An energy efficient knee locking mechanism for a dynamically walking robot. In: IEEE. 2011 IEEE International Conference on Robotics and Automation. [S.l.: s.n.], 2011. P. 2003–2008.

VILLA, Daniel KD; BRANDAO, Alexandre S; SARCINELLI-FILHO, Mário. A survey on load transportation using multirotor UAVs. **Journal of Intelligent & Robotic Systems**, Springer, v. 98, n. 2, p. 267–296, 2020.

WEIHMANN, Lucas. **MODELAGEM E OTIMIZAÇÃO DE FORÇAS E TORQUES APLICADOS POR ROBÔS COM REDUNDÂNCIA CINEMÁTICA E DE ATUAÇÃO EM CONTATO COM O MEIO**. 2013. S. 1689–1699. PhD thesis. ISBN 9788578110796. DOI: 10.1017/CBO9781107415324.004. arXiv: arXiv:1011.1669v3.

YAN, Hong-Sen. **Creative design of mechanical devices**. [S.l.]: Springer Science & Business Media, 1998.

YANG, Y; LI, M; LI, KR. Comparison and analysis of main effect elements of machining distortion for aluminum alloy and titanium alloy aircraft monolithic component. **The International Journal of Advanced Manufacturing Technology**, Springer, v. 70, n. 9-12, p. 1803–1811, 2014.

YOO, Wonsang; YU, Eun; JUNG, Jaemin. Drone delivery: Factors affecting the public's attitude and intention to adopt. **Telematics and Informatics**, Elsevier, v. 35, n. 6, p. 1687–1700, 2018.

ZHOU, Hong. Dimensional synthesis of adjustable path generation linkages using the optimal slider adjustment. **Mechanism and Machine Theory**, Pergamon, v. 44, n. 10, p. 1866–1876, 2009. ISSN 0094114X. DOI: 10.1016/j.mechmachtheory.2009.03.010.

ZIPAY, John J; MODLIN, Clarence T; LARSEN, Curtis E. The ultimate factor of safety for aircraft and spacecraft-its history, applications and misconceptions. In: 57TH AIAA/ASCE/AHS/ASC Structures, Structural Dynamics, and Materials Conference. [S.l.: s.n.], 2016. P. 1715.

APPENDIX A – LANDING MOTION STATIC ANALYSIS MATRICES

$$
\boldsymbol{Q} = \begin{array}{c}
\begin{matrix} F_{xd} & F_{yd} & F_{xe} & F_{ye} & F_{xa} & T_a & F_{xb} & F_{yb} & T_b & F_{xc} & F_{yc} & F_{xf} & F_{yf} & F_{xg} & F_{yg} & T_g & W \end{matrix} \\
\begin{bmatrix}
1 & 1 & -1 & -1 & 1 & 1 & 0 & 0 & 0 & 0 & 0 & 0 & 0 & 0 & 0 & 0 & 1 \\
-1 & -1 & 0 & 0 & 0 & 0 & 1 & 1 & 1 & 0 & 0 & 0 & 0 & 0 & 0 & 0 & 0 \\
-1 & -1 & 0 & 0 & 0 & 0 & 0 & 0 & 0 & 1 & 1 & 0 & 0 & 0 & 0 & 0 & 0 \\
0 & 0 & -1 & -1 & 0 & 0 & 0 & 0 & 0 & 0 & 0 & 1 & 1 & 0 & 0 & 0 & 0 \\
0 & 0 & 1 & 1 & 0 & 0 & 0 & 0 & 0 & 0 & 0 & 0 & 0 & 1 & 1 & 1 & 0
\end{bmatrix}
\end{array}
\tag{71}
$$

$$
\boldsymbol{A_D} = \begin{array}{c}
\begin{matrix} \$_{F_{xd}} & \$_{F_{yd}} & \$_{F_{xe}} & \$_{F_{ye}} & \$_{F_{xa}} & \$_{T_a} & \$_{F_{xb}} & \$_{F_{yb}} & \$_{T_b} & \$_{F_{xc}} & \$_{F_{yc}} & \$_{F_{xf}} & \$_{F_{yf}} & \$_{F_{xg}} & \$_{F_{yg}} & \$_{T_g} & \$_{W} \end{matrix} \\
\begin{bmatrix}
-y_d & x_d & -y_e & x_e & -y_a & 1 & -y_b & x_b & 1 & -y_c & x_c & -y_f & x_f & -y_g & x_g & 1 & x_W \\
0 & 0 & 0 & 0 & 1 & 0 & 0 & 0 & 0 & 0 & 0 & 0 & 0 & 0 & 0 & 0 & 0 \\
0 & 0 & 0 & 0 & 0 & 0 & 0 & 0 & 0 & 0 & 0 & 0 & 0 & 0 & 0 & 0 & 1
\end{bmatrix}
\end{array}
\tag{72}
$$

$$
\boldsymbol{A_N} = \begin{array}{c}
\begin{matrix} \$_{F_{xd}} & \$_{F_{yd}} & \$_{F_{xe}} & \$_{F_{ye}} & \$_{F_{xa}} & \$_{T_a} & \$_{F_{xb}} & \$_{F_{yb}} & \$_{T_b} & \$_{F_{xc}} & \$_{F_{yc}} & \$_{F_{xf}} & \$_{F_{yf}} & \$_{F_{xg}} & \$_{F_{yg}} & \$_{T_g} & \$_W \end{matrix} \\
\left[\begin{matrix}
-y_d & x_d & y_e & -x_e & -y_a & 1 & 0 & 0 & 0 & 0 & 0 & 0 & 0 & 0 & 0 & 0 & x_W \\
1 & 0 & -1 & 0 & 1 & 0 & 0 & 0 & 0 & 0 & 0 & 0 & 0 & 0 & 0 & 0 & 0 \\
0 & 1 & 0 & -1 & 0 & 0 & 0 & 0 & 0 & 0 & 0 & 0 & 0 & 0 & 0 & 0 & 1 \\
y_d & -x_d & 0 & 0 & 0 & 0 & -y_b & x_b & 1 & 0 & 0 & 0 & 0 & 0 & 0 & 0 & 0 \\
-1 & 0 & 0 & 0 & 0 & 0 & 1 & 0 & 0 & 0 & 0 & 0 & 0 & 0 & 0 & 0 & 0 \\
0 & -1 & 0 & 0 & 0 & 0 & 0 & 1 & 0 & 0 & 0 & 0 & 0 & 0 & 0 & 0 & 0 \\
y_d & -x_d & 0 & 0 & 0 & 0 & 0 & 0 & 0 & -y_c & x_c & 0 & 0 & 0 & 0 & 0 & 0 \\
-1 & 0 & 0 & 0 & 0 & 0 & 0 & 0 & 0 & 1 & 0 & 0 & 0 & 0 & 0 & 0 & 0 \\
0 & -1 & 0 & 0 & 0 & 0 & 0 & 0 & 0 & 0 & 1 & 0 & 0 & 0 & 0 & 0 & 0 \\
0 & 0 & y_e & -x_e & 0 & 0 & 0 & 0 & 0 & 0 & 0 & -y_f & x_f & 0 & 0 & 0 & 0 \\
0 & 0 & -1 & 0 & 0 & 0 & 0 & 0 & 0 & 0 & 0 & 1 & 0 & 0 & 0 & 0 & 0 \\
0 & 0 & 0 & -1 & 0 & 0 & 0 & 0 & 0 & 0 & 0 & 0 & 1 & 0 & 0 & 0 & 0 \\
0 & 0 & -y_e & x_e & 0 & 0 & 0 & 0 & 0 & 0 & 0 & 0 & 0 & -y_g & x_g & 1 & 0 \\
0 & 0 & 1 & 0 & 0 & 0 & 0 & 0 & 0 & 0 & 0 & 0 & 0 & 1 & 0 & 0 & 0 \\
0 & 0 & 0 & 1 & 0 & 0 & 0 & 0 & 0 & 0 & 0 & 0 & 0 & 0 & 1 & 0 & 0
\end{matrix} \right]
\end{array}
\tag{73}
$$

APPENDIX B – AERIAL TRANSPORT STATIC ANALYSIS MATRICES

$$\boldsymbol{Q} = \begin{array}{c} \begin{matrix} \$_{F_{xd}} & \$_{F_{yd}} & \$_{F_{xe}} & \$_{F_{ye}} & \$_{F_{xa}} & \$_{T_a} & \$_{F_{xb}} & \$_{F_{yb}} & \$_{F_{xc}} & \$_{F_{yc}} & \$_{F_{xsol}} & \$_{F_{ysol}} & \$_{F_{EL}} \end{matrix} \\ \begin{bmatrix} 1 & 1 & -1 & -1 & 1 & 1 & 0 & 0 & 0 & 0 & 0 & 0 & 0 \\ -1 & -1 & 0 & 0 & 0 & 0 & 1 & 1 & 0 & 0 & 0 & 0 & 1 \\ -1 & -1 & 0 & 0 & 0 & 0 & 0 & 0 & 1 & 1 & 0 & 0 & 0 \\ 0 & 0 & 1 & 1 & 0 & 0 & 0 & 0 & 0 & 0 & 1 & 1 & 0 \end{bmatrix} \end{array} \tag{74}$$

$$\boldsymbol{A_D} = \begin{array}{c} \begin{matrix} \$_{F_{xd}} & \$_{F_{yd}} & \$_{F_{xe}} & \$_{F_{ye}} & \$_{F_{xa}} & \$_{T_a} & \$_{F_{xb}} & \$_{F_{yb}} & \$_{F_{xc}} & \$_{F_{yc}} & \$_{F_{xsol}} & \$_{F_{ysol}} & \$_{F_{EL}} \end{matrix} \\ \begin{bmatrix} -y_d & x_d & -y_e & x_e & -y_a & 1 & -y_b & x_b & -y_c & x_c & -y_{sol} & x_{sol} & x_W \\ 1 & 0 & 1 & 0 & 1 & 0 & 1 & 0 & 1 & 0 & 1 & 0 & 0 \\ 0 & 1 & 0 & 1 & 0 & 0 & 0 & 1 & 0 & 1 & 0 & 1 & 1 \end{bmatrix} \end{array} \tag{75}$$

$$\boldsymbol{A_N} = \begin{array}{c} \begin{matrix} \$_{F_{xd}} & \$_{F_{yd}} & \$_{F_{xe}} & \$_{F_{ye}} & \$_{F_{xa}} & \$_{T_a} & \$_{F_{xb}} & \$_{F_{yb}} & \$_{F_{xc}} & \$_{F_{yc}} & \$_{F_{xsol}} & \$_{F_{ysol}} & \$_{F_{EL}} \end{matrix} \\ \begin{bmatrix} -y_d & x_d & y_e & -x_e & -y_a & 1 & 0 & 0 & 0 & 0 & 0 & 0 & 0 \\ 1 & 0 & -1 & 0 & 1 & 0 & 0 & 0 & 0 & 0 & 0 & 0 & 0 \\ 0 & 1 & 0 & -1 & 0 & 0 & 0 & 0 & 0 & 0 & 0 & 0 & 0 \\ y_d & -x_d & 0 & 0 & 0 & 0 & -y_b & x_b & 0 & 0 & 0 & 0 & x_W \\ -1 & 0 & 0 & 0 & 0 & 0 & 1 & 0 & 0 & 0 & 0 & 0 & 0 \\ 0 & -1 & 0 & 0 & 0 & 0 & 0 & 1 & 0 & 0 & 0 & 0 & 1 \\ y_d & -x_d & 0 & 0 & 0 & 0 & 0 & 0 & -y_c & x_c & 0 & 0 & 0 \\ -1 & 0 & 0 & 0 & 0 & 0 & 0 & 0 & 1 & 0 & 0 & 0 & 0 \\ 0 & -1 & 0 & 0 & 0 & 0 & 0 & 0 & 0 & 1 & 0 & 0 & 0 \\ 0 & 0 & -y_e & x_e & 0 & 0 & 0 & 0 & 0 & 0 & -y_{sol} & x_{sol} & 0 \\ 0 & 0 & 1 & 0 & 0 & 0 & 0 & 0 & 0 & 0 & 1 & 0 & 0 \\ 0 & 0 & 0 & 1 & 0 & 0 & 0 & 0 & 0 & 0 & 0 & 1 & 0 \end{bmatrix} \end{array} \tag{76}$$

APPENDIX C – LANDING MOTION STATIC ANALYSIS WITH LINK'S WEIGHT MATRICES

$$
\boldsymbol{Q} = \begin{array}{c}
\begin{matrix} F_{xd} & F_{yd} & F_{xe} & F_{ye} & F_{xa} & T_a & F_{xb} & F_{yb} & T_b & F_{xc} & F_{yc} & F_{xf} & F_{yf} & F_{xg} & F_{yg} & T_g & W & W_2 & W_3 & W_4 & W_5 & W_6 \end{matrix} \\
\begin{bmatrix}
1 & 1 & -1 & -1 & 1 & 1 & 0 & 0 & 0 & 0 & 0 & 0 & 0 & 0 & 0 & 0 & -1 & 0 & 0 & -1 & 0 & 0 \\
-1 & -1 & 0 & 0 & 0 & 0 & 1 & 1 & 1 & 0 & 0 & 0 & 0 & 0 & 0 & 0 & 0 & -1 & -1 & 0 & 0 & 0 \\
-1 & -1 & 0 & 0 & 0 & 0 & 0 & 0 & 0 & 1 & 1 & 0 & 0 & 0 & 0 & 0 & 0 & 0 & -1 & 0 & 0 & 0 \\
0 & 0 & -1 & -1 & 0 & 0 & 0 & 0 & 0 & 0 & 0 & 1 & 1 & 0 & 0 & 0 & 0 & 0 & 0 & 0 & 1 & 0 \\
0 & 0 & 1 & 1 & 0 & 0 & 0 & 0 & 0 & 0 & 0 & 0 & 0 & 1 & 1 & 1 & 0 & 0 & 0 & 0 & -1 & -1
\end{bmatrix}
\end{array} \tag{77}
$$

$$
\boldsymbol{A_D} = \begin{array}{c}
\begin{matrix} \$_{F_{xd}} & \$_{F_{yd}} & \$_{F_{xe}} & \$_{F_{ye}} & \$_{F_{xa}} & \$_{T_a} & \$_{F_{xb}} & \$_{F_{yb}} & \$_{T_b} & \$_{F_{xc}} & \$_{F_{yc}} & \$_{F_{xf}} & \$_{F_{yf}} & \$_{F_{xg}} & \$_{F_{yg}} & \$_{T_g} & \$_{W} & \$_{W_2} & \$_{W_3} & \$_{W_4} & \$_{W_5} & \$_{W_6} \end{matrix} \\
\begin{bmatrix}
-yd & xd & -ye & xe & -ya & 1 & -yb & xb & 1 & -yc & xc & -yf & xf & -yg & xg & 1 & xW & xW2 & xW3 & xW4 & xW5 & xW6 \\
1 & 0 & 1 & 0 & 1 & 0 & 1 & 0 & 0 & 1 & 0 & 1 & 0 & 1 & 0 & 0 & 0 & 0 & 0 & 0 & 0 & 0 \\
0 & 1 & 0 & 1 & 0 & 0 & 0 & 1 & 0 & 0 & 1 & 0 & 1 & 0 & 1 & 0 & 1 & 1 & 1 & 1 & 1 & 1
\end{bmatrix}
\end{array} \tag{78}
$$

$$
\boldsymbol{A_N} = \begin{array}{c}
\begin{matrix} \$_{F_{xd}} & \$_{F_{yd}} & \$_{F_{xe}} & \$_{F_{ye}} & \$_{F_{xa}} & \$_{T_a} & \$_{F_{xb}} & \$_{F_{yb}} & \$_{T_b} & \$_{F_{xc}} & \$_{F_{yc}} & \$_{F_{xf}} & \$_{F_{yf}} & \$_{F_{xg}} & \$_{F_{yg}} & \$_{T_g} & \$_{W} & \$_{W_2} & \$_{W_3} & \$_{W_4} & \$_{W_5} & \$_{W_6} \end{matrix} \\
\begin{bmatrix}
-y_d & x_d & y_e & -x_e & -y_a & 1 & 0 & 0 & 0 & 0 & 0 & 0 & 0 & 0 & 0 & 0 & x_W & 0 & 0 & x_W4 & 0 & 0 \\
1 & 0 & -1 & 0 & 1 & 0 & 0 & 0 & 0 & 0 & 0 & 0 & 0 & 0 & 0 & 0 & 0 & 0 & 0 & 0 & 0 & 0 \\
0 & 1 & 0 & -1 & 0 & 0 & 0 & 0 & 0 & 0 & 0 & 0 & 0 & 0 & 0 & 0 & 1 & 0 & 0 & 1 & 0 & 0 \\
y_d & -x_d & 0 & 0 & 0 & 0 & -y_b & x_b & 1 & 0 & 0 & 0 & 0 & 0 & 0 & 0 & 0 & x_W2 & x_W3 & 0 & 0 & 0 \\
-1 & 0 & 0 & 0 & 0 & 0 & 1 & 0 & 0 & 0 & 0 & 0 & 0 & 0 & 0 & 0 & 0 & 0 & 0 & 0 & 0 & 0 \\
0 & -1 & 0 & 0 & 0 & 0 & 0 & 1 & 0 & 0 & 0 & 0 & 0 & 0 & 0 & 0 & 0 & 1 & 1 & 0 & 0 & 0 \\
y_d & -x_d & 0 & 0 & 0 & 0 & 0 & 0 & 0 & -y_c & x_c & 0 & 0 & 0 & 0 & 0 & 0 & 0 & x_W3 & 0 & 0 & 0 \\
-1 & 0 & 0 & 0 & 0 & 0 & 0 & 0 & 0 & 1 & 0 & 0 & 0 & 0 & 0 & 0 & 0 & 0 & 0 & 0 & 0 & 0 \\
0 & -1 & 0 & 0 & 0 & 0 & 0 & 0 & 0 & 0 & 1 & 0 & 0 & 0 & 0 & 0 & 0 & 0 & 1 & 0 & 0 & 0 \\
0 & 0 & y_e & -x_e & 0 & 0 & 0 & 0 & 0 & 0 & 0 & -y_f & x_f & 0 & 0 & 0 & 0 & 0 & 0 & 0 & -x_W5 & 0 \\
0 & 0 & -1 & 0 & 0 & 0 & 0 & 0 & 0 & 0 & 0 & 1 & 0 & 0 & 0 & 0 & 0 & 0 & 0 & 0 & 0 & 0 \\
0 & 0 & 0 & -1 & 0 & 0 & 0 & 0 & 0 & 0 & 0 & 0 & 1 & 0 & 0 & 0 & 0 & 0 & 0 & 0 & -1 & 0 \\
0 & 0 & -y_e & x_e & 0 & 0 & 0 & 0 & 0 & 0 & 0 & 0 & 0 & -y_g & x_g & 1 & 0 & 0 & 0 & 0 & x_W5 & x_W6 \\
0 & 0 & 1 & 0 & 0 & 0 & 0 & 0 & 0 & 0 & 0 & 0 & 0 & 1 & 0 & 0 & 0 & 0 & 0 & 0 & 0 & 0 \\
0 & 0 & 0 & 1 & 0 & 0 & 0 & 0 & 0 & 0 & 0 & 0 & 0 & 0 & 1 & 0 & 0 & 0 & 0 & 0 & 1 & 1
\end{bmatrix}
\end{array} \tag{79}
$$